

**HYDRODYNAMIC MODEL FOR INVESTIGATION OF GAS FLOWS  
THROUGH MICRO-GEOMETRIES AND NANOPORES**

A thesis written at and submitted to

**KETTERING UNIVERSITY**

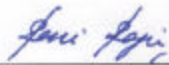
in partial fulfillment  
of the requirements for the  
degree of

**MASTER OF SCIENCE IN ENGINEERING  
MECHANICAL DESIGN MAJOR**

by

**RENI RAJU**

September 2003

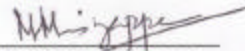


Author – Reni Raju

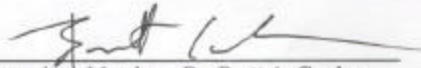


Faculty Advisor - Dr. Subrata Roy

Committee Member - Dr. Kingsley J. Berry



Committee Member - Dr. Meyya Meyyapan



Committee Member - Dr. Brett A. Cruden

## **DISCLAIMER**

This thesis is being submitted as partial and final fulfillment of the degree requirements of Kettering University needed to obtain a Master of Science in Mechanical Engineering Degree.

The conclusions and opinions expressed in this thesis are those of the writer and do not necessarily represent the position of Kettering University or any of its directors, officers, agents or employees with respect to the matters discussed.

## PREFACE

This thesis represents the capstone of my work in the Mechanical Engineering Department at Kettering University. I would like to express my sincere appreciation to Dr. Subrata Roy, who in the capacity of my faculty advisor introduced me to the subject. His technical guidance and moral support has made this thesis possible. I would like to acknowledge and extend my sincere gratitude to the my committee members, Dr. Meyya Meyyapan and Dr. Brett Cruden , Center of Nanotechnology, NASA Ames for their valuable time and guidance, without whom the completion of this thesis would not have been possible. I would like to acknowledge my thesis committee member Dr. K. Joel Berry, Head – Mechanical Engineering Department, Kettering University for his genuine help and concern during the period of thesis writing.

I would like to thank my colleagues at the Computational Plasma Dynamic Laboratory (CPDL) at Kettering University Dr. Birendra Pandey, Paresh Patel and Sagar Kapadia for their consistent support and assistance during the past two years. Finally I would like to acknowledge the faculty, staff and students of Kettering University who have knowingly or unknowingly helped me towards the successful completion of this thesis.

## TABLE OF CONTENTS

DISCLAIMER.....	ii
PREFACE.....	iii
LIST OF ILLUSTRATIONS.....	vi
I. INTRODUCTION .....	1
Overview of Flow through Microchannels .....	8
Diffusion in Nanotubes / Nanopores .....	10
II. HYDRODYNAMIC MODEL - ALGORITHM, METHODOLOGY AND IMPLEMENTATION.....	15
Governing Equations .....	15
Fluid-Wall Interactions .....	16
First order slip/jump boundary .....	16
Alternative slip boundary conditions .....	19
Finite Element Algorithm .....	20
Galerkin weak statement .....	21
Finite element basis function.....	22
III. MODELING OF SUBSONIC GAS FLOW THROUGH MICROCHANNELS .....	30
Model Geometry.....	30
Boundary Conditions .....	32
Results and Discussion.....	33
Case I .....	33
Case II.....	40
Case III.....	45
IV. MODELING OF SUPERSONIC GAS FLOW THROUGH MICROCHANNEL.....	49
Model Geometry.....	49
Boundary Conditions .....	51
Results and Discussion.....	52

V.	MODELING OF SUBSONIC GAS FLOW THROUGH A MICROCOLUMN .....	66
	Model Description .....	66
	Boundary Conditions .....	68
	Results and Discussion.....	68
VI.	MODELING OF GAS FLOW THROUGH NANOPORE AND NANOTUBULE .....	75
	Nanopore.....	76
	Anodisc membrane .....	76
	Carbon nanotubule .....	78
	Boundary Conditions .....	79
	Results and Discussion.....	80
	Anodisc membrane .....	80
	Carbon nanotubule .....	83
VII.	CONCLUSIONS AND RECOMMENDATIONS .....	88
	Recommendations for Future Work .....	90
	REFERENCES .....	91
	APPENDICES .....	100
	APPENDIX A: NOMENCLATURE .....	101
	APPENDIX B: JACOBIAN MATRIX (ACTUAL FORM).....	104
	APPENDIX C: JACOBIAN MATRIX (USED IN ALGORITHM).....	106

## LIST OF ILLUSTRATIONS

<u>Figures</u>	<u>Page</u>
1. Length scales for the smaller scale systems .....	3
2. Flow regimes based on Knudsen number .....	5
3. Quadrilateral element $\Omega_{el}$ in (a) global reference frame and (b) local reference frame for bilinear basis. ....	24
4. Full biquadratic quadrilateral element $\Omega_{el}$ in (a) global reference frame and (b) local reference frame. ....	25
5. A typical 9-noded quadrilateral element utilized.....	27
6. Schematics for microchannel analysis of Poiseuille flow inside a microchannel .....	32
7. Comparison of the normalized centerline pressure distribution for slip and no-slip finite element results for <i>Case I</i> .....	34
8. Comparison of the centerline $u$ -velocity distribution for slip and no-slip finite element results for <i>Case I</i> .....	35
9. Comparison of the normalized centerline pressure distribution for slip results with experimental data of Pong <i>et al.</i> ....	36
10. Comparison of the normalized centerline pressure distribution for slip results with numerical data of Chen <i>et al.</i> ....	36
11. Comparison of the centerline $u$ -velocity distribution for slip results with numerical data of Chen <i>et al.</i> ....	37
12. Comparison of the $u$ -velocity distribution for slip results with numerical data of Chen <i>et al.</i> for $P_{in}/P_{out} = 2.70$ .....	38
13. Two-dimensional contour plots for the streaming velocity inside the microchannel of slip and no-slip solutions for (a) $P_{in}/P_{out} = 1.34$ , and (b) $P_{in}/P_{out} = 2.70$ .....	39

14. Mass flow rate comparison of the slip and no-slip solution with the corresponding numerical result of Chen <i>et al.</i> .....	40
15. Comparison of the normalized centerline pressure distribution for slip and no-slip results with the experimental data of Shih <i>et al.</i> .....	41
16. Comparison of the centerline $u$ -velocity distribution for slip and no-slip solutions for <i>Case II</i> .....	42
17. Comparison of the $u$ -velocity for slip and no-slip condition in the $y$ -direction at three different sections along the length of the microchannel for $P_{in}/P_{out}=2.29$ .....	43
18. Comparison of the $v$ -velocity for slip and no-slip condition in the $y$ -direction at three different sections along the length of the microchannel for $P_{in}/P_{out}=2.29$ .....	44
19. Mass flow rate (kg/s) obtained by slip and no-slip conditions as compared to the slip and no-slip mass flow rate with the experimental data Shih <i>et al.</i> .....	44
20. Comparison of the normalized centerline numerical slip and no-slip pressure distribution for <i>Case III</i> .....	46
21. Comparison of the centerline slip and no-slip streamwise velocity solutions for <i>Case III</i> .....	46
22. Comparison of the $u$ - velocity for slip and no-slip condition in the $y$ -direction at three different sections along the length of the microchannel for $P_{in}/P_{out}=2.70$ .....	47
23. Comparison of mass flow rate (kg/s) obtained by slip and no-slip conditions to the experimental data of Arkilic <i>et al.</i> and the numerical slip and no-slip mass flow rates from Chen <i>et al.</i> .....	48
24. Schematic of microchannel geometry for supersonic gas flows .....	51
25. Mach number contours for (a) $Kn=0.062$ and (b) $Kn = 0.14$ .....	53
26. Pressure contours in Pa for (a) $Kn=0.062$ and (b) $Kn = 0.14$ .....	54
27. Density contours in $kg/m^3$ for (a) $Kn=0.062$ and (b) $Kn = 0.14$ .....	55
28. Temperature contours for (a) $Kn=0.062$ and (b) $Kn = 0.14$ .....	56
29. Comparison of, (a) centerline and (b) near wall, Mach number distribution of both N-S solutions with available DSMC results for $Kn =0.14$ .....	57
30. Mach number distribution of $Kn =0.062$ case, (a) at the centerline and (b) near the wall .....	58

31. Comparison of centerline distribution of temperature compared with the available DSMC results for (a) $Kn = 0.062$ and (b) $Kn = 0.14$ .....	59
32. Comparison of near wall distribution of temperature compared with the available DSMC results for (a) $Kn = 0.062$ and (b) $Kn = 0.14$ .....	60
33. Centerline pressure distribution of N-S solutions for (a) $Kn = 0.062$ and (b) $Kn = 0.14$ in comparison with DSMC results.....	61
34. Near wall pressure distribution of N-S solutions for (a) $Kn = 0.062$ and (b) $Kn = 0.14$ in comparison with DSMC results.....	62
35. Comparison for various cross sections in the $y$ -direction for $Kn = 0.062$ and $Kn = 0.14$ along the streamwise direction for Mach number. ....	64
36. Comparison for various cross sections in the $y$ -direction for $Kn = 0.062$ and $Kn = 0.14$ along the streamwise direction for temperature.....	65
37. Geometry schematic of microcolumn used for flow analysis .....	67
38. Downstream velocity vectors in the micro-column for $P_{in}/P_{out}=2.70$ . The peak $v$ -velocities are shown at the centerline distance of $1200 \mu m$ from the inlet .....	69
39. Pressure distribution comparison of slip and no-slip boundary condition along the centerline of the micro-column with $90^\circ$ bends .....	70
40. Pressure distribution comparison of slip flow results for the micro-column with $90^\circ$ bend and a straight microchannel along the centerline.....	71
41. $u$ - velocity distribution comparison of slip and no-slip boundary condition along the centerline of the micro-column with $90^\circ$ bends .....	72
42. $v$ - velocity distribution comparison of slip and no-slip boundary condition along the centerline of the micro-column with $90^\circ$ bends .....	73
43. Numerical comparison of mass flow rate for five pressure ratios with slip and no-slip wall conditions for the micro-column with $90^\circ$ bends.....	74
44. SEM image of Anodisc membrane of $200 \text{ nm}$ pores.....	78
45. (a) Density profile at the centerline, (b) velocity profile at the centerline, and (c) Argon molar flux along the centerline for $DP = 600 \text{ torr}$ .....	82
46. Solution validation of numerical results with experimental data for Argon .....	83



47. Flux versus pressure drop for Anodisc membranes processed with CVD at temperatures of 700° C compared to numerical results for $s_v = 1.0$ .....	84
48. Flux versus pressure drop for Anodisc membranes processed with CVD at temperatures of 750° C compared to numerical results for $s_v = 1.0$ .....	84
49. Argon massflux versus pressure drop for Anodisc membranes processed with CVD at 800° C compared to numerical results for different values of TMAC values. ....	85
50. Nitrogen massflux versus pressure drop for Anodisc membranes processed with CVD of 800° C compared to numerical results for $s_v = 0.52$ .....	86
51. Oxygen massflux versus pressure drop for Anodisc membranes processed with CVD at 800° C compared to numerical results for $s_v = 0.52$ .....	86
52. Normalized mass flow rate $\dot{m}/P_i^2 - P_o^2$ for experimental Argon data at 800 °C plotted as a function of the inverse mean pressure $1/\bar{P}$ .....	87

**Tables**

**Page**

1. Microchannel Dimensions and Properties of Fluid for Subsonic Gas Flows .....	31
2. Model Dimensions and Flow Parameters for Supersonic Gas Flows.....	50
3. Model Dimensions and Gas Properties for Flow through a Microcolumn.....	67
4. Nanopore Dimensions and Fluid Properties .....	77
5. Nanotubule Dimensions and Fluid Properties .....	79
6. Calculated and Measured Diffusivities of Anodisc Membrane ( $\times 10^{-5} \text{ m}^2/\text{s}$ ) .....	81

## I. INTRODUCTION

Feynman's famous lecture "There's plenty of room at the bottom" in 1959 [1], on the concept of small-scale devices has inspired the revolution of small systems, specifically micro/nanoelectromechanical systems (MEMS/NEMS). These are integrated micro/nano systems which combine mechanical and electrical components using the micromachining/nano-fabrication technology. In the past two decades advancement in silicon micromachining, bulk micromachining and other micromachining techniques have lead to a rapid development of the MEMS field particularly for silicon based microelectronics. The microfabrication technology enables fabrication of large arrays of small devices, which individually perform simple tasks but in combination can accomplish complicated functions. To date the primary applications of these devices are in the areas of biology, space, automobile and other microelectronics areas. The notable forms of these are,

- Sensors: electrostatic, piezoelectric, drive and signal electronics
- Actuators: mechanical, electrostatic, thermal, piezoelectric, electrostrictive, fluidic, pneumatic.
- Systems: pressure sensors, accelerometer, gyroscopes, optical devices, rf-devices, microfluidic, bio-medical devices, power-generation.

These developments in turn have paved the way to even smaller scale nanotechnology in which a combination of various fields like molecular biology, particle physics, space propulsion and microelectronics merge. Merriam-Webster dictionary offers the definition of nanotechnology as the art of manipulating on an atomic or molecular scale especially to build microscopic devices [2]. This interdisciplinary field offers the opportunity to build completely optimal systems at the molecular level, which utilize the smallest amount of matter and energy possible to perform a desired task. This remarkable utility of nanotechnology presents vast opportunities in every field for the future. Following are a few areas where nanotechnology has already found applications,

- Computer industry: logic circuits
- Plastics industry: nanoclays and composites, thermal insulation, fade proof materials
- Coating industry: nanocomposites/particles, high temperature stable, abrasion resistant materials
- Chemical industry: nanotubes, nanocatalysts, high thermal conducting materials, glass coating

In general MEMS devices are characterized as devices having a length scale less than  $10^{-1}$  m and greater than  $10^{-6}$  m. For length scales less than  $10^{-6}$  m these devices fall under the category of meso-scale and nano-scale systems. The nanoscale is of the order of  $10^{-9}$  m (1 nm) which is approximately 1/80,000 the diameter of a human hair. Figure 1 presents the categorization of these length scales in comparison with typical man made devices.

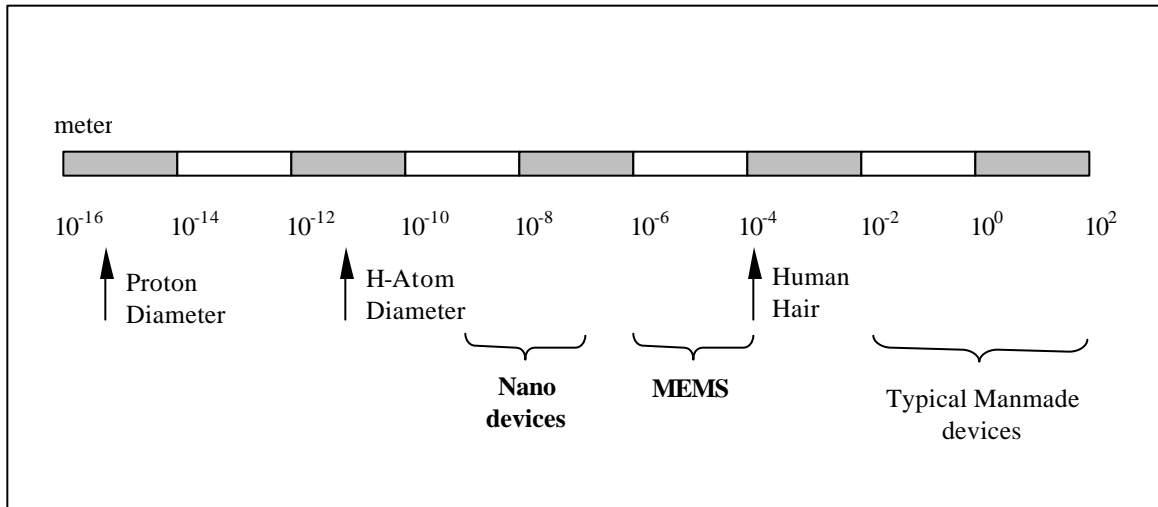


**Figure 1.** Length scales for the smaller scale systems. [3]

The focus of this study is to analyze gas flows through micro and nano-geometries. Recent advancements in manufacturing of micro-pumps, micro-valves, micro-turbines and micro-thrusters have invoked a strong fascination in microfluidics. In addition to gas flows electro-osmotic, electrophoresis and Brownian motion in liquid flows are also under investigation. Reduction in scale increases the complexity of these systems and it has been found the flow behavior fundamentally differs from that of macroscale systems. A strong understanding of the physical aspects and the laws governing these small systems has thus become essential. With the reduction in the length scale the fluid flow characteristics can be defined to be similar to rarefied for gases and granular for liquids. The walls “move” and several factors, some of which are neglected in larger systems, start playing dominant roles. These include wetting, adsorption, electrokinesis, rarefaction, compressibility, viscous heating, thermal creep [4], surface forces in liquids like van der Waals, electrostatic forces, steric forces [3,5] and gas-surface properties.

The fluid flow through micro devices are numerically modeled using either the continuum or the molecular approach [3, 6-8]. The continuum approach solves for macroscopic fluid properties as a function of the spatial coordinates and time and is used widely for various fluid flow applications. However as the length scale of a physical system decreases, the validity of the standard continuum approach with no-slip boundary conditions diminishes. Of critical importance is the Knudsen number (Kn) that determines the degree of rarefaction of gases encountered in such small flows. It is defined as

$$\text{Kn} = \frac{l}{\Lambda} \quad (1)$$

where the fluid mean free path  $l$  is described using the Chapman-Enskog result as  $l = 16m/5r\sqrt{2pRT}$  and  $\Lambda$  is the macroscopic length scale of the physical system which can be the scale of a gradient of a macroscopic quantity, e.g.  $\Lambda = r/\partial r/\partial x$ . As Kn increases, the rarefaction effects become more pronounced and eventually the continuum assumption breaks down. As  $\text{Kn} \rightarrow 0$ , the flow can be assumed sufficiently continuous while for  $\text{Kn} > 10$ , it becomes a free-molecule flow [9]. However, for  $10^{-3} < \text{Kn} < 10$  the flow is neither sufficiently continuum nor completely molecular, hence has been further divided into two subcategories; slip flow regime for  $10^{-3} < \text{Kn} < 10^{-1}$  and transition regime for  $10^{-1} < \text{Kn} < 10$ . Several models of streamwise velocity boundary condition are available for slip flow regime [4, 10-11]. However, in the transition region most reported literatures introduce molecular dynamics (MD) and other statistical methods [12-19]. Figure 2 describes different flow regimes based on the Knudsen number and the traditional methodology applied for modeling these flows presently.

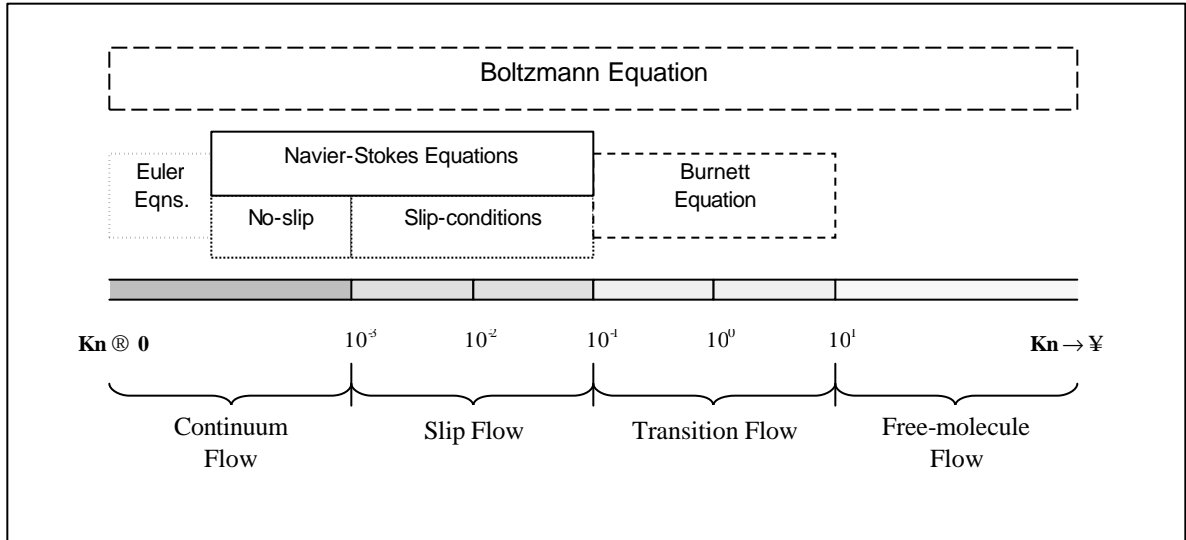


Figure 2. Flow regimes based on Knudsen number.

The molecular approach [12-14] analyzes the fluid as an aggregate of discrete particles instead of averaging the bulk properties. This model can be either deterministic [15-16] or statistical, [7, 17-19] giving the position, inertia and state of all the individual molecules at all times. The molecular approach considers individual particle dynamics based on a Boltzmann distribution at the temperature of interest and is particularly suitable for capturing small-scale interactions in free molecule flows ( $Kn > 10$ ). The interaction between two particles is given by the two-body potential energy and transient evolution of particle positions are determined by numerically integrating Newton's equations of motion. The choice of potential for particular fluid and solid combinations is, however, *ad hoc*. From the documented contributions in the literature, it is evident that, despite the theoretical appropriateness of Molecular dynamics (MD) models for the purpose of capturing the small-scale interactions, it is unrealistic to simulate a reasonably practical microflow problem using present day supercomputers. Most MD calculations

are restricted to femtosecond time steps limiting the results to short time scale (picoseconds to nanoseconds) phenomena [15-16]. Gad-el-hak [3] cites an example of 1 second real-time simulation for complex molecular interaction using MD that estimates thousands of years of CPU time requirement.

For dilute gases, molecular dynamics becomes highly inefficient while micro flow analysis using probabilistic models like direct simulation Monte Carlo (DSMC) provides accurate solution as the time step diminishes and the number of particles in the cell approaches a high number. However, the error in DSMC is inversely proportional to the square root of the number of simulated molecules [4] and thus decreasing the number of particles in the computational cell drastically increases the solution error [20]. The cell size should be one-third of the local mean-free-path; otherwise it leads to error in calculation of the dynamic viscosity coefficients [4]. Both molecular dynamics and DSMC have very slow convergence rates compared to continuum models. Also, due to the time splitting of the molecular motion and collisions, the maximum allowable DSMC time step needs to be smaller than the collisional time scale. For a practical problem involving a large matrix of candidate particles, these numerical restrictions translate to prohibitively expensive computational resources, severely limiting the application of DSMC to small-scale problems. Oh *et al.* [21] have also explained the difficulty of using DSMC at near atmospheric conditions. DSMC requires computational time to be less than the mean collision time which is of the order of  $10^{-10}$  seconds for this condition. Hence for low speed flows to reach a steady-state solution a minimum of  $10^8$  time steps maybe needed. Also for geometries with high aspect ratio of about 2500, which is

generally the case encountered for microchannels, a minimum of 500,000 cells would be required for computation [21].

As a viable remedy, several recent publications [22-24] have applied the Burnett equations [24] for rarified gas flows. These continuum equation solutions are reasonably fast compared to the molecular approach. However, accurate application of the Burnett equations becomes complicated as Knudsen number increases beyond the slip flow regime and the solution becomes unstable due to small wavelength disturbances. Since Burnett equations violate the entropy condition of thermodynamics at high Kn, artificial regularization becomes necessary to stabilize the solution [26]. Recently Sokhan *et al.* [27] have presented hydrodynamic boundary conditions for nonequilibrium molecular dynamics (NEMD) solutions in a 7.1 nm carbon nanopore. For Poiseuille flow of simple uniform fluids the relaxation times in NEMD are of the order of several picoseconds and increases by several orders of magnitude in confined geometries. The results show that in order to capture important fluctuations in collective physical flow properties an integration time of the order of 100  $\mu$ s is essential while an equilibration time of the order of 1 nanosecond is required for their computational domain [27].

As a means of achieving numerically efficient small scale flow predictions with reasonable computational time a finite element discretized Galerkin weak statement (GWS) based phase space model for small flow applications is being developed at the *Computational Plasma Dynamics Laboratory (CPDL) at Kettering university*. This method has been implemented for gas flow simulations through several micro-geometries and nanopores [28-32]. Based on the value of the Knudsen number these flows lie in the slip and transition regimes i.e.  $10^{-3} < Kn < 10$ . The aim of this thesis is to describe the



current state of the hydrodynamic model and document several validation results for flow through microchannels, microcolumn and nanopores. The following sections of this chapter describe in brief history of experimental and numerical investigations carried for afore mentioned geometries.

### **Overview of Flow through Microchannels**

A basic geometry that has been helpful in understanding the flow at the micro level is a microchannel. Both gaseous and liquid flow through microchannels has captured the interest of experimentalists for the past two decades. Several experiments have been carried out in order to understand the flow physics in these small scale systems. These flows can either be pressure-driven (Poiseuille), shear-driven (Couette) or thermal creep (transpiration) flows. In one of the earliest experiments Wu & Little [33] have measured heat transfer in fine channels and found higher friction factors compared to the established correlations. Experimental investigations of friction characteristics of nitrogen in circular micro tubes ranging from 3-81  $\mu\text{m}$  were carried out by Choi *et al.* [34]. Pfahler *et al.* [34] have documented friction measurements pertaining to channels of both large and small cross-sections. Liu *et al.* [36-37] manufactured microsystems to measure pressure distribution along a microchannel, which was followed by studies on first and second-generation systems by Pong *et al.* [38]. Shih *et al.* [39-40] have extended the same to detailed measurements of both mass flow rate and pressure distribution. Harley *et al.* [41] have investigated compressible flow through microchannels for low Reynolds number. Arkilic *et al.* [42-43] have carried out experiments for measuring the mass flow rate through long microchannels for helium gas. The effects of varying tangential momentum accommodation coefficients for different gas flows have also been

presented for these microchannels [44, 45]. Heat transfer performance and cooling characteristics of sub-cooled liquid through 0.7mm deep microchannels have been measured by Peng *et al.* [46]. Mala *et al.* [47] investigated the effect of electric double layer in a flow between parallel plates while Adams *et al.* [48] have tried to enhance heat transfer of forced liquid convection using dissolved non-condensables.

Many researchers have performed analytical and numerical simulation to validate the continuum model for the experimental data as long as the flow is within the slip and slightly transitional regime. Harley *et al.* [41] has used a two-dimensional finite element technique for evaluating the compressible flow through plates without considering the slip flow effects. Chen *et al.* [49] have studied the experimental results of Pong *et al.* [38] and Arkilic *et al.* [37] using the finite difference method with first-order slip conditions. Arkilic *et al.* [42] have done a two-dimensional analysis using the Navier-Stokes equations with first order slip boundary conditions to study compressibility and rarefaction effects in long microchannels. Shih *et al.* [40] have also validated the slip model with their data analytically. Karniadakis & Beskok [4] have carried out both analytical and numerical study of flow in different micro-geometries using direct simulation Monte Carlo (DSMC) and spectral element methods. Recently Zohar *et al.* [50] have presented an analytical solution for calculating the flow field of steady isothermal gas flow in microchannel accounting for compressibility, slip, acceleration and non-parabolic velocity profile effects. Xue *et al.* [51] have also derived a new analytical solution of Navier-stokes equations in microchannel flows into the transition regime.

In addition to the continuum models several researchers have presented Burnett equation and DSMC approach for modeling microflows. Xue *et al.* [7, 52] have used both DSMC and Burnett equation methods to study Poiseuille and Couette flow in microchannels. Oh *et al.* [21] have simulated supersonic flow of Helium gas through short microchannels of varying dimensions. Similar studies for Nitrogen have been carried out by Liou *et al.* [53]. Agarwal *et al.* [24] have compared the results obtained by using Burnett's equation model for both subsonic and supersonic gas flows. Mavriplis *et al.* [54] have also applied the DSMC method for investigating both supersonic and subsonic flows through in microsystems, however, for different geometries. Recently, McNenly *et al.* [55] has studied the applicability of different slip models for varying Knudsen number in comparison with the DSMC results.

### **Diffusion in Nanotubes/Nanopores**

As mentioned earlier, nanotechnology is an emerging field where a lot of research is still under progress. A few of the issues that are currently under investigation include the importance of quantum effects (like quantum dots, tunneling and wave-particle interaction), electronic transport, optic effects, thermal effects and energy transport by phonons in nanostructured materials. The complication of nano-dynamics arises due to the fact that it contains too many atoms to be easily understood by straightforward application of quantum mechanics and yet nano systems are not so large as to be completely free from quantum effects. From the fluidics aspect, the behavior of fluids inside these systems is treated separately as compared to microscale systems. Since physically nanopores and nanotubes are treated as porous media the fluid behavior is considered on the basis of diffusion through a porous material. Diffusion characteristics

through these membranes become increasingly important in chemical processes like catalytic and separation processes. In general the diffusion mechanism through pores can be characterized as Knudsen diffusion, molecular diffusion, surface diffusion or hydrodynamic flow. *Knudsen diffusion* is the flow that occurs when the mean free path of the fluid is of the same order of magnitude as the pore size and diffusion is governed by the collisions of molecules with the wall. This is the case that is generally encountered in nanosystems where the diameter of the pore is usually a few times larger than the molecular diameter of the fluid. If  $d_{pore}$  is the diameter of the pore then Knudsen diffusion occurs when  $d_{pore}/\lambda < 0.2$ . *Molecular diffusion* occurs when the diffusion is governed predominantly by the intermolecular collisions, as is the case in large pores where the mean free path of the fluid is not significant. *Surface diffusion* occurs when the fluid is adsorbed onto the pore surfaces and diffusion occurs through the movement of these adsorbed molecules. *Hydrodynamic flow* (Poiseuille flow) is a bulk flow which occurs due a pressure gradient across the membrane. This flow is only important in large pores where viscous effects are predominant. Fundamentally however, the diffusion is of two types; *self-diffusion* describing the motion of the molecules in absence of a gradient or diffusion of a single tagged molecule through the fluid; and *transport diffusion*, the motion of the molecules due to an existing concentration gradient.

Although porous membranes were known for quite sometime, nanotubules were discovered only in the past one decade. They were originally discovered by Iijima [56] as microtubules of carbon with diameter of 4-30 nm and 1  $\mu\text{m}$  length known as multi-wall carbon nanotubes (MWNT). Single walled cylinders of graphite carbon with diameters of 0.4 –3 nm were later reported known as single-wall carbon nanotubes (SWNT) [57, 58].

Ever since experimental studies have also been carried out in order to understand the transport phenomena in other nanoporous solids like zeolites [59, 60].

The computational studies of diffusion mechanisms through nanotubes and nanopores have begun only recently. An attempt has been made in this section to highlight some of the work that has been carried out so far. Tuzun *et al.* [61] have performed molecular dynamics simulations of flow of Helium and Argon through carbon nanotubes in order to study the rigidity of the tube on the behavior of the fluid. Sholl and Fichthorn [62] have examined diffusion of different gases like Ne, Ar, Kr, Xe, CH<sub>4</sub>, CF<sub>4</sub>, CCl<sub>4</sub>, SF<sub>6</sub>, SnCl<sub>4</sub> and SnBr<sub>4</sub> through molecular sieves of AlPO<sub>4</sub>-5. Molecular simulations of transport phenomena of these species were carried out both as single adsorbed species and binary mixtures. Further work using molecular dynamics on molecular cluster diffusion and permeance in zeolite membranes have also been carried out [63, 64]. In addition Sarvanan and Auerbach [65] have studied the lattice model of self-diffusion of benzene in faujasite type zeolites, Na-X and Na-Y. The model was used to explore the loading, temperature and nearest neighbor coupling parameter dependence of benzene self-diffusion. Keffer [66] has carried out molecular dynamics simulations of CH<sub>4</sub> and C<sub>2</sub>H<sub>6</sub> in one-dimensional molecular sieve of AlPO<sub>4</sub>-5 to examine the temperature dependence of the diffusivities of components in a binary adsorbed mixture. Self-diffusion of methane, ethane and ethylene through SWNT of various diameters and helical structure at 300K has been studied by Mao and Sinnott [16]. They have also investigated diffusive flow of binary mixtures of methane/ethane, methane/*n*-butane, and methane/isobutane through SWNT's using molecular dynamics simulation [67]. MacElroy *et al.* [68] have applied equilibrium and non-equilibrium molecular dynamics

simulations to investigate self-diffusion in a dense fluid confined within a model crystalline nanopore. Brownian dynamics was used to study flow induced by wall effects and time dependent concentration of particles in an adsorbing nanopore by ten Bosch [69]. Steady state Poiseuille flow through carbon slit pores and carbon nanopores were investigated by Sokhan *et al.* [27, 70] using non-equilibrium molecular dynamics (NEMD) simulations. These studies show that the fluid flows are characterized by a large slip length even for strong wetting cases. Seo *et al.* [71] have applied a dynamic Monte Carlo (MC) simulation method to calculate transport diffusion of hydrogen and hydrocarbons in nanoporous carbon membranes with slit-like pores. Transport selectivity of CH<sub>4</sub> and CO<sub>2</sub> was investigated by Nicholson [72] through cylindrical carbon pores with structureless walls. Düren *et al.* [73] have computed transport diffusion coefficients for CH<sub>4</sub>/CF<sub>4</sub> mixtures in MWNT consisting of three concentric nanotubes with innermost tube diameter of 2.978 nm. Ackerman *et al.* [74] have presented the self-diffusivity and transport-diffusivity of Argon and Neon through different SWNT's over a range of pore loadings corresponding to bulk phase equilibrium pressures of 0 to 100 bar. Recently, Roy *et al.* [28] have compared the numerical results with analytical and experimental results for Knudsen diffusivity through an anodisc membrane with pores of 200 nm diameters and operating pressure of 0-1200 torr.

The thesis documents three cases for flow through micro-geometries and two for nanopores. Summary of the remaining thesis chapter is as follows;

- a) Chapter II describes in detail the governing equations, slip/jump boundary conditions and the development of the finite element algorithm.
- b) Modeling of subsonic, low Reynolds number gas flows through different microchannels using the hydrodynamic model have been presented in Chapter III.

- c) Chapter IV covers the modeling of two cases of supersonic gas flows through short microchannels.
- d) Chapter V presents the flow characteristics of Nitrogen through a serpentine channel with two 90° bends.
- e) In Chapter VI the diffusion through an anodisc membrane with pores of 200 nm diameter and determination of slip coefficients of nanotubules have been presented.
- f) Finally conclusions and recommendations for future work are given in Section VII.

## II. HYDRODYNAMIC MODEL -ALGORITHM, METHODOLOGY AND IMPLEMENTATION

Due to practical limitations of DSMC and MD simulations, a two-dimensional hydrodynamic model based on first order slip/jump boundary conditions has been developed as an alternative to simulate flow through micro/nano-geometries in the slip and transitional flow regimes. The algorithm uses finite element methodology. The following sections detail the governing equations, boundary conditions and the algorithm implementation procedure. Nomenclature for all the variables, functions and constants is given in Appendix A.

### Governing Equations

The two-dimensional, time-dependent, compressible Navier-Stokes (NS) equation system with constant viscosity is used to analyze the gas flow through microchannels.

Conservation of Mass:

$$\frac{\partial \mathbf{r}}{\partial t} + \frac{\partial \mathbf{r}u}{\partial x} + \frac{\partial \mathbf{r}v}{\partial y} = 0 \quad (2)$$

Conservation of x- Momentum:

$$\frac{\partial \mathbf{r}u}{\partial t} + u \frac{\partial \mathbf{r}u}{\partial x} + v \frac{\partial \mathbf{r}u}{\partial y} + \frac{\partial P}{\partial x} - \mathbf{m} \left( \frac{\partial^2 u}{\partial x^2} + \frac{\partial^2 u}{\partial y^2} + \frac{1}{3} \left( \frac{\partial^2 u}{\partial x^2} + \frac{\partial^2 v}{\partial x \partial y} \right) \right) = 0 \quad (3)$$

Conservation of y- Momentum:

$$\frac{\partial \mathbf{r}v}{\partial t} + u \frac{\partial \mathbf{r}v}{\partial x} + v \frac{\partial \mathbf{r}v}{\partial y} + \frac{\partial P}{\partial y} - \mathbf{m} \left( \frac{\partial^2 v}{\partial x^2} + \frac{\partial^2 v}{\partial y^2} + \frac{1}{3} \left( \frac{\partial^2 v}{\partial y^2} + \frac{\partial^2 u}{\partial x \partial y} \right) \right) = 0 \quad (4)$$



Conservation of Energy:

$$rC_p \frac{DT}{Dt} - \frac{DP}{Dt} - \frac{\partial}{\partial x} \left( \mathbf{k} \frac{\partial T}{\partial x} \right) - \frac{\partial}{\partial y} \left( \mathbf{k} \frac{\partial T}{\partial y} \right) - \mathbf{m} \left( 2 \left( \frac{\partial u}{\partial x} \right)^2 + 2 \left( \frac{\partial v}{\partial y} \right)^2 + \left( \frac{\partial v}{\partial x} + \frac{\partial u}{\partial y} \right)^2 - \frac{2}{3} \left( \frac{\partial u}{\partial x} + \frac{\partial v}{\partial y} \right)^2 \right) = 0 \quad (5)$$

For the momentum equations, (3) and (5), the second coefficient of viscosity,  $\mathbf{m}'$  is based on the Stoke's hypothesis,  $\mathbf{m}' = -\frac{2}{3} \mathbf{m}$ .

The ideal gas law is used as the equation of state for closure of the Navier-Stokes equation system,

$$P - rRT = 0 \quad (6)$$

Equations (2)-(6) solve for five state variables; the fluid velocity in  $x$ -direction ( $u$ ), fluid velocity in  $y$ -direction ( $v$ ), gas density ( $r$ ), gas temperature ( $T$ ) and gas pressure ( $P$ ).

## **Fluid-Wall Interactions**

### **First order slip/jump boundary**

For the fluid-surface interaction the “no-slip” wall condition in the usual continuum description is defined as having all components of the velocity vanish at the solid wall and fluid temperature equal to that of the wall for near wall conditions. This assumption is based on the notion that there are sufficiently high number of collisions of the fluid molecules with the wall to thermodynamic equilibrate the fluid with the wall and randomize molecular motion near the wall to give zero bulk velocity. However, as the macroscopic length scale becomes comparable to the fluid mean free path, this assumption fails. For  $\text{Kn} > 10^{-3}$ , the collisions are not sufficient enough to maintain thermodynamic equilibrium and in the region near the wall a sub-layer of one gas mean free path thickness (Knudsen layer) develops. It is found that for  $\text{Kn} \leq 0.1$ , the Knudsen layer is relatively thin and can be neglected by extrapolating the bulk gas flow towards

wall [4]. This is can be done by relating tangential slip velocity,  $\Delta u$  on the wall to the local strain rate expressed mathematically as,

$$\Delta u|_w = L_s \left. \frac{du}{dy} \right|_w \quad (7)$$

where  $L_s$  is the slip length and  $du/dy|_w$  is the strain rate computed at the wall.

Alternatively it can be said that the streaming velocity at the wall is comprised of the streaming velocity of incident particles and that of the scattered particles. The boundary condition in this case can be interpreted as the flux or Neumann condition from the macroscopic point of view. One may use a Taylor series expansion on mean free path (Knudsen number) to determine the wall streaming velocity as a function of normal derivatives. Maxwell [10] derived the first order slip relations for dilute, monatomic gases. The relation of slip velocity near the wall for an ideal gas was given as,

$$u_{gas} - u_{wall} = \mathbf{I} \left( \frac{\partial u}{\partial y} \right)_w \quad (8)$$

In order to accommodate both diffuse and specular reflections of the fluid molecules from the walls, the final form of the Maxwell's [10] first order slip condition was derived as,

$$u_{gas} - u_{wall} = \frac{2 - \mathbf{s}_v}{\mathbf{s}_v} \mathbf{I} \left( \frac{\partial u}{\partial y} \right)_w + \frac{3}{4} \frac{\mathbf{m}}{\mathbf{r}T_{gas}} \left( \frac{\partial T}{\partial x} \right)_w \quad (9)$$

The second term in the equation (9) is known as 'thermal creep', which generates slip velocity in the direction opposite to the increasing temperature, a principle which is used in the operation of a Knudsen pump [75].

Using the Chapman-Enskog result for the mean free path, the equation can be modified to the following form,

$$- \mathbf{m} \left( \frac{\partial u}{\partial y} \right)_w = \frac{5 \mathbf{r} \mathbf{s}_V \sqrt{2 \mathbf{p} R T}}{16 (2 - \mathbf{s}_V)} \left( u_{gas} - u_{wall} + \frac{3}{4} \frac{\mathbf{m}}{\mathbf{r} T_{gas}} \left( \frac{\partial T}{\partial x} \right)_w \right) \quad (10)$$

The corresponding temperature-jump relation was derived by von Smoluchowski [11] as,

$$T_{gas} - T_{wall} = \frac{2 - \mathbf{s}_T}{\mathbf{s}_T} \left[ \frac{2 \mathbf{g}}{\mathbf{g} + 1} \right] \frac{\mathbf{l}}{\text{Pr}} \left( \frac{\partial T}{\partial y} \right)_w \quad (11)$$

Equation (11) can also be modified to the following form based on the Chapman-Enskog result for mean free path,  $\lambda$ ,

$$- \mathbf{k} \left( \frac{\partial T}{\partial y} \right)_w = \frac{\mathbf{s}_T \sqrt{2 \mathbf{p} R T}}{2 - \mathbf{s}_T} \left[ \frac{\mathbf{g} + 1}{2 \mathbf{g}} \right] \frac{5 \mathbf{r} C_p}{16} (T_{gas} - T_{wall}) \quad (12)$$

The slip-wall conditions in the equations (9)-(12) use the tangential-momentum accommodation coefficient,  $\mathbf{s}_V (0 \leq \mathbf{s}_V \leq 1)$  and the thermal accommodation coefficient,  $\mathbf{s}_T (0 \leq \mathbf{s}_T \leq 1)$  at the walls. The gas molecules on the wall are sometimes reflected from the wall with the same angle as that of the incident molecule exerting no shear stress on the wall. This reflection is known as *specular* reflection. On the other hand if the channel surface is rough the incident molecules maybe reflected at random angles, causing a *diffuse* reflection. The accommodation coefficients indicate the fraction of the molecules reflected diffusively from the walls. The definitions of the accommodation coefficients are given as,

$$\mathbf{s}_V = \frac{\mathbf{t}_{ic} - \mathbf{t}_r}{\mathbf{t}_{ic} - \mathbf{t}_w} \quad (13)$$

$$\mathbf{s}_T = \frac{dE_{ic} - dE_r}{dE_{ic} - dE_w} \quad (14)$$

Here,  $\mathbf{t}$  indicates the tangential momentum of molecules while  $dE$  denotes the energy flux. Based on the definitions given above, for  $\mathbf{s}_v = 0$  the molecules reflect specularly indicating the reversal in their normal velocity due to normal momentum transfer to the wall. For  $\mathbf{s}_v = 1$ , the molecules reflect diffusively when reflected from the wall with zero tangential velocity. Similarly  $\mathbf{s}_T = 0$  indicates a perfect energy exchange between the wall and the fluid. The value of the coefficients  $\mathbf{s}_V$  and  $\mathbf{s}_T$  depends on the surface finish, the fluid, temperature, and local pressure. A range of values for the tangential accommodation coefficient (0.2-0.8) has been determined experimentally for different gases and surfaces [44-45, 76].

### **Alternative slip boundary conditions**

Several researchers state that the equations (9)-(12) are applicable as long as  $\text{Kn} < 0.1$ . For higher values of Knudsen number, it is difficult to obtain accurate solution with just the first order slip boundary conditions. Studies by Srekanth [77] and Piekos & Breuer [78] suggest Maxwell's first order boundary condition breaks down near  $\text{Kn} = 0.15$ . Karniadakis & Beskok [4] has proposed a higher order slip boundary condition, which is the second order expansion in  $\text{Kn}$ , for predicting flow accurately for higher Knudsen number. The higher order slip velocity has been given as [4],

$$u_{gas}^* - u_{wall}^* = \frac{2 - \mathbf{s}_V}{\mathbf{s}_V} \frac{\text{Kn}}{1 - b(\text{Kn})} \frac{\text{Kn}}{\text{Kn}} \left( \frac{\partial u^*}{\partial y^*} \right)_w \quad (15)$$

where  $b(\text{Kn})$  is an empirical parameter defined as the ratio of the vorticity flux to the wall vorticity,  $b = \frac{1}{2} \left( \frac{\partial \mathbf{w} / \partial n}{\mathbf{w}} \right)_w$ . It can be determined analytically or by curve fitting the solutions of the Navier-Stokes and DSMC numerical models for higher  $\text{Kn}$  ranges.

However, it has also been suggested that this higher order slip boundary conditions may actually deviate from the actual solution more than the first order Maxwell's wall-slip conditions for some cases [55]. McNenly *et al.* [55] have suggested an empirical slip model based on DSMC as,

$$u_{gas}^* - u_{wall}^* = \frac{2 - \mathbf{s}_V}{\mathbf{s}_V} (1.253) \text{Kn} \left( \frac{\partial u^*}{\partial y^*} \right)_w \quad (16)$$

The coefficient is based on the best fit of DSMC results for Knudsen number range of 0.01 to 0.1 for Poiseuille and Couette gas flows.

Recent studies [28-32, 79], however, show that the first boundary conditions can be utilized for wide range of Knudsen number ranging from slip to transition. Since there are no significant advantages for using any other slip model the first order conditions (i.e. equations (9)-(12)) are utilized in this thesis to benchmark the cases presented.

### **Finite Element Algorithm**

The finite element method has been used since the 1950's for analyzing structural systems. With the development of weighted-residual criteria it has also found significant applications in fluid mechanics and heat transfer applications [80, 81]. Presently, algorithms developed using finite element methods are extensively used in numerical simulation of heat transfer and fluid flow [82-85]. The numerical development for this thesis is based on an in-house finite element platform utilized for a range of applications including electric propulsion, design optimization and micro/nanoscale flow analysis[28-32,83-85].

The equation system (2)-(6) for the finite element formulation can be represented in a concise form as,

$$L(\mathbf{q}) = \frac{\partial \mathbf{q}}{\partial t} + \frac{\partial (\mathbf{f}_j - \mathbf{f}_j^v)}{\partial x_j} - s = 0, \quad 1 \leq j \leq 2 \quad (17a)$$

$$\mathbf{q} = \begin{pmatrix} \mathbf{r} \\ \mathbf{r}u_i \\ \mathbf{r}C_p T + P \\ 0 \end{pmatrix}, \mathbf{f}_j = \begin{pmatrix} \mathbf{r}u_j \\ u_j \mathbf{r}u_i + P\mathbf{d}_{ij} \\ u_j (\mathbf{r}C_p T + P) \\ 0 \end{pmatrix}, \mathbf{f}_j^v = \begin{pmatrix} 0 \\ \mathbf{t}'_{ij} \\ k \frac{\partial T}{\partial x_j} + \mathbf{t}'_{ij} u_i \\ 0 \end{pmatrix}, s = \begin{pmatrix} 0 \\ 0 \\ 0 \\ P - \mathbf{r}RT \end{pmatrix}, \quad 1 \leq i \leq 2 \quad (17b)$$

where  $\mathbf{q}$  is the state variable,  $\mathbf{f}$  is the kinetic flux vector,  $\mathbf{f}^v$  the dissipative flux vector and

$s$  is the source term; and  $\mathbf{t}'_{ij} = \mathbf{m} \left( \frac{\partial u_i}{\partial x_j} + \frac{\partial u_j}{\partial x_i} \right) + \mathbf{d}_{ij} \mathbf{I} \operatorname{div} \mathbf{V}$ .

### **Galerkin weak statement**

The fundamental principle underlying the finite element method is the construction of a solution approximation as a series of assumed (known) spatial function multiplied by a set of unknown expansion coefficients. This can be done using the Rayleigh-Ritz variational procedure or the Galerkin weak statement [86]. Any real world smooth problem can be approximated as a Taylor or power series of known functions  $x_j$ . Such an approximation for our problem statement, equation (17), can be written as,

$$L(q) = \sum a_i \mathbf{f}_i(x_j) \quad (18)$$

where  $a_i$  are unknown coefficients and  $\mathbf{f}_i(x_j)$  are known functions of  $x_j$ .

The Galerkin weak statement (GWS) approach requires that the measure of the approximation error should vanish in an overall integrated sense. This gives a mathematical expression for minimization of the weighted residual over the domain for equation (17a) (also known as the *weak statement*) as,

$$WS = \int_{\Omega} wL(q)d\Omega \equiv 0 \quad (19)$$

Here,  $\Omega$  defines the domain for the problem statement and  $w$  is the weight function set which is arbitrary at this point. For the Galerkin criterion, the weight (test) function is made identical to the corresponding trial function set  $f_i$  for the approximation of state variables. Equation (19) guarantees that the associated approximation error is a minimum since it is orthogonal to the trial function set  $f_i$ . Thus the weak statement formulation for equation (19) corresponds to the following form,

$$WS = \int_{\Omega} f_i L(q) d\Omega \equiv 0 \quad (20)$$

The term “weak statement” signifies that the differentiability requirement for the approximation is weakened by one order. For example, second order terms in the momentum and energy equations reduces to first order.

### **Finite element basis function**

The finite element basis is a set of polynomials generally distributed uniformly on every subdivision (*finite element*) of the solution domain,  $\Omega$  created by placing nodes for better resolution and hence constructing the domain discretization  $\Omega^h$  [86]. Discretization for the domain is a fundamental concept of finite element analysis since it simplifies the construction of a wide range of suitable trial functions,  $f_i$ . The set of functions associated with the trial function,  $f_i$ , that spans a single generic element  $\Omega_{el}$  are defined as the *finite element basis*. The finite element basis,  $N_k$  maybe Chebyshev, Lagrange or Hermite interpolation polynomials complete to degree  $k$  based on the problem statement (one, two or three- dimensional).

Since for this case the problem statement is two-dimensional, appropriate two-dimensional quadrilateral elements are used. The discrete approximation of the spatially discretised domain  $\Omega^h$  yields a union of elements  $\Omega_{el}$  as shown,

$$\Omega^h = \bigcup_{el} \Omega_{el} \quad (21)$$

Similarly the integrated variables can be represented as the union of spatially and temporally discretized elements,

$$q(t, x_j) \approx q^h(t, x_j) = \bigcup_{el} q_{el}(t, x_j) \quad (22a)$$

$$q_{el}(t, x_j) = N_k(x_j) \mathcal{Q}_{el}(t) \quad (22b)$$

The spatially discretized two-dimensional quadrilateral finite element basis definition yields,

$$\mathcal{Q}_{el}(x_j) = \{N_k(\mathbf{h}_j)\} \{\mathcal{Q}\}_{el} \quad (23)$$

where the intrinsic coordinates spanning the quadrilateral  $\Omega_{el}$  constitute the tensor product system  $\mathbf{h}$ . The bases can be either *bilinear* or *biquadratic* corresponding to  $k=1$  or 2.

### Bilinear basis

A straight-sided quadrilateral finite element can be completely defined by the coordinates of the four intersections of the boundary segment generators. Figure 3(a) shows the geometry of a generic straight-sided quadrilateral element  $\Omega_{el}$  on a global coordinate system. The vertices of the quadrilateral are given as  $(X_i, Y_i)_{el}$ ,  $1 \leq i \leq 4$ . The mapping of the global coordinate system to the local coordinate system is shown in Figure 3(b). The coordinates of these nodes in the local  $\mathbf{h}_i$  coordinate system are normalized to unity for the origin defined at the element centroid.



The finite element bilinear basis for this coordinate system can be written as,

$$\{N_i(\mathbf{h}_i)\} = \frac{1}{4} \begin{Bmatrix} (1-\mathbf{h}_1)(1-\mathbf{h}_2) \\ (1+\mathbf{h}_1)(1-\mathbf{h}_2) \\ (1+\mathbf{h}_1)(1+\mathbf{h}_2) \\ (1-\mathbf{h}_1)(1+\mathbf{h}_2) \end{Bmatrix} \quad (24)$$

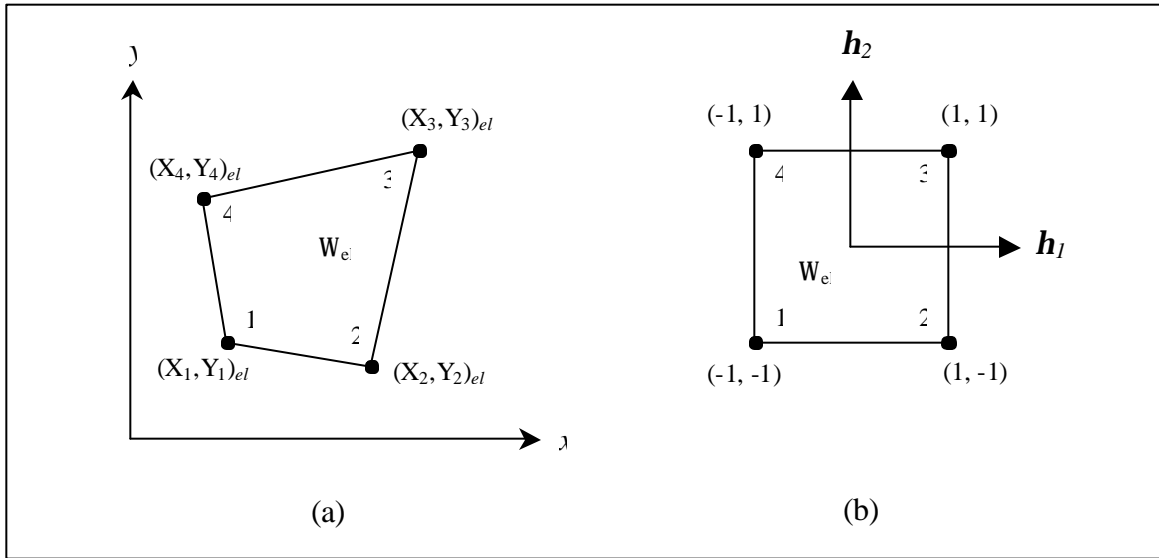
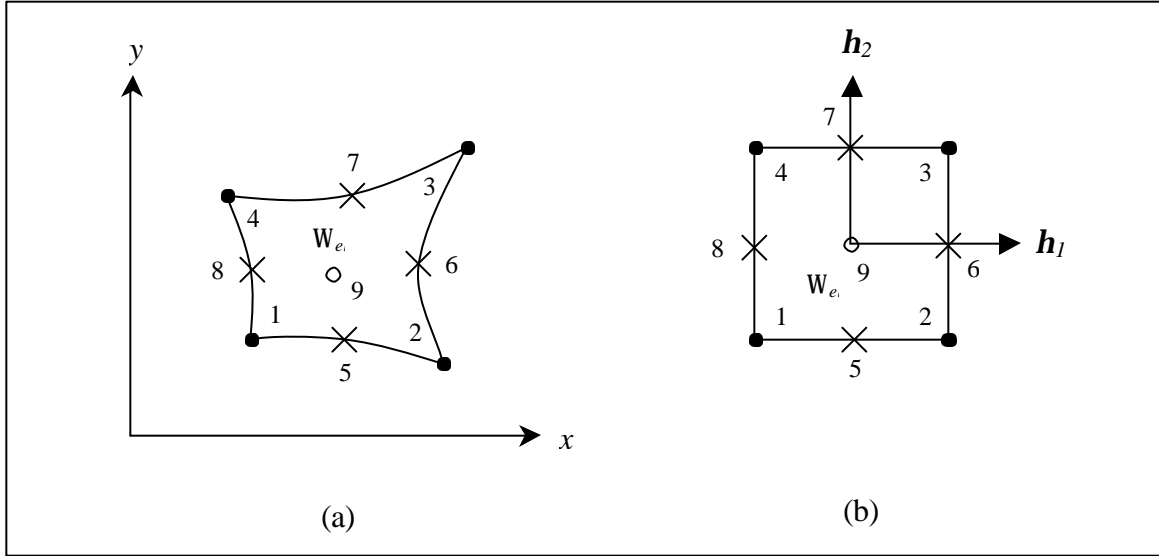


Figure 3. Quadrilateral element  $\Omega_{el}$  in (a) global reference frame and (b) local reference frame for bilinear basis. Note: From Finite Elements 1-2-3 (p. 209), Baker, A.J. and Pepper, D.W., McGraw Hill, Inc. (1991).

### Biquadratic bases

Biquadratic bases can either be complete biquadratic or *serendipity* bases, which utilizes only the element surface geometric nodes. Figure 4(a) shows the global reference frame of a quadrilateral element where the vertex nodes are numbered 1 to 4, while nodes 5 to 8 are sequentially located on the midside of four boundary segments of element  $\Omega_{el}$ . For full biquadratic elements only there is an additional node 9 at the centroid of the

element. The mapping of a biquadratic element in general coordinate system to the local coordinate system is shown in Figure 4(b).



**Figure 4.** Full biquadratic quadrilateral element  $\Omega_{el}$  in (a) global reference frame and (b) local reference frame. Note: From Finite Elements 1-2-3 (p. 213), Baker, A.J. and Pepper, D.W., McGraw Hill, Inc. (1991).

The finite element basis associated to this transformation is given by,

$$\{N_2(\mathbf{h}_i)\} = \frac{1}{4} \begin{Bmatrix} (1-h_1)(1-h_2)(h_1h_2) \\ (1+h_1)(1-h_2)(-h_1h_2) \\ (1+h_1)(1+h_2)(h_1h_2) \\ (1-h_1)(1-h_2)(-h_1h_2) \\ 2(1-h_1^2)(1-h_2)(-h_2) \\ 2(1-h_1)(1-h_2^2)(h_1) \\ 2(1-h_1^2)(1-h_2)(h_2) \\ 2(1-h_1)(1-h_2^2)(-h_2) \\ 4(1-h_1^2)(1-h_2^2) \end{Bmatrix} \quad (25)$$

For both the cases the bases provide the transformation given below,

$$\begin{aligned} x_{el} &= \{N_k(\mathbf{h}_j)\}\{X\}_{el} \\ y_{el} &= \{N_k(\mathbf{h}_j)\}\{Y\}_{el} \end{aligned} \quad (26)$$

Hence the semi-discrete finite element formulation for the problem statement (17) can be represented as,

$$\begin{aligned} WS^h &= S_{el} \left( \int_{\Omega_{el}} N_k L(Q_{el}) dt \right) \equiv 0 \\ WS^h &= S_{el} \left( \int_{\Omega_{el}} N_k \frac{dQ_{el}}{dt} dt + \int_{\Omega_{el}} N_k (-s) dt - \int_{\Omega_{el}} \frac{\partial N_k}{\partial x_j} (f_j - f_j^v) dt + \oint_{\partial\Omega_{el} \cap \partial\Omega^h} N_k (f_j - f_j^v) \hat{n}_j ds \right) \end{aligned} \quad (27)$$

Here  $S_{el}$  symbolizes the ‘‘assembly operator’’ carrying local (element  $el$ ) matrix coefficients into the global arrays and  $dt = dx dy$ . The differentiation of the basis function depends on both the global and local coordinates as shown below,

$$\nabla\{N_k\} = \mathbf{i} \frac{\partial\{N_k\}}{\partial x} + \mathbf{j} \frac{\partial\{N_k\}}{\partial y} = \frac{\partial\{N_k\}}{\partial \mathbf{h}_i} \left( \mathbf{i} \left( \frac{\partial \mathbf{h}_i}{\partial x} \right)_{el} + \mathbf{j} \left( \frac{\partial \mathbf{h}_i}{\partial y} \right)_{el} \right) \quad 1 \leq i \leq 2 \quad (28)$$

Hence inverse coordinate transformation (from  $\mathbf{h}_i$  to  $x_j$ ) is required to evaluate the formation of the assembly matrices containing the convection and diffusion information. The transformation jacobian matrix is the inverse of forward transformation i.e.

$$[J]_{el} = \begin{bmatrix} \frac{\partial \mathbf{h}_i}{\partial x_j} \end{bmatrix}_{el} = \begin{bmatrix} \frac{\partial x_j}{\partial \mathbf{h}_i} \end{bmatrix}_{el}^{-1}.$$

The weak statement naturally yields the surface integrals via application of the Green-Gauss theorem in equation (28), which contains the unknown boundary fluxes wherever Dirichlet (fixed) boundary conditions are enforced. The zero gradient boundary conditions are automatically enforced via removal of the surface integral. For the slip flow boundary, appropriate surface integrals are replaced by incorporating the equations (10) and (12) for the momentum and energy equations only.

For all the cases presented in the following chapters the computational channel geometry is discretized using two-dimensional non-overlapping 9-noded biquadratic finite elements. The continuity and equation of state are solved for density and pressure respectively using the four corner nodes of the element. For velocity and temperature calculations, all nine nodes of the biquadratic element are used as shown in Figure 5.

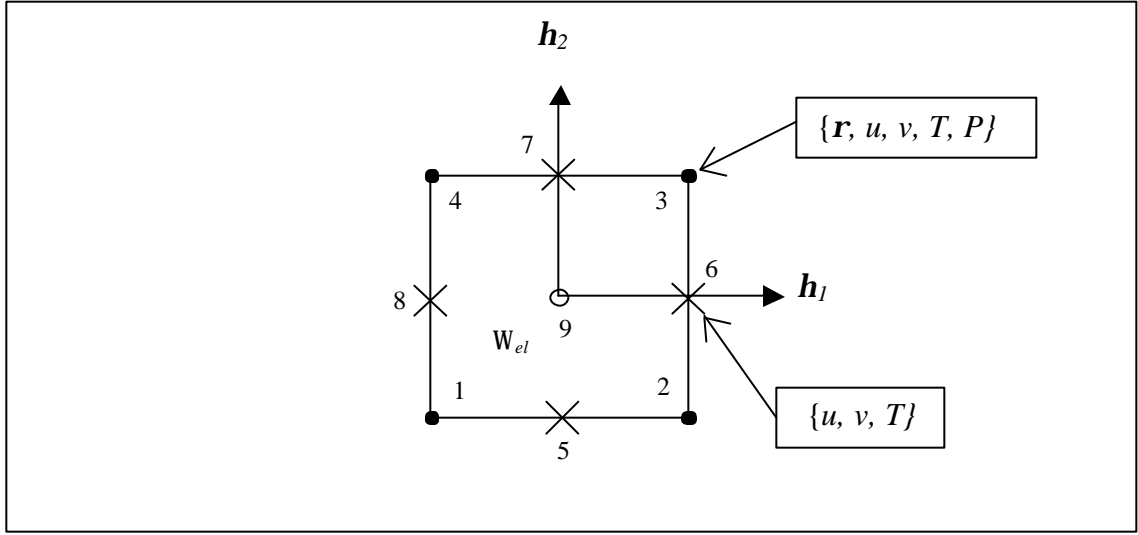


Figure 5. A typical 9-noded quadrilateral element utilized.

Independent of the physical dimension of  $\Omega$ , and for general forms of the flux vectors, the semi-discretized weak statement of equation (28) always yields an ordinary differential equation (ODE) system of the following form,

$$WS^h = S_{el} \left( M_{el} \frac{dU}{dt} + \mathfrak{R}_{el}(Q) \right) = M \frac{dU}{dt} + \mathfrak{R}(Q) = \{0\} \quad (29)$$

where  $Q$  is the time-dependent finite element nodal vector,  $M = S_{el}(M_{el})$  is the “mass” matrix associated with element level interpolation, while  $\hat{\mathbf{A}}$  carries the element convection information and the diffusion matrix resulting from genuine (non-Eulerian) or

numerical elemental viscosity effects, and all known data. The time derivative  $dU/dt$ , is generally replaced by using a  $q$ -implicit or  $t$ -step Range-Kutta time integration procedure and the terminal ODE is usually solved using the Newton-Raphson scheme,

$$\begin{aligned} Q_{t+1}^{i+1} &= Q_{t+1}^i + \Delta Q^i = Q_t + \sum_{p=0}^i Q^{p+1} \\ \Delta Q^i &= -[M + q\Delta t(\partial\mathfrak{R}/\partial Q)]^{-1}\mathfrak{R}(Q) \end{aligned} \quad (30)$$

The choice of time step is dictated by the Courant-Fredrich-Levy condition [87].

The code uses variable time steps until the transient features die down as the iteration converges to a steady state. The solution is declared convergent when the maximum residual for each of the state variables becomes smaller than a chosen convergence criterion of  $\epsilon = 10^{-4}$ . Here, the convergence of a solution vector  $U$  on node  $j$  is defined as the norm:

$$\frac{\|Q_j - Q_{j-1}\|}{\|Q_j\|} \leq \epsilon \quad (31)$$

Here, an implicit ( $q=1$ ) time stepping procedure is employed. The obvious numerical issues are associated with calculation of the “jacobian”,  $\partial\mathfrak{R}/\partial Q$  with sufficient accuracy. The “jacobian” associated with the problem statement has been represented in Appendix B and C.

The difficulty involved in achieving a steady state solution for equations (2)-(6) directly is due to the selection of initial conditions. The conventional method of achieving a steady state solution is to use the time term as a relaxation parameter in the equation system and run the problem until the transient features die down. In some of the cases, an artificial diffusion term has been utilized as an initial condition generator to obtain a final steady state solution instead using unsteady conditions.

Equation (17) can be modified in the following steady state form,

$$L(\mathbf{q}) = \frac{\partial(\mathbf{f}_j - \mathbf{f}_j^y)}{\partial x_j} - \mathbf{b} \frac{\partial^2 \tilde{\mathbf{q}}}{\partial x_j^2} - s = 0, \quad 1 \leq i, j \leq 2 \quad (32)$$

where,  $\tilde{\mathbf{q}}^T = (0, u_i, T, 0)$  and  $\mathbf{b}$  is a diffusion perturbation parameter that can be varied separately for each state variable. As  $\mathbf{b} \rightarrow 0$ , equation (32) reverts back to steady state form of equation (17). Initially  $\mathbf{b}$  is set to a sufficiently high value so as to generate a diffused but stable convergence to steady state solution. Progressive reduction of  $\mathbf{b}$  is carried out until the final steady state solution with  $\mathbf{b} \rightarrow 0$  is achieved. This procedure is analogous to using the transient relaxation.

### III. MODELING OF SUBSONIC GAS FLOW THROUGH MICROCHANNELS

This chapter focuses on establishing the finite element based hydrodynamic model for simulating subsonic gas flows through microchannels. Here a detailed comparison and benchmarking of the developed model is documented for several experimental [38, 40, 42] and numerical data [49] published in literature. The model assumes the gas flow through two parallel plates of length  $L$ , width  $W$  and separated by a distance  $H$ . Neglecting the end effects only the two-dimensional geometry stretching in the  $x$  and  $y$  directions is considered.

#### **Model Geometry**

The model dimensions and gas properties for three cases of microchannel flow simulation are listed in Table 1. The three cases (*I - III*) will validate the finite element based numerical results with the experimental data of Pong *et al.* [38], Shih *et al.* [40] and Arkilic *et al.* [42] respectively, for different pressure ratios. Pong *et al.* [38] have initially measured the pressure distribution along a long microchannel with an aspect ratio of 2500 using pressure sensors. Shih *et al.* [40] have extended the work of Pong *et al.* [38] by measuring both pressure distribution and mass flow rate for Helium for a different length of microchannel (4000  $\mu\text{m}$ ). Arkilic *et al.* [42] have carried out similar experiments by measuring the Helium gas mass flow rate in a channel with aspect ratio of 5639.

Table 1

Microchannel Dimensions and Properties of Fluid for Subsonic Gas Flows

<b>Parameters</b>	<b>Case I</b> (Pong <i>et al.</i> [38])	<b>Case II</b> (Shih <i>et al.</i> [40])	<b>Case III</b> (Arkilic <i>et al.</i> [42])
Working Fluid	Nitrogen	Helium	Helium
$L$ (mm)	3000.0	4000.0	7500.0
$W$ (mm)	40.0	40.0	52.25
$H$ (mm)	1.2	1.2	1.33
$P_{in}/P_{out}$	1.34, 1.68, 2.02, 2.36, 2.70	1.59,1.87,1.92, 2.29	1.34, 1.68, 2.02, 2.36, 2.70
$P_{out}$ (kPa)	100.8	100.8	100.8
$T_{in}$ (K)	314.0	300.0	314.0
$T_w$ (K)	314.0	300.0	314.0
<b>Kn</b>	0.0585	0.17	0.155
$\mu$ (Ns/m <sup>2</sup> )	$1.85 \times 10^{-5}$	$2.066 \times 10^{-5}$	$2.066 \times 10^{-5}$
?	1.4	1.667	1.667
$R$ (J/kg K)	296.7	2076.9	2076.9

The exit Kn for these three cases are 0.0585, 0.17 and 0.155, respectively, ranging from slip to transitional regime. Chen *et al.* [49] has reported numerical results for *Case I* and massflow rate comparison for *Case III* using a fine grid finite difference formulation with Maxwell's first order slip boundary conditions. Figure 6 illustrates the schematics of the Poiseuille flow through the microchannel.



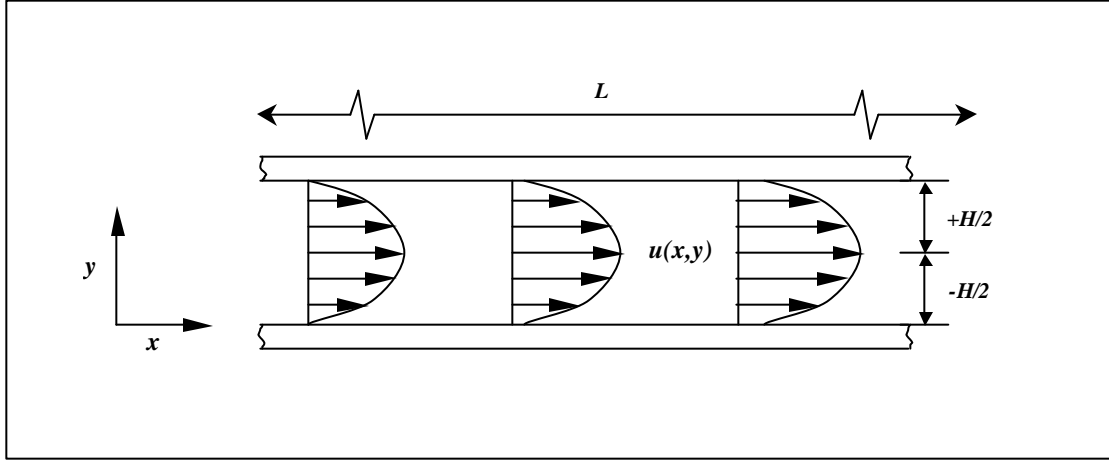


**Figure 6.** Schematics for microchannel analysis of Poiseuille flow inside a microchannel.

### **Boundary Conditions**

Table 1 includes the boundary conditions for all the three cases presented in this chapter. The gas temperature  $T_{in}$  is specified at the inlet and based on the assumption of isothermal wall the wall temperature  $T_w$  is specified. At the inlet the velocity flux is  $\partial u / \partial x = 0$  and the y-component of the velocity is  $v = 0$ . The pressure at the outlet,  $P_0$  is 100.8 kPa for all the three cases and the inlet pressure,  $P_{in}$ , is specified based on the corresponding pressure ratio. The flow through the microchannel is benchmarked using both no-slip and first order slip conditions. Shih *et al.* [40] have given the averaged effective tangential accommodation coefficient for *Case II* to be 1.162 indicating perhaps a non-physical quantity since by definition  $0 < \mathbf{s}_V < 1.0$ . For the remaining cases we assume  $\mathbf{s}_V = \mathbf{s}_T \approx 1.0$  consistent with the reported numerical result [49], since the roughness of the channel is not known. This is applicable to most of the engineering systems, implying that the all the molecules would encounter diffuse reflection.

## **Results and Discussion**

### **Case I**

The centerline pressure results for the finite element model slip-model have been validated with the experimental data of Pong *et al.* [38] for their first generation microchannel. The experimental data were based on four pressure sensors along the length of the channel. The maximum uncertainty for these experimental measurements was determined to be less than 1 psig (6.89 kPa) for most sensors. The maximum Knudsen number is found to be 0.0585 at the outlet. For this case, the computational geometry is discretized using 324 two-dimensional 9-noded non-overlapping bi-quadratic finite elements, giving a total of 1369 nodes. The solution for the dimensional equations (2)-(6) yields a non-linear distribution of pressure, density and velocity along the microchannel.

Flow resistance arising from wall frictional forces induces the pressure drop in the channel. As the temperature variation along the channel is negligible, the density becomes directly proportional to the pressure following the ideal gas law, and hence shows a corresponding drop along the channel. A corresponding increase in velocity preserves the continuity equation. The effect of slip and no-slip boundary conditions at the centerline of the channel is shown in Figure 7. An increase in shear stress with increasing velocity further reduces the pressure, giving a non-linear dependence of pressure on position. Clearly, increasing divergence is observed between the no-slip and slip wall pressure solutions as the pressure ratio increases. This effect is most noticeable for the highest considered pressure ratio of 2.70 where the maximum percentage difference in the pressure prediction between two solutions is  $\sim +4\%$ . However, near the

downstream region lower shear stresses are encountered by the flow causing a larger difference between the slip and no-slip solutions for the same pressure ratio.

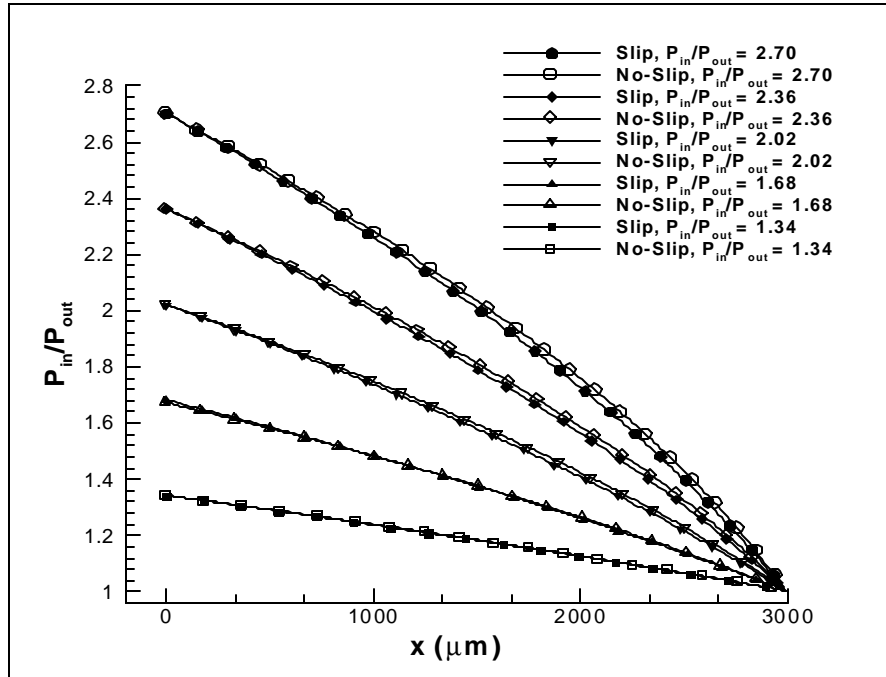


Figure 7. Comparison of the normalized centerline pressure distribution for slip and no-slip finite element results for *Case I*.

The corresponding  $u$ -velocity solutions at the channel centerline are plotted in Figure 8. The slip condition consistently predicts a higher magnitude of velocity than the no-slip condition due to lower shear stress. As the pressure ratio increases, the streaming velocity distribution becomes increasingly non-linear. The difference between the slip and no-slip velocity distribution shows a higher difference for the corresponding higher pressure ratio. The percentage difference between the slip and no-slip condition is  $\sim +8\%$ .

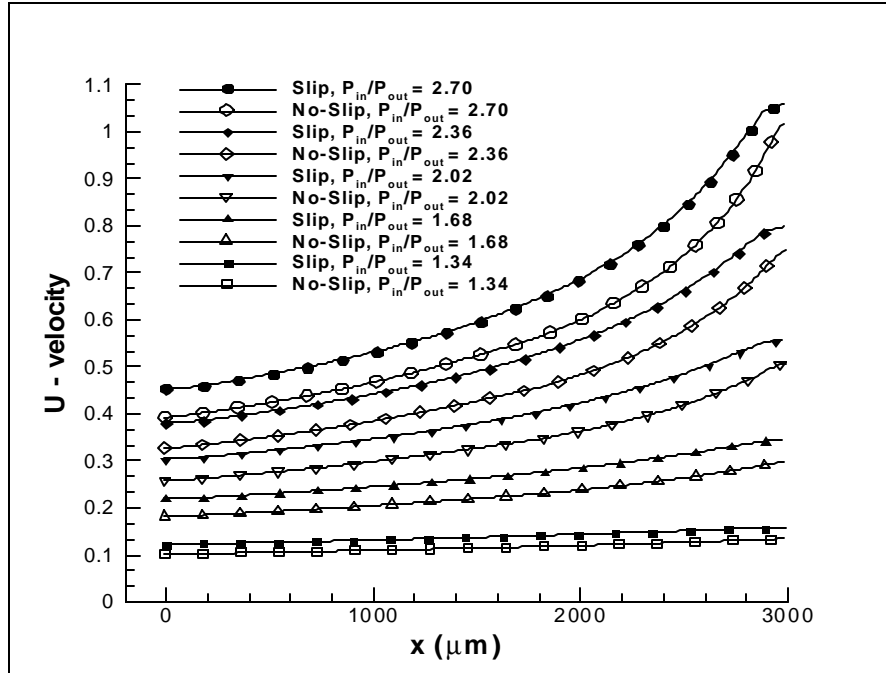


Figure 8. Comparison of the centerline  $u$ -velocity distribution for slip and no-slip finite element results for *Case I*.

For five selected pressure ratios, the computed finite element model solutions are found to be within approx. -2 % of the experimental data, Figure 9. Overall, presented simulation results under predicted the experimental data in the upstream section and matches well in the downstream. The computed solutions for the same five pressure ratios are further benchmarked with numerical results previously reported in the literature [49]. The numerical results as plotted against that of Chen *et al.* [49] generate a similar non-linear pressure distribution trend in Figure 10 and the centerline pressure distributions are found to be comparable within 3.5 % of the reported results. It is important to note that Chen *et al.* [49] has utilized explicit finite difference method on a  $6000 \times 23$  grid for this simulation, while an  $18 \times 18$  biquadratic finite element mesh has been used for this thesis.

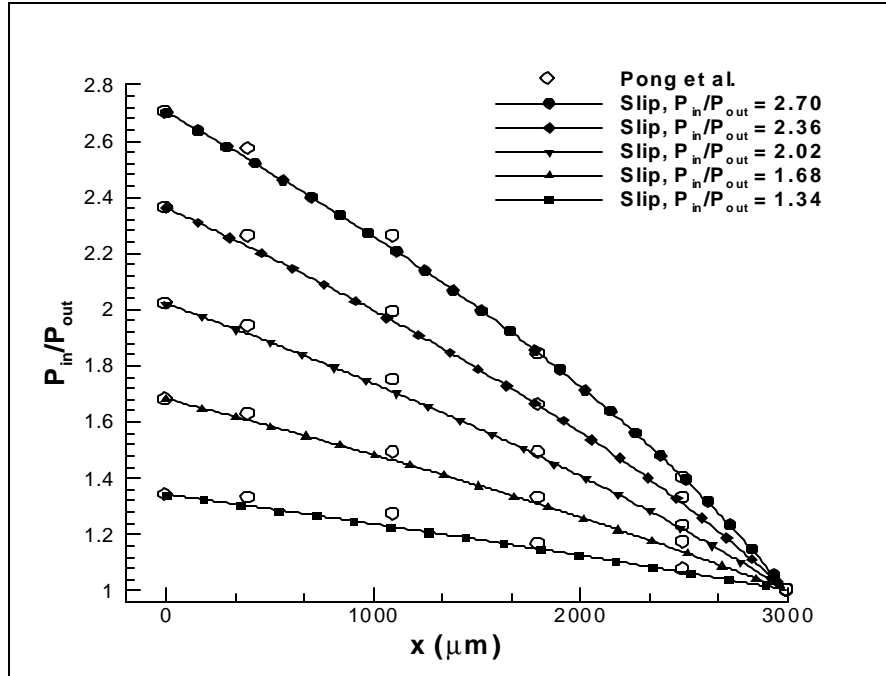


Figure 9. Comparison of the normalized centerline pressure distribution for slip results with experimental data of Pong *et al.* [38].

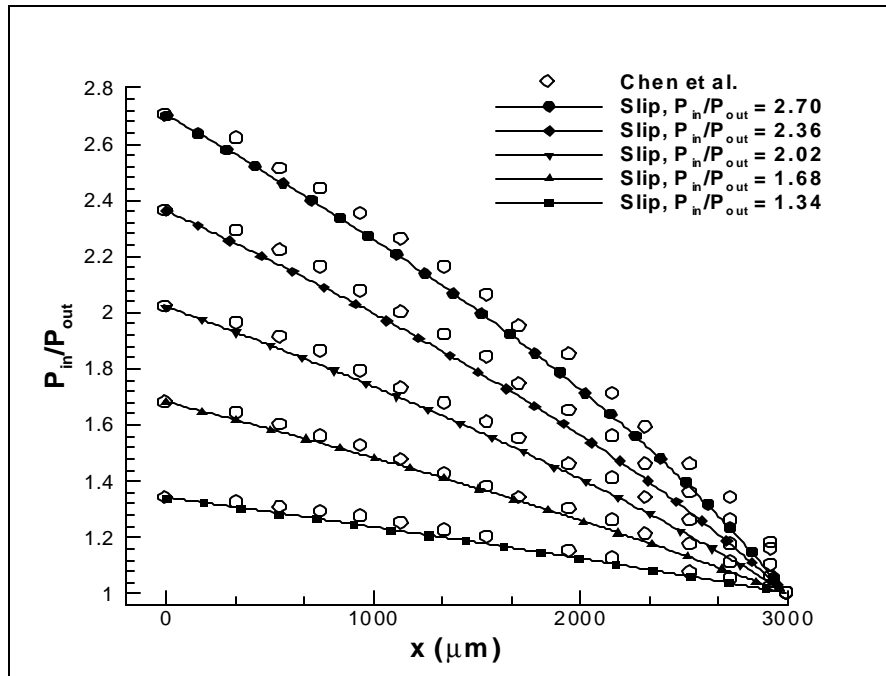
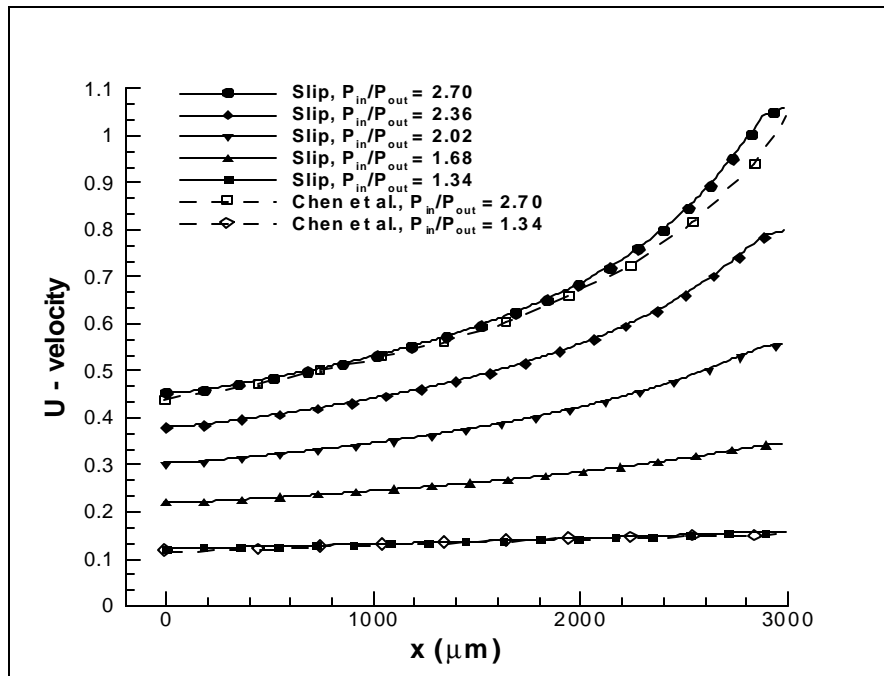


Figure 10. Comparison of the normalized centerline pressure distribution for slip results with numerical data of Chen *et al.* [49].

The slip-model streaming velocity solutions along the centerline are compared with the reported numerical results [49] for the highest (2.70) and the lowest (1.34) pressure ratios. Experimental data was not available for this study. As evident in Figure 11, the centerline velocity distribution of Chen *et al.* [49] for both pressure ratios follow closely with hydrodynamic model results validating the computationally efficient finite element model. The 1369-node finite element result matches closely with that of the 138,000-point finite difference solution for low pressure ratio while for the highest pressure ratio the finite element solution shows  $\sim 23\%$  higher exit velocity satisfying continuity. The small knee noticeable near the outlet for the streamwise velocity solution is due to the imposed vanishing gradient boundary condition. This effect does not impact the overall solution and can be reduced by generating finer mesh near the outlet.



**Figure 11.** Comparison of the centerline  $u$ -velocity distribution for slip results with numerical data of Chen *et al.* [49].

Figure 12 compares the  $u$ -velocity distribution for three sections taken across the channel length at  $x = 500, 1500$  &  $2500 \mu\text{m}$  for slip and no-slip results. With the rise in velocity downstream the corresponding centerline and wall velocity also increases. The comparison with the numerical result [49] for slip solution at  $x = 2500 \mu\text{m}$  show an almost exact match.

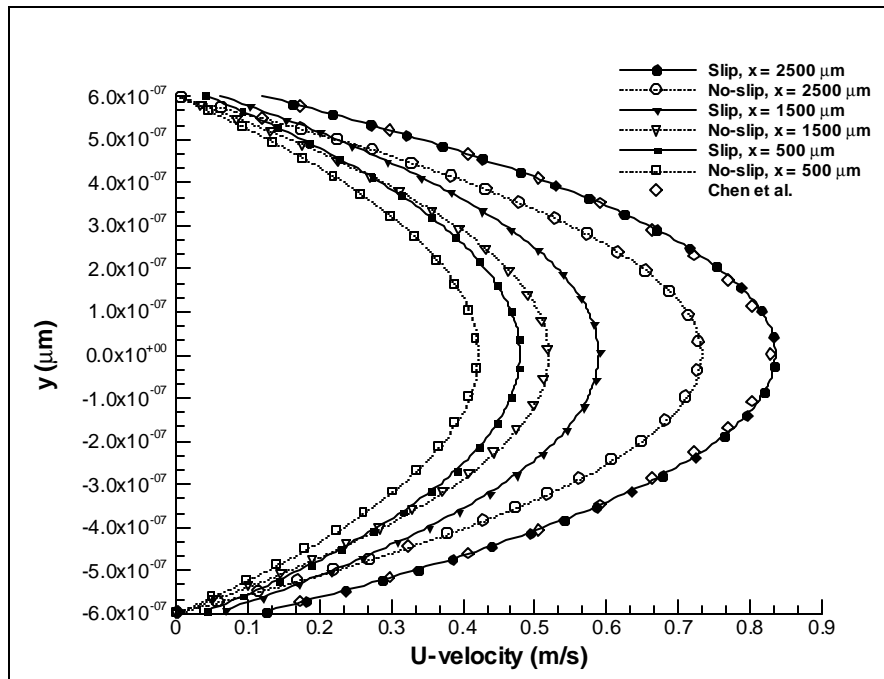
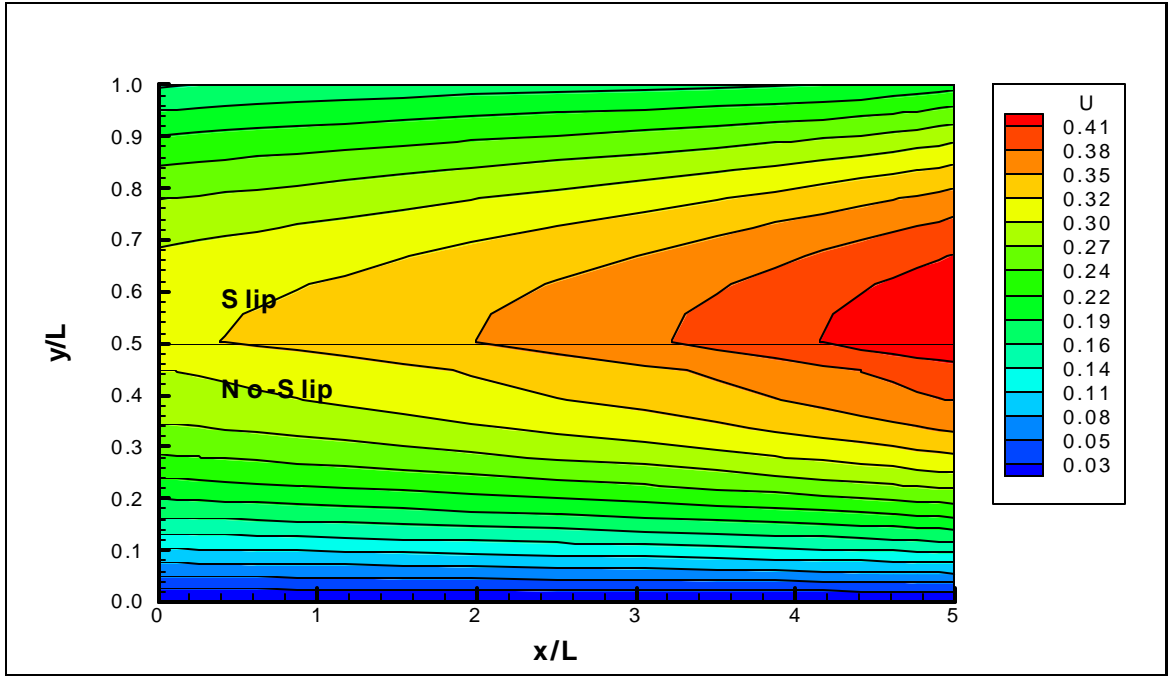
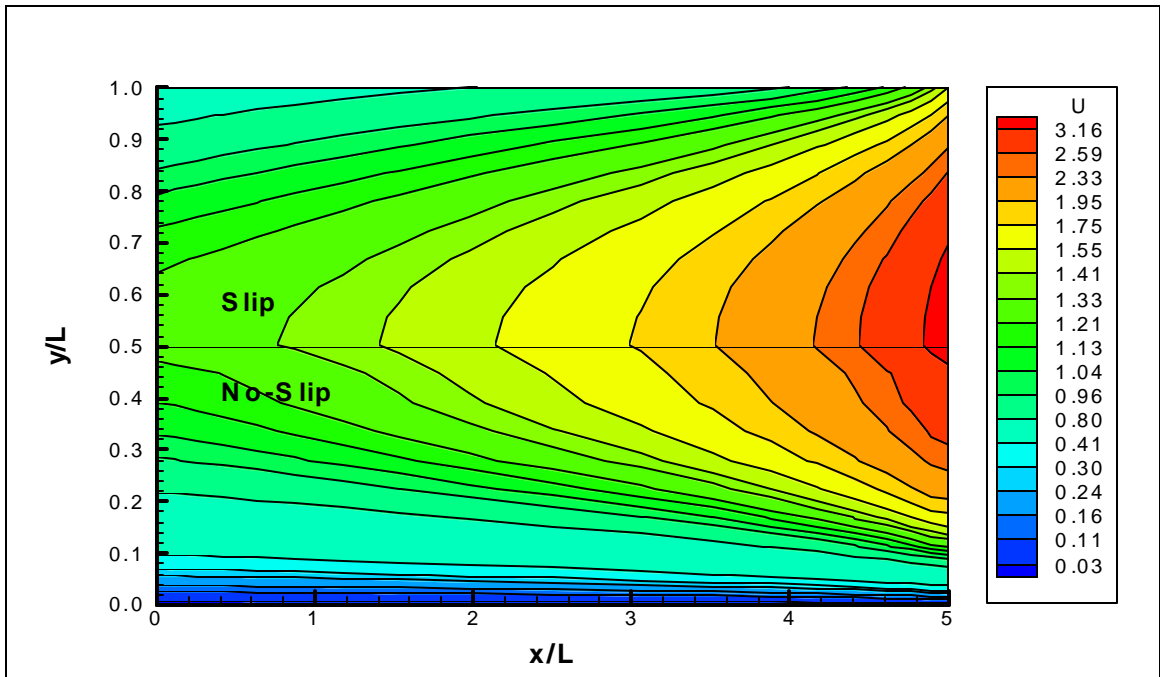


Figure 12. Comparison of the  $u$ -velocity distribution for slip results with numerical data of Chen *et al.* [49] for  $P_{in}/P_{out} = 2.70$ .

The two-dimensional streaming velocity contour plots in Figure 13(a-b) document general description and comparison of the slip and no-slip solutions for pressure ratios 1.34 and 2.70. While the no-slip solution maintains zero velocity at the wall, the slip wall solution for  $P_{in}/P_{out} = 2.70$  maintains a streaming wall velocity ranging approximately 9% (near inlet) to 15% (near exit) that of the centerline.



(a)  $P_{in}/P_{out} = 1.34$



(b)  $P_{in}/P_{out} = 2.70$

Figure 13. Two-dimensional contour plots for the streaming velocity inside the microchannel of slip and no-slip solutions for (a)  $P_{in}/P_{out} = 1.34$ , and (b)  $P_{in}/P_{out} = 2.70$ .



Finally, since the experimental data is not available the slip and no-slip mass flow rates are compared with the reported numerical results [49] in Figure 14. The maximum predicted mass flow rate is found to be  $\sim 4.6 \times 10^{-12}$  kg/s for slip solution. The slip flow comparison with the other numerical result is within  $\sim -1.5\%$ ; whereas the no-slip solution is  $\sim 12\%$  lower.

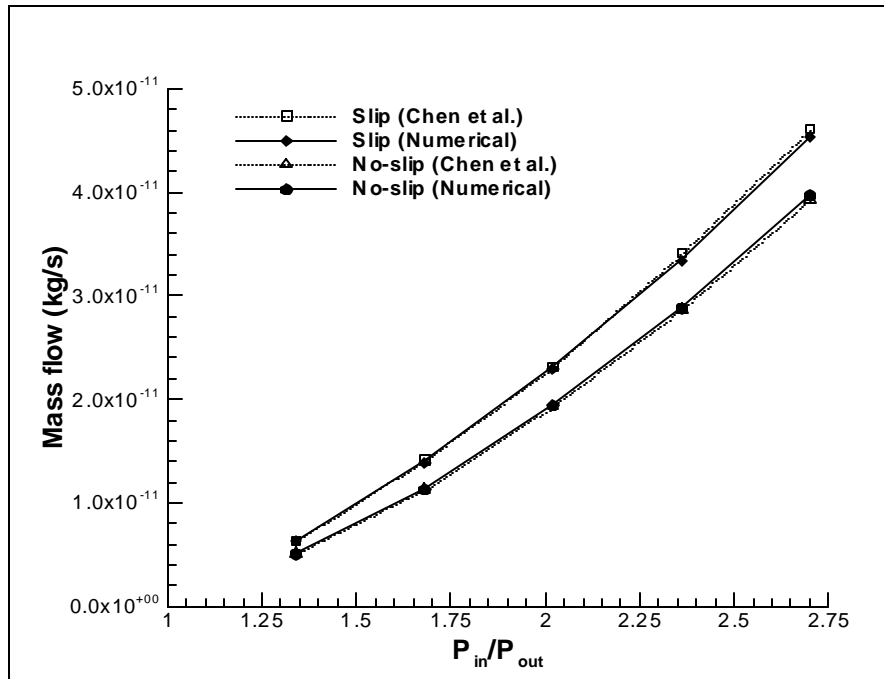


Figure 14. Mass flow rate comparison of the slip and no-slip solution with the corresponding numerical result of Chen *et al.* [49].

## Case II

This case is based on the experiment of Shih *et al.* [40]. This is an extension of the experimental study by Pong *et al.* [38] for a different length of microchannel. The channel is  $4000 \mu\text{m}$  long and  $1.2 \mu\text{m}$  high with an aspect ratio of 3333. Experimental data was collected using thirteen pressure transducers of  $250 \times 250 \mu\text{m}^2$  area connected at

intervals of 400  $\mu\text{m}$  along the length of the channel. The gas used in this case was Helium having an outlet Knudsen number of 0.17 at atmospheric conditions indicating transition regime. The computational geometry is discretized using 28 x 20 two-dimensional 9-noded non-overlapping bi-quadratic finite elements consisting of a total of 2337 nodes.

For four different pressure ratios, the experimental measurements of the pressure distribution show also a non-linear trend, which are closely (within  $-2\%$ ) matched by the numerical slip data as plotted in Figure 15. The pressure drop occurs to overcome the shear stresses in the channel. With a slip boundary the flow encounters lesser frictional forces on the wall than no-slip boundary, which tends to make the slip flow more linear as compared to the no-slip flow.

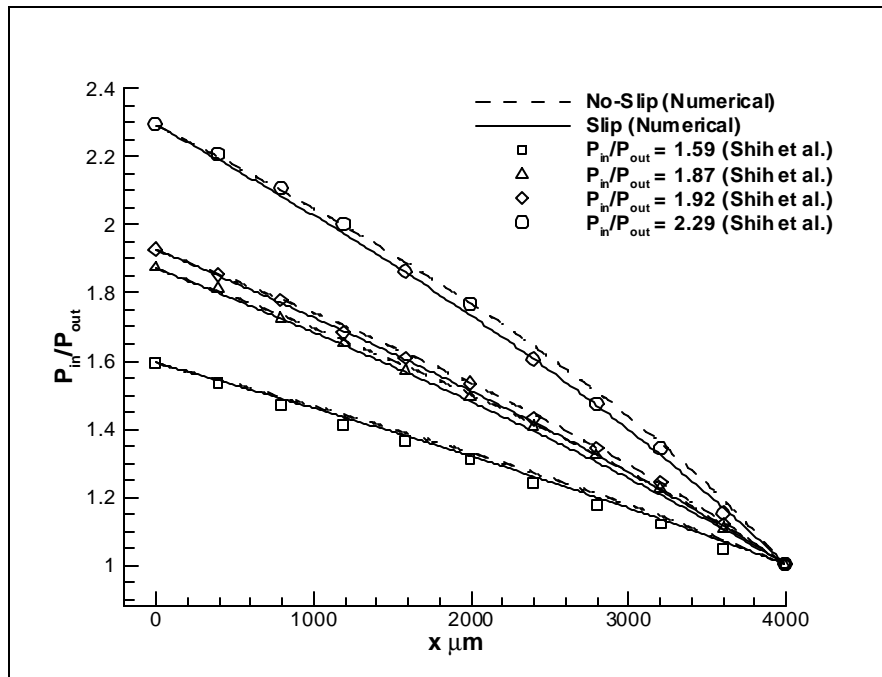


**Figure 15.** Comparison of the normalized centerline pressure distribution for slip and no-slip results with the experimental data of Shih *et al.* [40].

Since the temperature changes are negligible the density variation is proportional to the pressure change. Due to mass flux conservation, velocity increases as the density and pressure drop; however the values remain considerably low indicating a sub-sonic flow, Figure 16. The slip flow yields a higher velocity than the corresponding no-slip flow. For a  $P_{in}/P_{out} = 2.29$ , this difference is approximately +21% near the outlet.

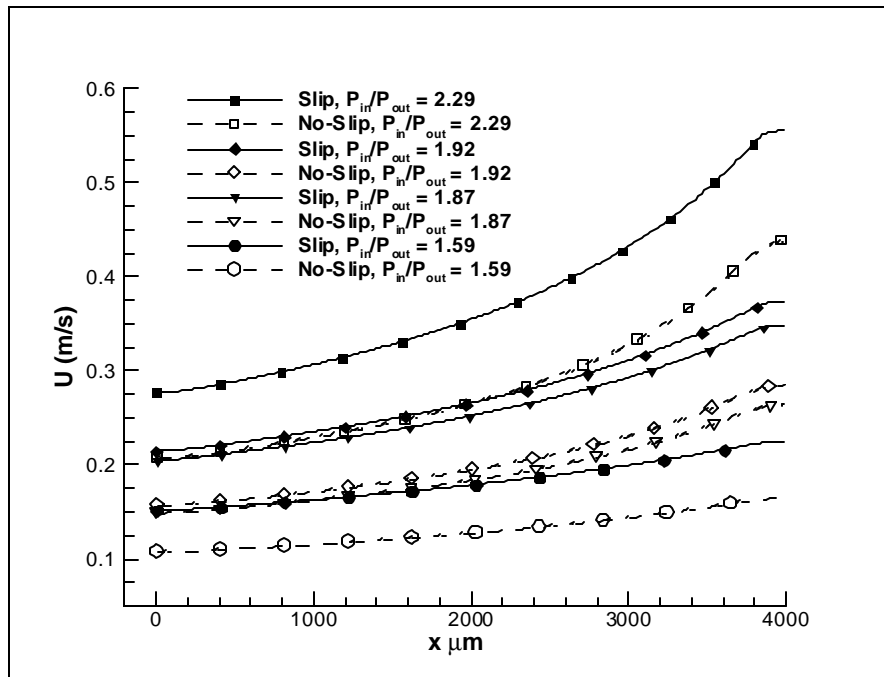


Figure 16. Comparison of the centerline  $u$ -velocity distribution for slip and no-slip solutions for *Case II*.

A similar effect is also visible in Figure 17 where different cross-sections along the  $y$ -direction show increase in streamwise velocity with a corresponding rise in wall velocity due to slip. As  $Kn$  increases due to reduced density downstream, the slip effect increases.

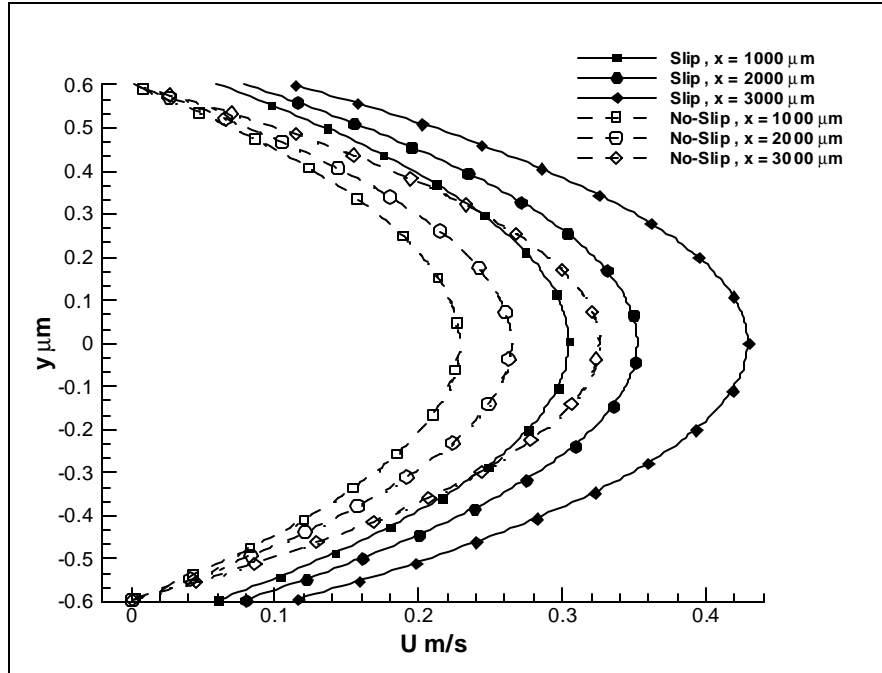


Figure 17. Comparison of the  $u$ -velocity for slip and no-slip condition in the  $y$ -direction at three different sections along the length of the microchannel for  $P_{in}/P_{out}=2.29$ .

Figure 18 shows considerable (orders of magnitude) difference in velocity in slip and no-slip crosswise ( $v$ ) velocity component. However, it is significantly smaller in the magnitude ( $10^{-6}$  m/s) than the streamwise ( $u$ ) velocity which is of the order of  $10^{-1}$  m/s. This indicates that pressure difference in the crosswise direction is comparatively negligible. The only other experimental data available for this case is the mass flow rate, which has been compared with the slip and no-slip solutions. The experimental data with  $\pm 3\%$  error bar has been plotted in Figure 19 validating the other two numerical solutions for five data points. The maximum mass flow rate is found to be  $\sim 6.82 \times 10^{-12}$  kg/s for helium. The slip flow comparison with the experimental data is within  $\sim -8\%$ ; whereas the no-slip solution is  $\sim 28\%$  lower.

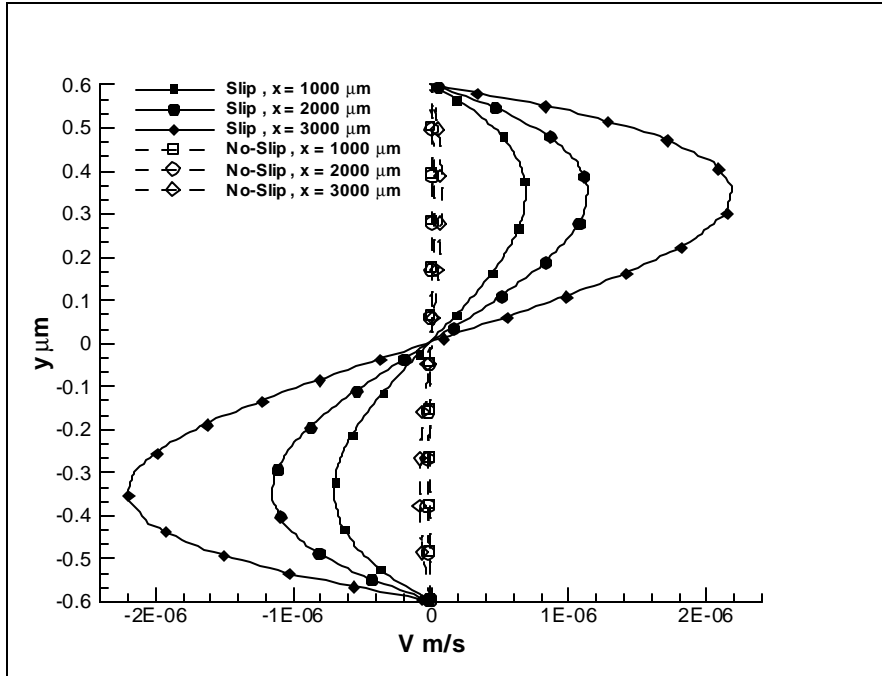


Figure 18. Comparison of the  $v$ -velocity for slip and no-slip condition in the  $y$ -direction at three different sections along the length of the microchannel for  $P_{in}/P_{out}=2.29$ .

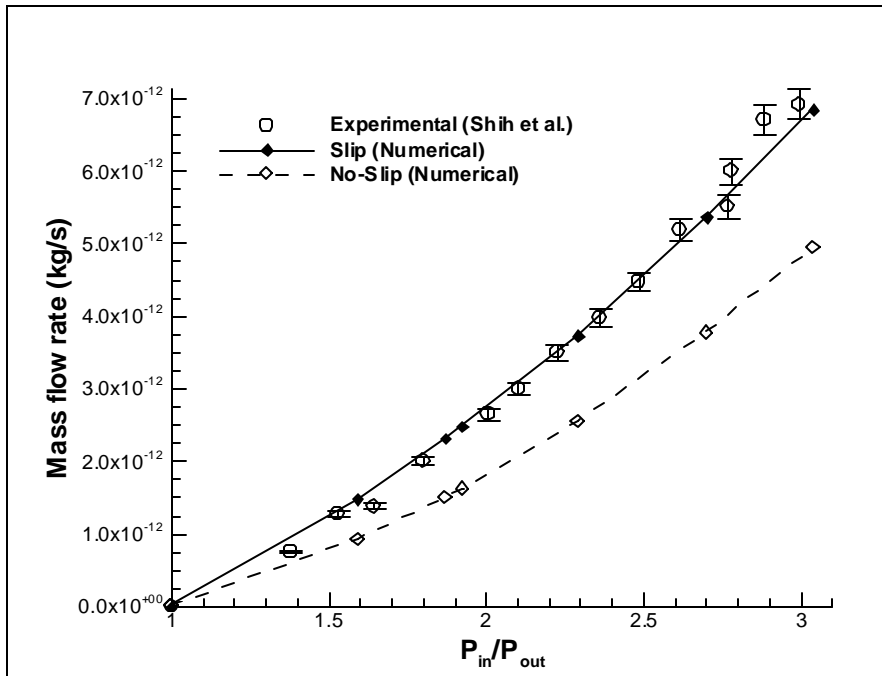


Figure 19. Mass flow rate (kg/s) obtained by slip and no-slip conditions as compared to the slip and no-slip mass flow rate with the experimental data Shih *et al.* [40].

### **Case III**

This representative case of low Reynolds number flow through a microchannel was documented by Arkilic *et al.* [42]. The channel has an aspect ratio of 5639 having a length of 7500  $\mu\text{m}$  and 1.33  $\mu\text{m}$  height. It was manufactured using a two-wafer manufacturing process by etching an oxide grown on silicon. The experiment was based on measuring the mass flow rate through the channel for Helium and other gases. For this case only Helium has been used. The outlet condition is atmospheric, similar to the first two cases.

Five different pressure ratios are used between 1.34 and 2.70, based on inlet pressure, yielding a maximum Knudsen number of 0.155 (transition regime) at the outlet. The computational geometry is the same as *Case II*, consisting of 28 x 20 finite elements as compared to Chen *et al.*'s [49] 6000 x 23 finite difference mesh. Figure 18 plots the slip and no-slip hydrodynamic solution variables showing a similar trend as *Case I* in terms for a non-linear distribution of pressure. The maximum difference in slip and no-slip solutions is ~4% for pressure as shown in Figure 20. The velocity profiles for the slip and no-slip solutions have been compared for  $P_{in}/P_{out} = 1.34$  & 2.70 and the maximum difference is found to be ~24% for velocity as shown in Figure 21.

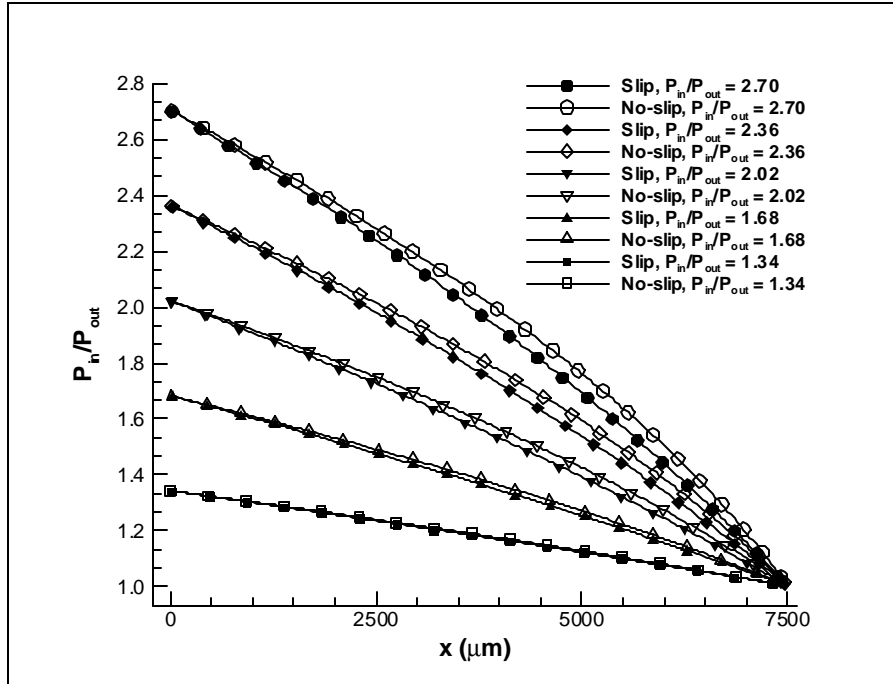


Figure 20. Comparison of the normalized centerline numerical slip and no-slip pressure distribution for Case III.

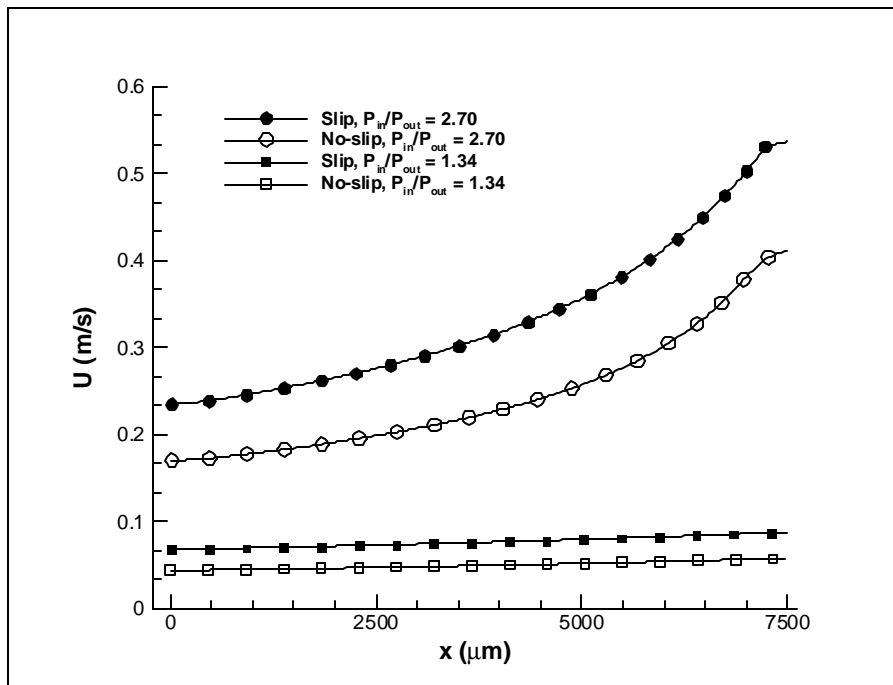


Figure 21. Comparison of the centerline slip and no-slip streamwise velocity solutions for Case III.

Figure 22 compares the distribution of  $u$ -velocity in the  $y$  direction for three crosswise sections taken along the length of the channel. A change in the centerline velocity is reflected on the wall velocity where wall velocity at  $x = 5625 \mu\text{m}$  is  $\sim 50\%$  more than that at  $x = 1875 \mu\text{m}$ . This also confirms the effect of slip with increasing  $Kn$ , which rises in the downstream region.

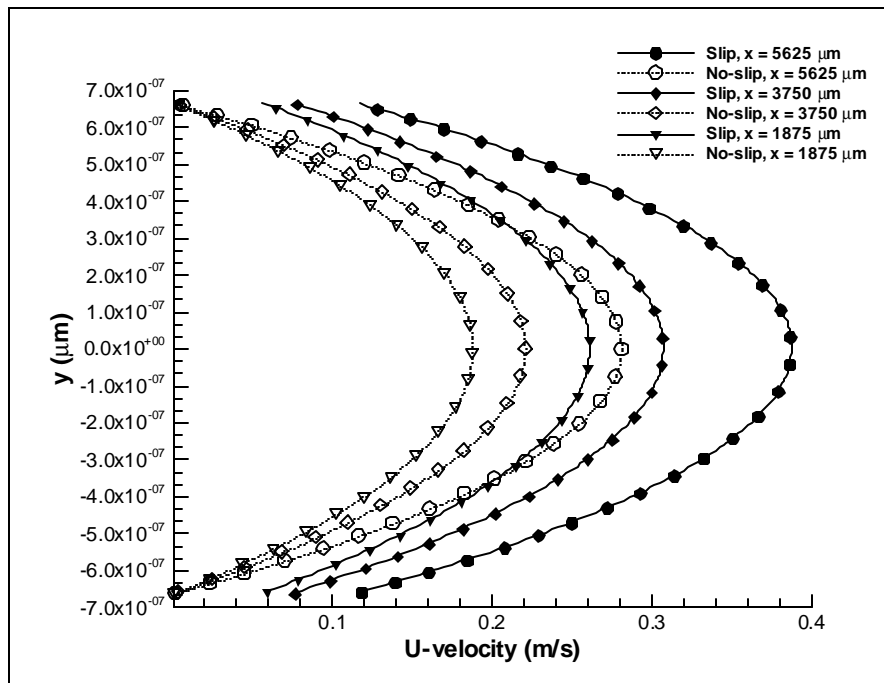


Figure 22. Comparison of the  $u$ - velocity for slip and no-slip condition in the  $y$ -direction at three different sections along the length of the microchannel for  $P_{in}/P_{out}=2.70$ .

The mass flow rates for microchannel have been compared with both the experimental data [42] and numerical solution [49] in Figure 23. The slip flow differs by only  $\sim +2.5\%$  with numerical slip-solution and a maximum of  $+7\%$  from the experimental data. The mass flow rate for the slip solution is  $\sim 35\%$  higher than the no-slip solution.



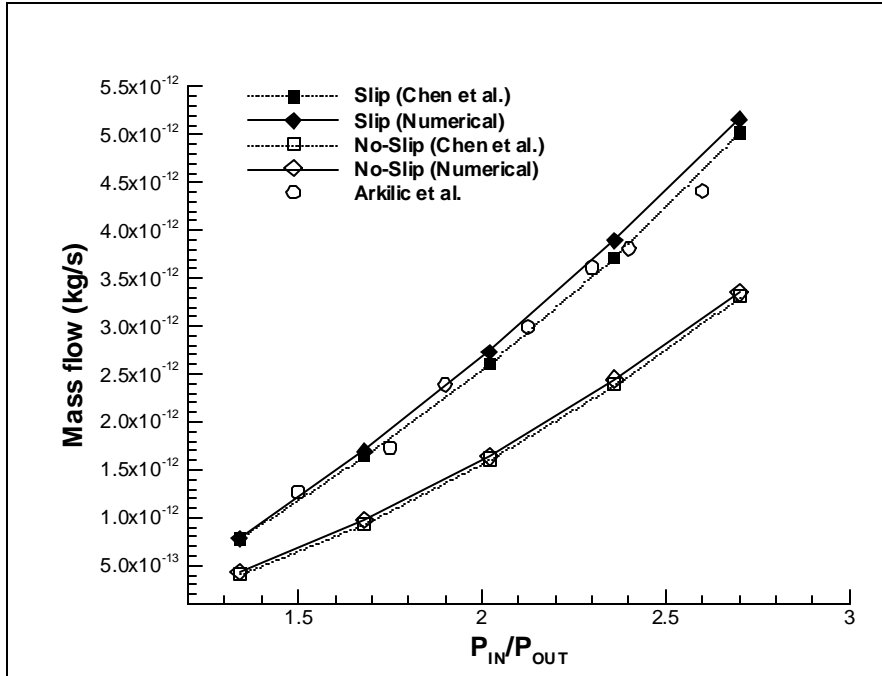


Figure 23. Comparison of mass flow rate (kg/s) obtained by slip and no-slip conditions to the experimental data of Arkilic *et al.* [42] and the numerical slip and no-slip mass flow rates from Chen *et al.* [49].

#### IV. MODELING OF SUPERSONIC GAS FLOW THROUGH MICROCHANNEL

Most of the experiments for flow through microchannels are based on subsonic or pressure driven flows having low Reynolds number. However, for some particular applications like in the aerospace industry high speed flows maybe encountered. DSMC [21, 53-54] and Burnett equation models [24] are the popular methods for analyzing the low and heat transfer characteristics of high speed gas flows in microchannels since they give a better resolution for gas to surface interactions. Several investigators have used the DSMC approach especially in case of high-speed flows where the Kn is relatively high [21, 53-54]. This section aims to extend the applicability of hydrodynamic model to investigate flow and heat transfer characteristics of high-speed flows through microchannels having a Knudsen number range of 0.062 – 0.14 for two different gases, helium and nitrogen. The results have been compared to the available DSMC results of Oh *et al.* [21] and Liou *et al.* [53].

##### **Model Geometry**

The two-dimensional microchannel model shown in Figure 24 is an extension of the experimental setup of Pong *et al.* [38] used to study Poiseuille flow through long microchannels. The channel geometry have been modified by Oh *et al.* [21] to a shorter length of 6  $\mu\text{m}$ , in order to obtain hypersonic flow conditions. This reduces the aspect ratio to  $L/H = 5$ . The value of Knudsen number for the working fluid helium is 0.14 for

this case. Another case was presented by Liou *et al.* [53] is similar to that of Oh *et al.* [21] in terms of dimensions. However the working fluid is nitrogen for this case giving a lower Knudsen number of 0.062. The microchannel dimensions and flow parameters are enlisted in the Table 2. The flow is simulated at near atmospheric conditions. A free stream region **B** is specified near the inlet section of the microchannel where the specular reflection of gas molecules takes place and the flow develops. Similar boundary conditions have been specified for both cases.

Table 2

Model Dimensions and Flow Parameters for Supersonic Gas Flows

<b>Parameters</b>	<b>Case 1</b> (Liou <i>et al.</i> [53])	<b>Case 2</b> (Oh <i>et al.</i> [21])
Fluid	Nitrogen	Helium
<b><i>L</i></b> ( <i>mm</i> )	6.0	6.0
<b><i>H</i></b> ( <i>mm</i> )	1.2	1.2
<b><i>B</i></b> ( <i>mm</i> )	0.6	1.0
<b>Kn</b>	0.062	0.14
<b><i>T<sub>o</sub></i></b> ( <i>K</i> )	300	298
<b><i>T<sub>w</sub></i></b> ( <i>K</i> )	323	298
<b>Ma<sub>o</sub></b>	4.15	5.0
<b><i>P<sub>o</sub></i></b> ( <i>Pa</i> )	1.01 x 10 <sup>5</sup>	1.01 x 10 <sup>5</sup>
<b><i>R</i></b> ( <i>J/kg.K</i> )	296.8	2076.9
<b><i>C<sub>p</sub></i></b> ( <i>J/kg.K</i> )	1039.0	5192.6
<b><i>m</i></b> ( <i>N-s/m<sup>2</sup></i> )	1.85 x 10 <sup>-5</sup>	2.066 x 10 <sup>-5</sup>
<b><i>k</i></b> ( <i>W/k.m</i> )	0.0259	0.152
<b><i>i</i></b>	1.40	1.667

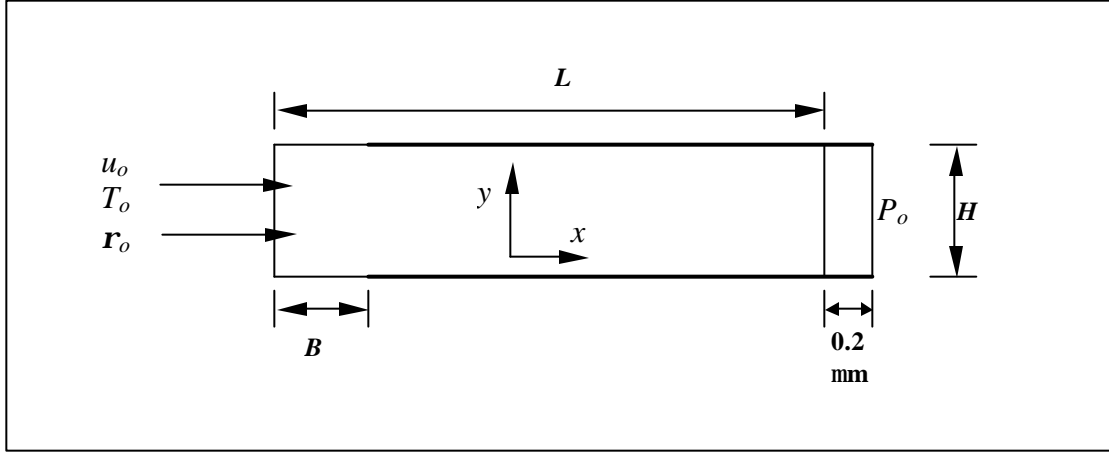


Figure 24. Schematic of microchannel geometry for supersonic gas flows. [21]

### Boundary Conditions

For both cases the inlet boundary is fixed for velocity  $u_o$  (based on Mach number,  $Ma_o$ ), temperature  $T_o$  and the density  $\rho_o$  (based on inlet pressure,  $P_o$ ) as listed in Table 2. The wall temperature for the top and the bottom surface is set to be  $T_w$ . The velocity flux is  $\partial u/\partial x=0$  at the outlet and the  $y$ -component of the velocity  $v$  vanishes at the inlet. A backpressure equal to the inlet boundary pressure is specified at the outlet. The drawback faced for modeling this problem is that outflow boundary conditions could not be replicated since the exact location of the outlet pressure is not clear in any of the references [21, 53]. A backpressure  $P_o = 1.01 \times 10^5$  Pa has been specified 0.2  $\mu\text{m}$  downstream from the exit.

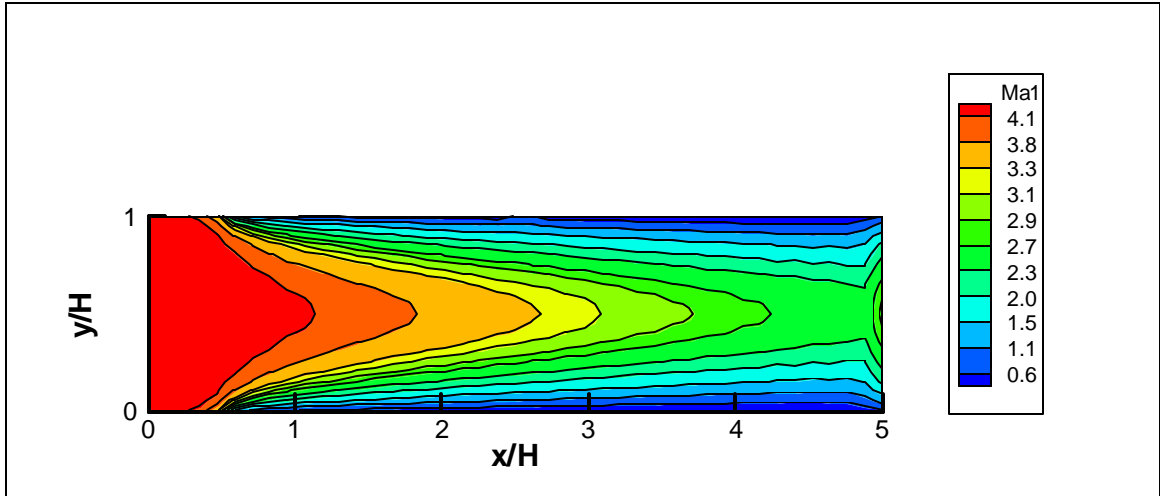
Near the entrance, the wall boundary for the length  $B$  (“lighter wall”) is defined by the accommodation coefficients of  $\mathbf{s}_V = \mathbf{s}_T = 0.0$ , implying a specular reflection where only the tangential component of velocity of the impinging molecules is conserved making it a freestream region consistent with the DSMC models. In the rest of the

domain (“darkened walls”), the gas to wall interaction is set with  $s_V = s_T = 1.0$  implying the gas molecules undergo a complete change in momentum after collision.

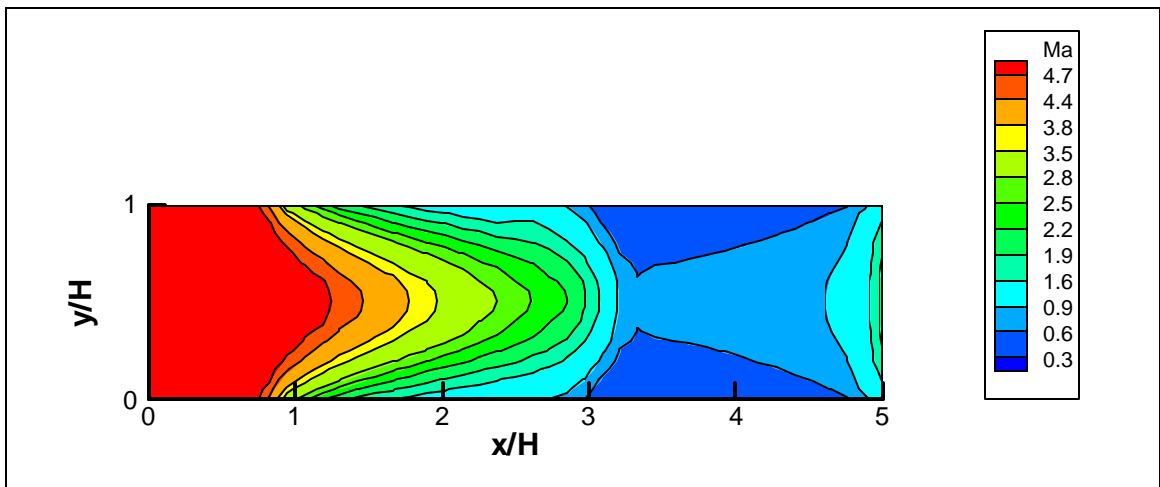
### **Results and Discussion**

A single computational grid is used for both cases consisting of 560 finite elements and 3485 nodes. Although for microchannels with high aspect ratios only 1369 and 2337 node grids was used earlier for the subsonic flow cases, here a finer mesh is utilized for capturing better resolution of the high speed flow characteristics. In order to keep the consistency with the numerical report the length in  $x$ -direction is considered for the length mentioned in Table 2 ignoring the extra length of  $0.2 \mu\text{m}$  for both cases. Here onwards in this chapter, *Case I* is referred as  $\text{Kn} = 0.062$  and *Case II* as  $\text{Kn}=0.14$ .

For *Case I* the Mach number contours show shocks emerging from the walls move towards the center of the channel causing a distortion just ahead of the freestream section. The drop in the Mach number is smooth along the channel as is seen in Figure 25(a). However, for *Case II* the contours in Figure 25(b) plot a relatively sharper drop in velocity creating normal bow shock structures near  $x/H = 3.2$ . A constriction in flow is observed near this region which indicates the prevailing viscous effects for the higher Knudsen number cases.



(a)

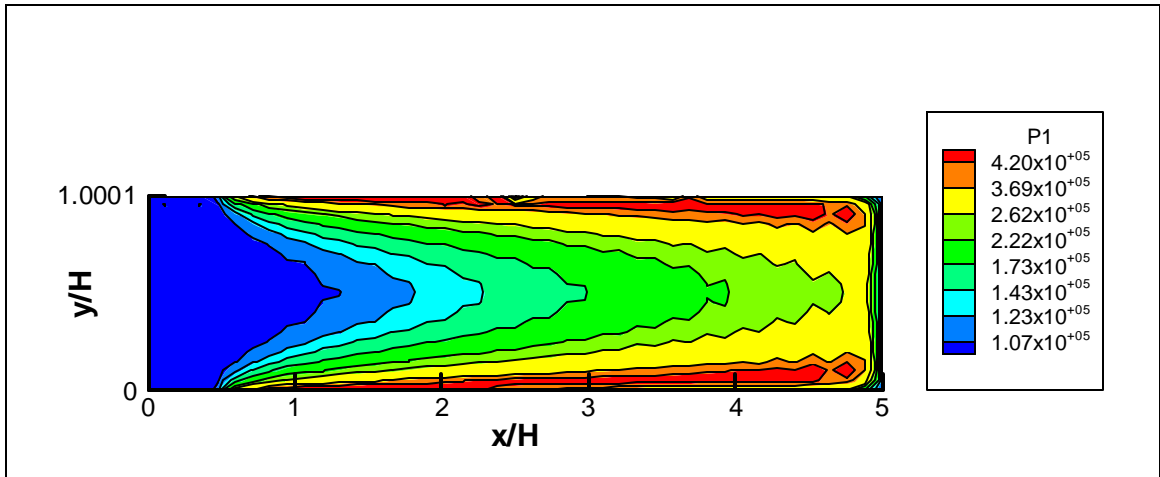


(b)

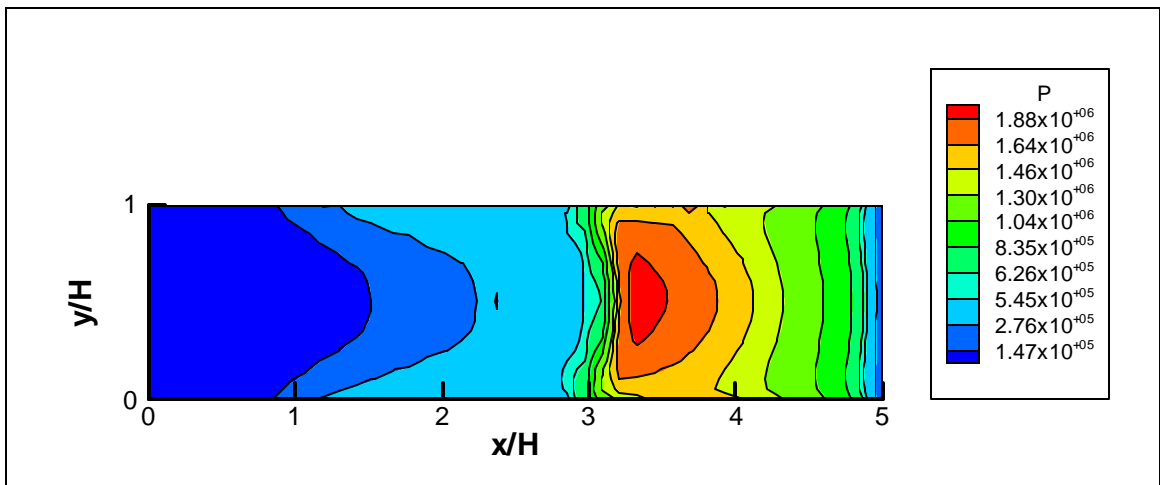
Figure 25. Mach number contours for (a)  $Kn=0.062$  and (b)  $Kn = 0.14$ .

The effect of backpressure is minimal for  $Kn = 0.062$  shown in Figure 26(a), where Nitrogen is used as working fluid. The high pressure regions are seen only near the walls for this case. The pressure contours for  $Kn = 0.14$  show the dominance of the backpressure near the exit. The shock waves stemming from the leading edges and the exit meet at  $x/H = 3.2$ , Figure 26(b). The highest pressure is seen at this region of intersection. The density contours shown in Figure 27 have similar profile as that of the

pressure for both cases. Clearly, the fluidity of Helium makes it more interesting with shock-wall layer interactions. A sharp density rise follows the pressure rise with similar shock structures.

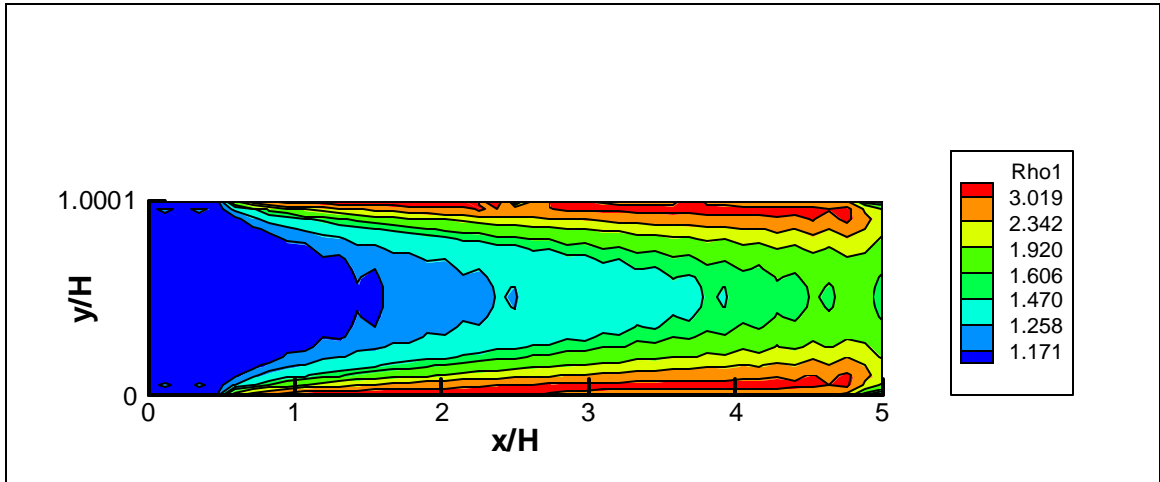


(a)

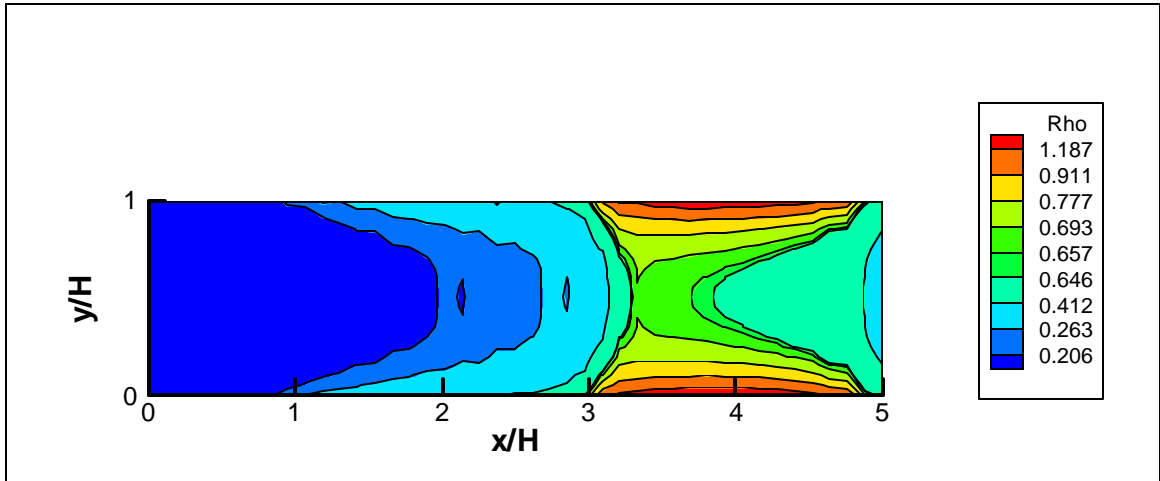


(b)

Figure 26. Pressure contours in Pa for (a)  $Kn=0.062$  and (b)  $Kn = 0.14$ .



(a)



(b)

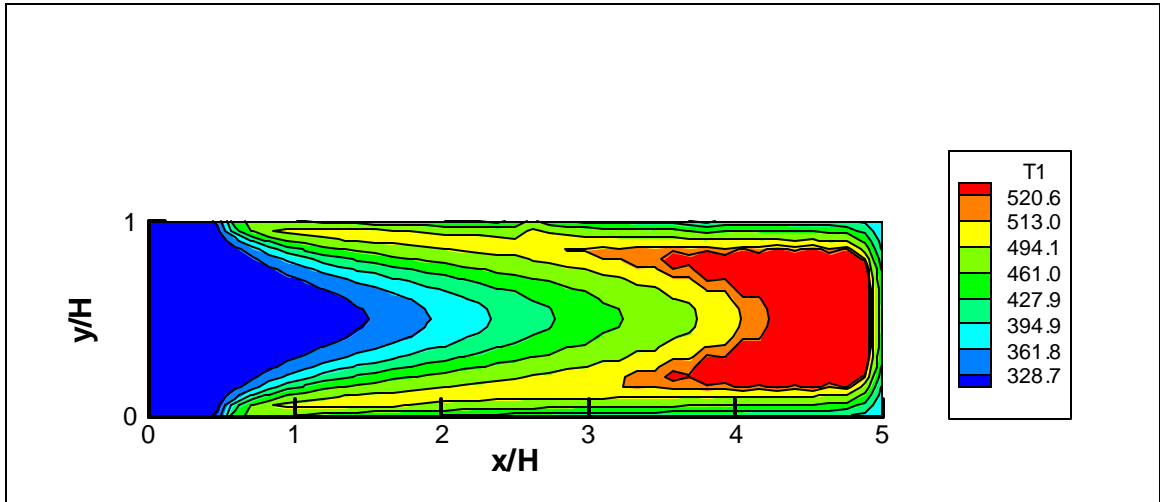
Figure 27. Density contours in  $\text{kg/m}^3$  for (a)  $\text{Kn}=0.062$  and (b)  $\text{Kn} = 0.14$ .

The temperature contours in Kelvin for the two cases are plotted in Figure 28.

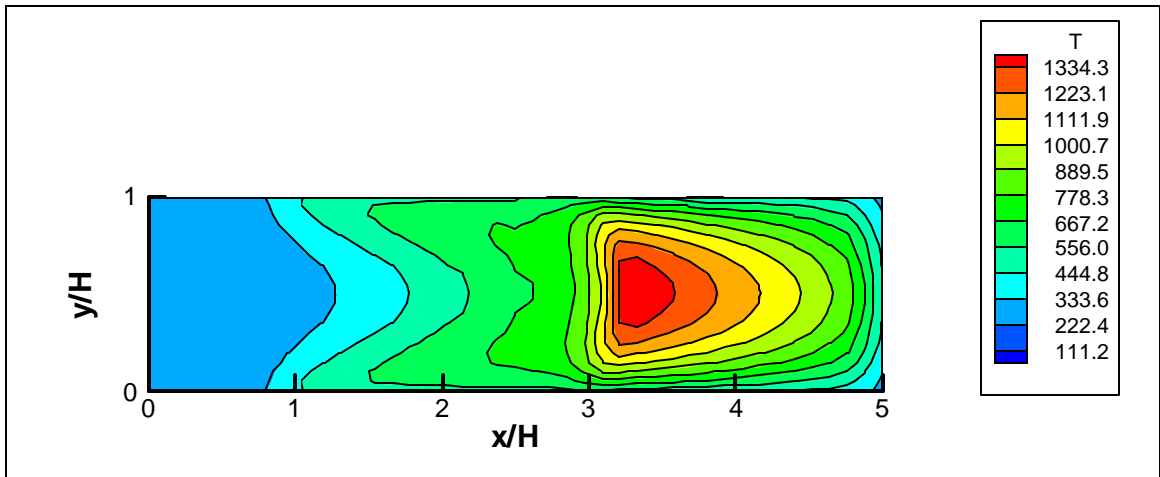
Due to shock the thermal boundary is not completely developed for  $\text{Kn} = 0.062$ . The rise in the temperature is seen the downstream region near the exit, Figure 28(a) at nearly  $x/H=4.2$ . This temperature jump is documented upstream for  $\text{Kn}=0.14$  at nearly  $x/H=3.4$  due to the increase in thermal boundary layer as shown in Figure 28(b). The shock



structure for  $Kn = 0.14$  causes a hot spot at the center corresponding to the shock region created by the backpressure.



(a)

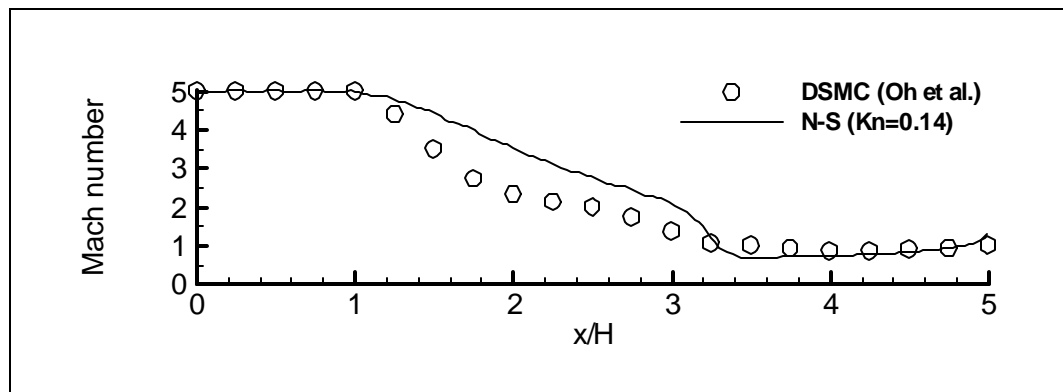


(b)

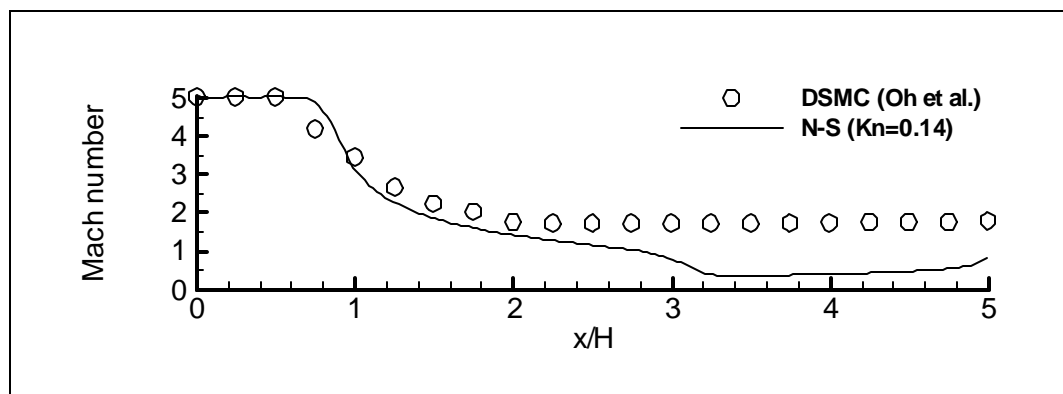
Figure 28. Temperature contours for (a)  $Kn=0.062$  and (b)  $Kn = 0.14$ .

Since no experimental data is available for these cases, the first order Navier-Stokes solutions have been compared with reported DSMC results [21] for  $Kn = 0.14$ . However, the centerline and near wall profiles are not available for comparison for  $Kn =$

0.062 except for the temperature,  $T$ . The Mach number distribution along the centerline and near wall section of the flow in the streamwise direction is plotted for  $Kn = 0.14$  in Figure 29(a-b). The centerline Mach number for this case shows a good comparison in the upstream and downstream region with DSMC results. In the mid-region, the observed deviation could be due to the difference in the specification of the location of backpressure as described before. The near wall distribution in Figure 29(b) also shows a similar comparison with even exaggerated effect of the shock waves on the walls in the downstream region. The Mach number ranges from 5.0 to nearly 1.0.



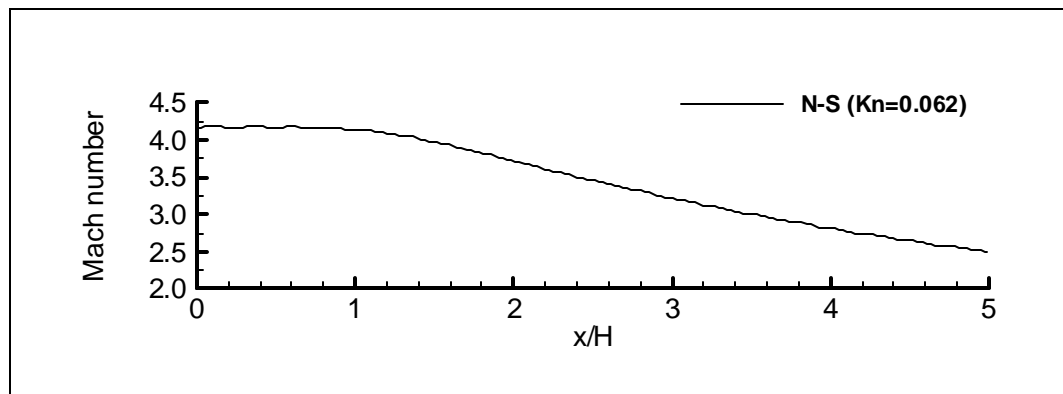
(a)



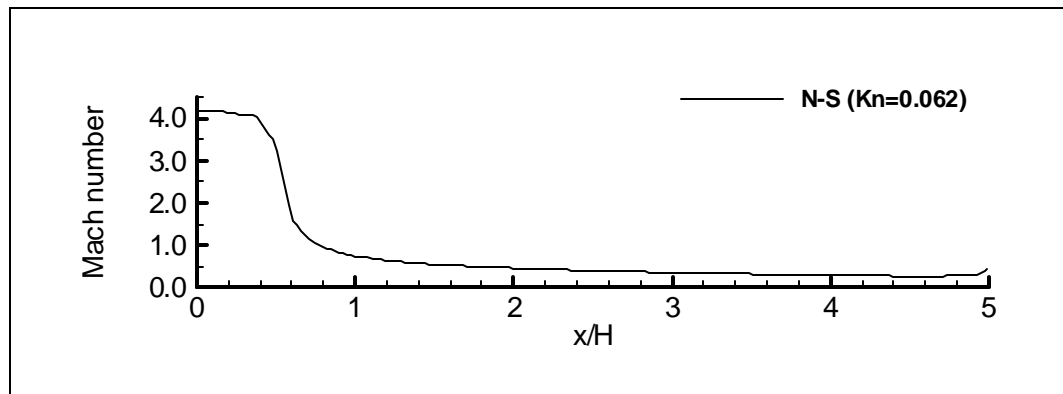
(b)

Figure 29. Comparison of, (a) centerline and (b) near wall, Mach number distribution of both N-S solutions with available DSMC results [21] for  $Kn = 0.14$ .

Figure 30 compares the centerline and near wall Mach number distribution for  $Kn = 0.062$ . Plotted solution in Figure 30(a) shows a smoother drop in the Mach number along the channel centerline as compared to the  $Kn = 0.14$ , Figure 29(a). The solution near the walls of the microchannel plotted in Figure 30(b) shows that Mach number undergoes a drop immediately after the freestream region and there after remains nearly steady. Since no such data at this Knudsen number is reported elsewhere there is no means for direct comparison with the literature.



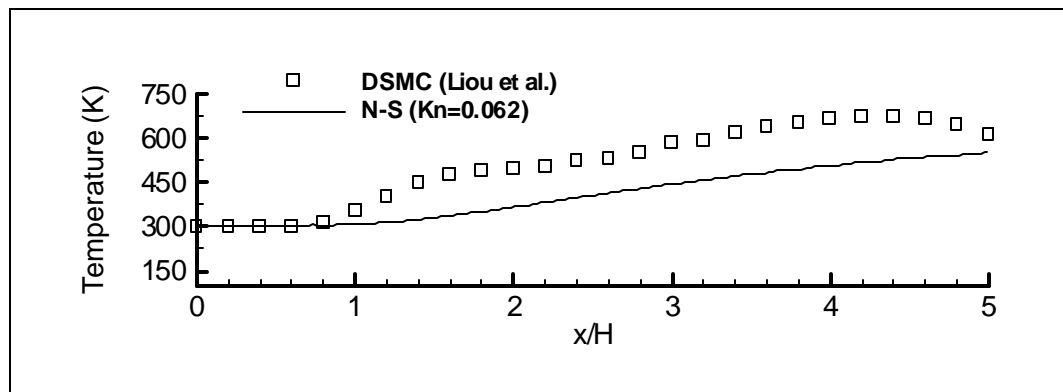
(a)



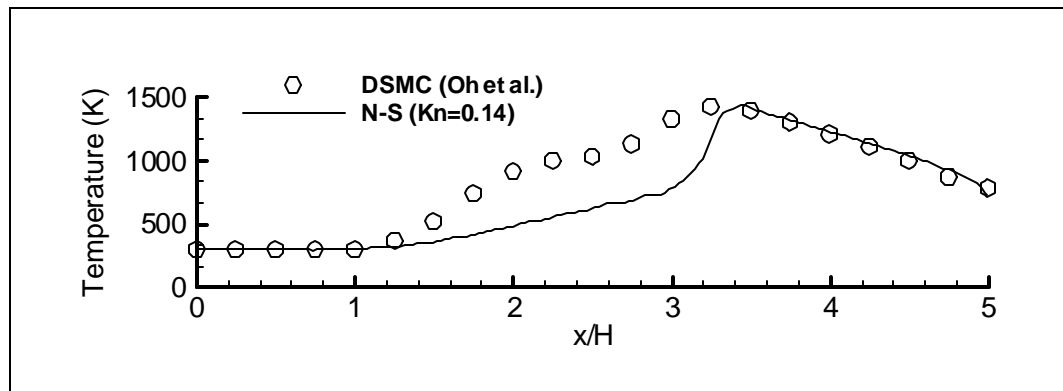
(b)

Figure 30. Mach number distribution of  $Kn = 0.062$  case, (a) at the centerline and (b) near the wall.

The centerline distribution of temperature for the two cases has been compared with both DSMC results [21, 53] in Figures 31(a-b). For  $Kn = 0.062$ , the temperature trend shows a steady rise indicating a gradual development of the thermal boundary layer with a maximum difference of 100 K in the peak value prediction. For  $Kn = 0.14$ , temperature profiles match in upstream and downstream region like the Mach number. The peak for the temperature matches closely with the referred data. However, compared to the DSMC result, the normal shock-like structure for the hydrodynamic solution is noticeable in Figure 31(b).



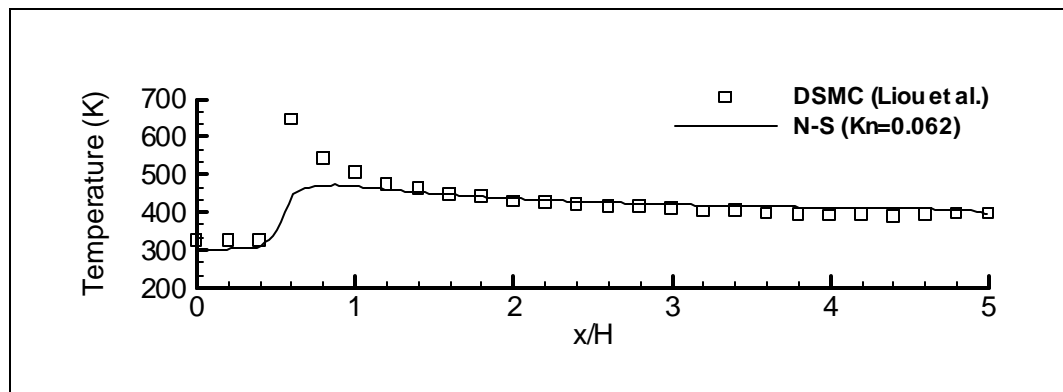
(a)



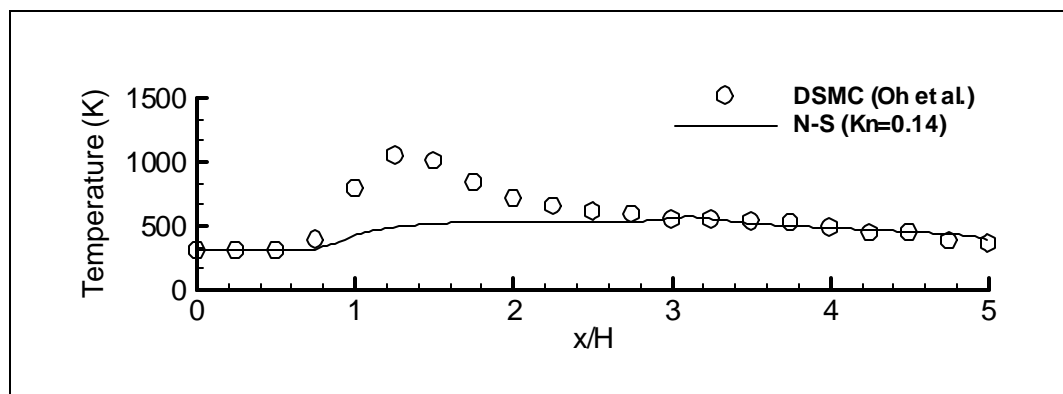
(b)

Figure 31. Comparison of centerline distribution of temperature compared with the available DSMC results for (a)  $Kn = 0.062$  and (b)  $Kn = 0.14$ .

Figure 32(a) shows the near wall temperature distribution for  $Kn = 0.062$  where the peak values of the N-S simulation differ from the DSMC results [53] at the end of freestream region; however for the rest of the domain the values match closely. The solution plotted in Figure 32(b) for  $Kn=0.14$  shows that the temperature near the walls remains below 600 K at all places. Deviation from published DSMC result [21] is observed in the region from  $x/H = 0.8$  to 2.2. However similar deviation in temperature distribution has also been documented for Burnett equation solutions [24] for low Knudsen number ( $Kn=0.07$ ) in comparison with the DSMC results.



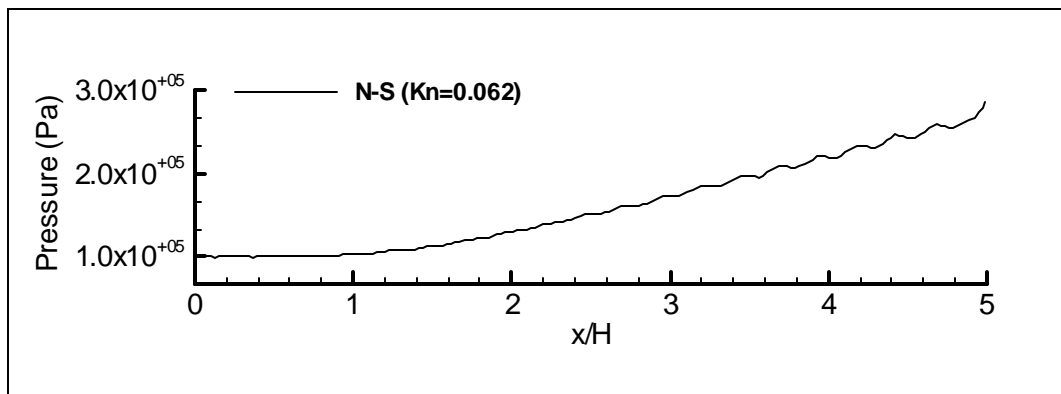
(a)



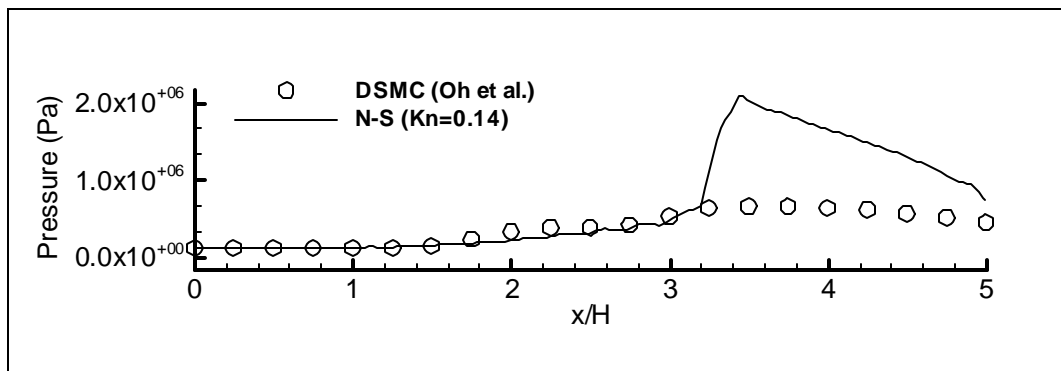
(b)

Figure 32. Comparison of near wall distribution of temperature compared with the available DSMC results for (a)  $Kn = 0.062$  and (b)  $Kn = 0.14$ .

The centerline pressure distributions for  $Kn = 0.062$  and  $Kn = 0.14$  are presented in Figure 33 and compared for  $Kn = 0.14$  with the DSMC result [21]. The presence of backpressure plays a dominant role in determining the solution characteristic. For  $Kn = 0.62$  the presence of backpressure is minimal giving a steady rise in pressure near the outlet however, giving an oscillatory solution. For  $Kn = 0.14$  comparison in Figure 33(b) shows steady rise in the pressure indicating a more diffused solution for the DSMC results. Contrarily, the hydrodynamic solutions captures a sharp shock around  $x/H = 3.2$ . Note that the inlet Mach number for Case 2 is 5.0.



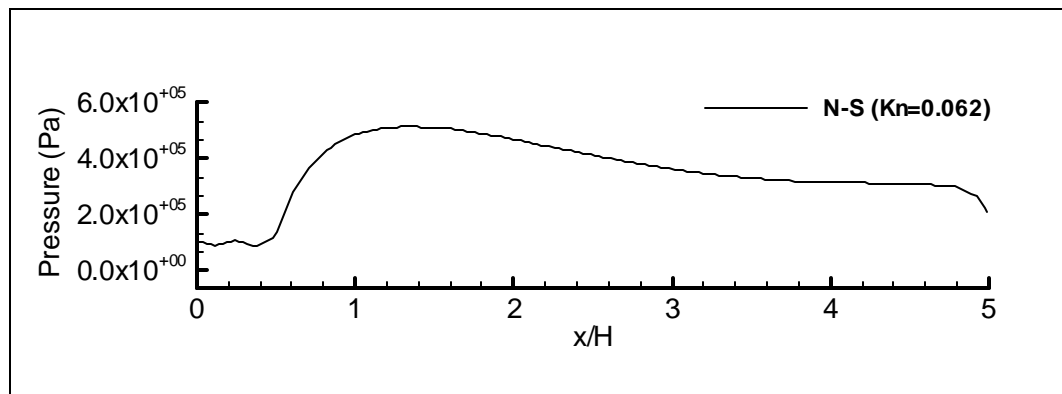
(a)



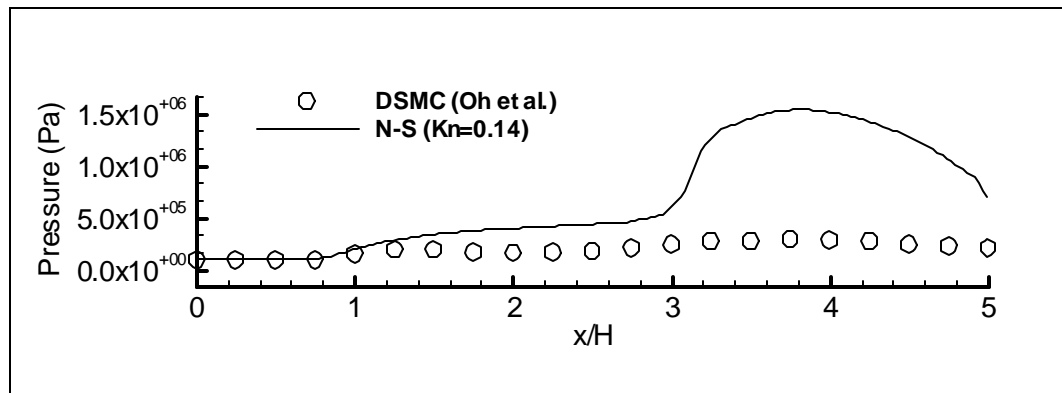
(b)

**Figure 33.** Centerline pressure distribution of N-S solutions for (a)  $Kn = 0.062$  and (b)  $Kn = 0.14$  in comparison with DSMC results [21].

Figure 34 plots the solution prediction near the wall along the streamwise direction to indicate the slip effects for  $Kn = 0.062$  and  $Kn = 0.14$ . For  $Kn = 0.062$  the pressure profiles reflect the presence of shock structures near the leading edges of the channel, as shown in Figure 34(a). However, in comparison for  $Kn = 0.14$  the dominance the shock near the walls due to the backpressure is visible for the pressure profile, Figures 34(b). The shock emanating from the walls is the highest near  $x/H=3.2$  at the centerline. The shock structures obtained for the Navier-Stokes solutions are found to be higher when compared to DSMC predictions.



(a)



(b)

**Figure 34.** Near wall pressure distribution of N-S solutions for (a)  $Kn = 0.062$  and (b)  $Kn = 0.14$  in comparison with DSMC results [21].

The difference in the shock indicates that the DSMC solutions are much more diffused in comparison to the N-S solutions. While the reason for this discrepancy is not clear and the experimental verification is unavailable, the author presumes that the specification of exit boundary condition is the possible cause. For *Case 2*, the DSMC model has exit boundary consisting of virtual cells where the backpressure is updated continuously by the equation of state [21], unlike the fixed pressure boundary in the hydrodynamic solution.

Figure 35 shows the distribution of the Mach number for various crosswise sections taken along the length of the microchannel for  $x/H = 0.8, 1.6, 2.4, 3.2$  and  $4.0$ . For  $Kn = 0.14$  at  $x/H = 0.8$ , the flow is in the freestream region and hence the profile is linear. This becomes parabolic for  $x/H = 1.6$  and as the flow progresses downstream the Mach number profile the peak value decreases corresponding to the drop in velocity downstream. This is due to the higher viscous effects for helium. On the other hand, for less viscous nitrogen a gradual change in the parabolic profile for  $Kn = 0.062$  is observed as the flow progresses. Evidently, higher Mach number produces more slip on the walls.

Corresponding sections for the temperature distribution show the development of thermal boundary layer. Figure 36 depicts these crosswise profiles of the temperature. In the freestream region the temperature remains linear. For  $Kn = 0.14$ , thermal boundary formation starts at  $x/H = 0.8$  with knees near the top and bottom surfaces. This distortion merges towards the center of the channel as the flow develops. Finally at  $x/H = 4.0$  the flow becomes fully developed with both peaks vanishing. For  $Kn = 0.062$ , the development of the thermal boundary layer does not complete at  $x/H = 4.0$ . The contours in Figure 26(a) show that the thermal boundary formation continues beyond  $x/H = 4.2$ .



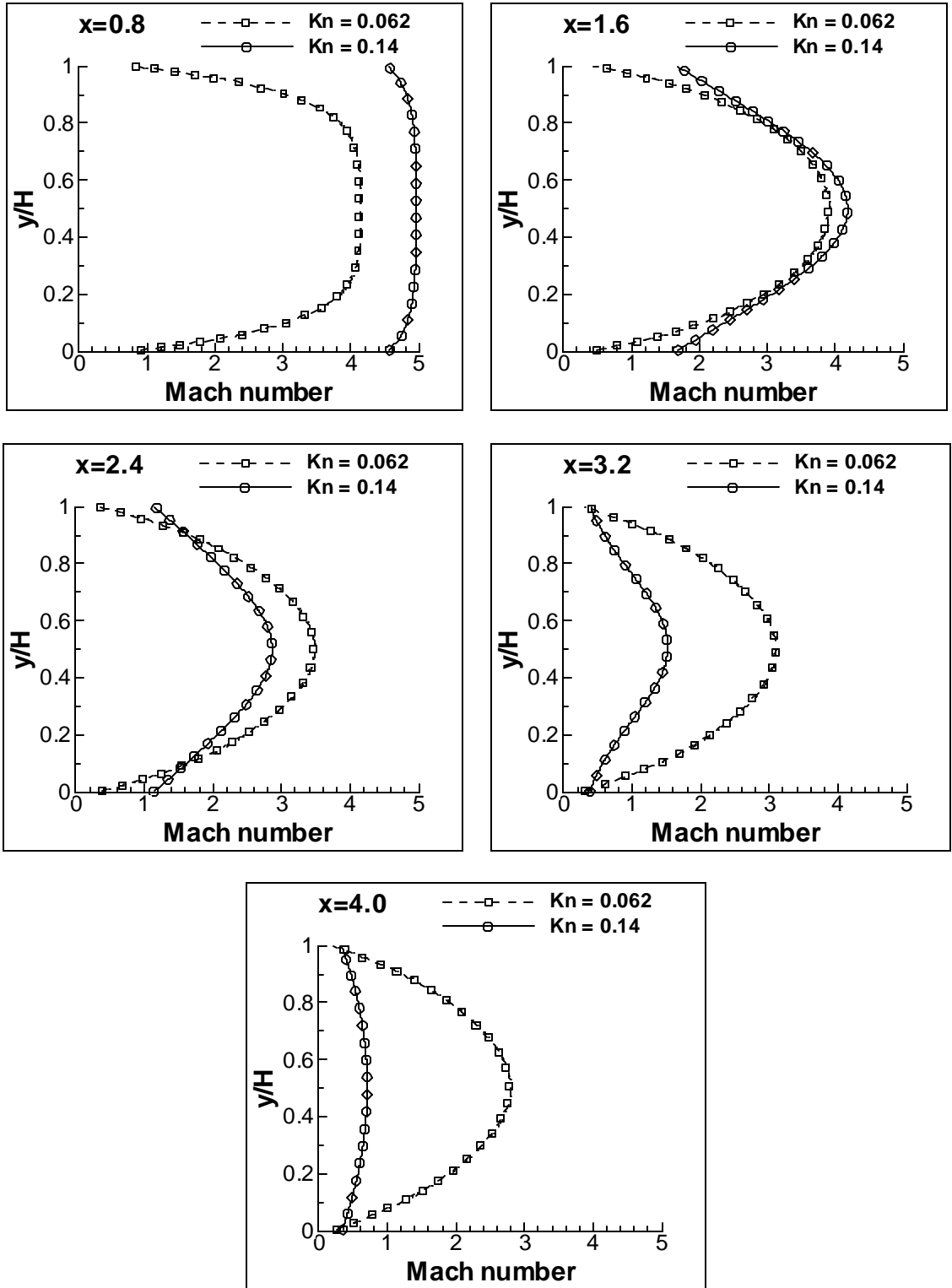


Figure 35. Comparison for various cross sections in the y-direction for  $Kn = 0.062$  and  $Kn = 0.14$  along the streamwise direction for Mach number.

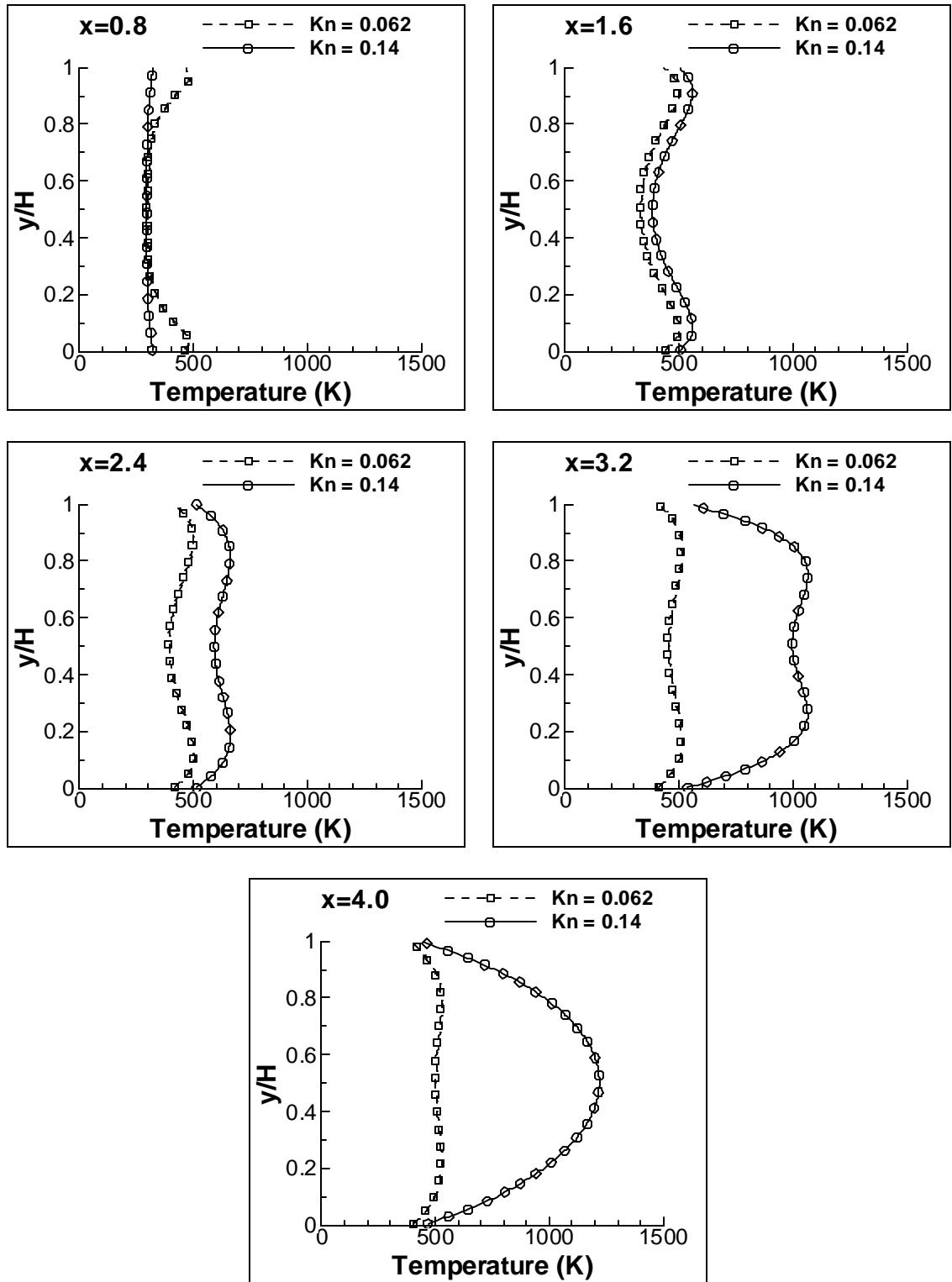


Figure 36. Comparison for various cross sections in the  $y$ -direction for  $Kn = 0.062$  and  $Kn = 0.14$  along the streamwise direction for temperature.

## V. MODELING OF SUBSONIC GAS FLOW THROUGH A MICROCOLUMN

Present study focuses on flow through a microcolumn with two sharp  $90^\circ$  bends, which is a geometric modification of the straight microchannel studied by Poiseuille flow [38, 49]. This geometry has application in many practical microfluidic devices that require serpentine channels to allow longer contact length within a compact area [88]. The following sections cover the model description, boundary conditions and discussion of numerical results. The solution obtained for the bends are also compared to the reported numerical results for the straight microchannel [38] so as to understand the overall effect of tortuosity on the flow. To the best of my knowledge, no other published report has addressed microflow in this particular geometry.

### **Model Description**

The two-dimensional micro-column geometry under consideration is shown in Figure 37. The overall dimensions of the microchannel with two  $90^\circ$  bends are based on the first generation straight microchannel system [38]. The centerline length  $L$ , height  $H$  and width  $W$  remain the same for the same microchannel [38]. For two-dimensional analysis the end effects across the width  $W$  (normal to the  $xy$ -plane) have been ignored. The working fluid is Nitrogen and its properties along with other flow parameters are listed in Table 3. The aspect ratio of the channel is 2500 with a centerline length of 3000  $\mu\text{m}$  and the Knudsen number at the outlet is 0.0585 for the given atmospheric conditions.

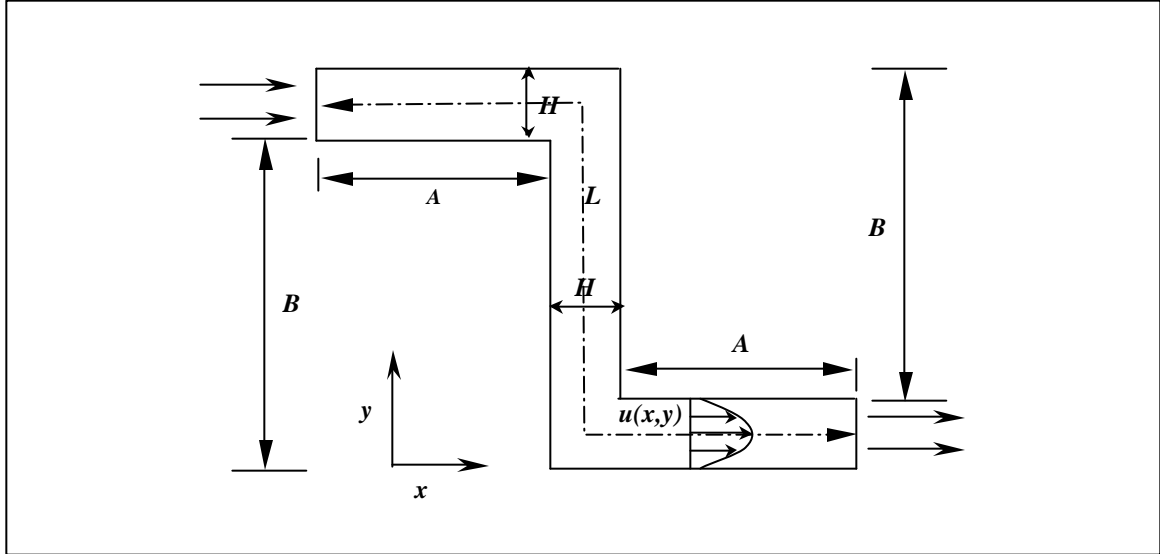


Figure 37. Geometry schematic of microcolumn used for flow analysis.

Table 3

Model Dimensions and Gas Properties for Flow through a Microcolumn

<i>Parameters</i>	<i>Value</i>
Centerline length, $L(\text{mm})$	3000
$A(\text{mm})$	999.4
$B(\text{mm})$	1000
$W(\text{mm})$	40
$H(\text{mm})$	1.2
$P_{in}/P_{out}$	1.34, 1.68, 2.02, 2.36, 2.70
$P_{out}(\text{kPa})$	100.8
$T_i(\text{K})$	314
$T_w(\text{K})$	314
$Kn$	0.0585
$m(\text{Ns/m}^2)$	$1.85 \times 10^{-5}$
$R(\text{J/kg K})$	296.7
?	1.4

## **Boundary Conditions**

The gas temperature  $T_{in}$  at the inlet is specified as 314 K. A uniform wall temperature  $T_w$  is also specified as 314 K. The velocity flux  $\partial u/\partial x=0$  and the y-component of the velocity  $v = 0$  is specified at the inlet. The micro-column is benchmarked using both no-slip and first order slip conditions. For no-slip conditions  $u=0$  and  $v=0$  is used on the walls, while equations (10) and (12) are used for the slip boundary conditions. For slip boundary, since the roughness of the channel is not known, we assume  $s_V = s_T \approx 1.0$  consistent with that of the straight microchannel, implying that the channel surface is rough. The pressure at the outlet,  $P_{out}$ , is maintained at 100.8 kPa while the inlet pressure,  $P_{in}$ , is specified based on the pressure ratio.

## **Results and Discussion**

The flow through the channel has been analyzed for both slip and no-slip boundary conditions. The computational domain is discretized using 560 (28 along  $L$ , 20 along  $H$  in Figure 37) two-dimensional biquadratic finite elements that consist of 2337 nodes. For a  $90^\circ$  bend, the flow undergoes skewing due to the change in streamwise direction in comparison to the flow through a straight duct. In Figure 38(a), the no-slip solution shows a skewed parabolic profile in the vertical region near the bend due to the change in direction of the flow. Under slip boundary condition there is a visible flattening of this parabolic profile showing high gas velocities adjacent to the walls, Figure 38(b).

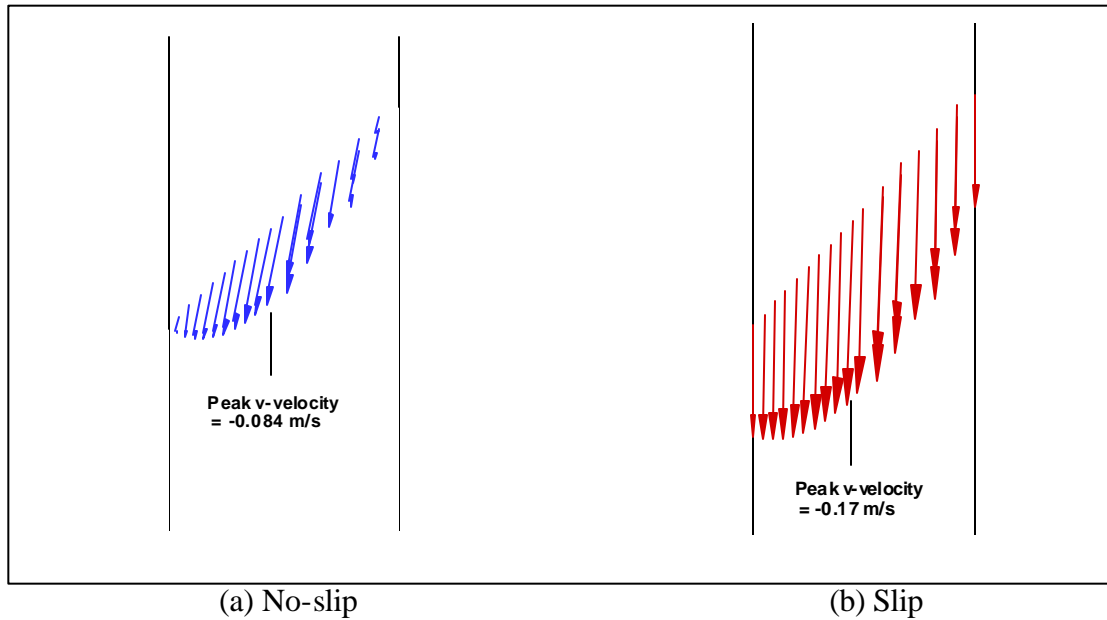


**Figure 38.** Downstream velocity vectors in the micro-column for  $P_{in}/P_{out}=2.70$ . The peak  $v$ -velocities are shown at the centerline distance of  $1200 \mu\text{m}$  from the inlet.

For this geometry and boundary specifications, the pressure, density and velocity vary non-linearly along the microchannel. The difference in temperature over the computational domain is negligible resulting in an almost isothermal condition similar to that of the straight microchannel [38]. The pressure drop occurs to overcome the frictional forces along the channel. For a simple Poiseuille flow the velocity increases downstream to preserve the continuity equation. The rise in shear stress with increasing in velocity causes a further drop in pressure. The centerline effect shows a relatively higher slope in pressure drop when the flow becomes vertical, Figure 39. This is due to the higher shear stress caused by the sharp change in momentum at the bends. However, at the same time slip flow encounters lesser shear stress than the no-slip condition. Increasing pressure ratios show increasing divergence in the pressure distribution between the no-slip and slip wall solutions. For five selected pressure ratios, the no-slip

solutions show a steeper slope in the vertical section than in slip solutions, Figure 39.

This effect is the most prominent for pressure ratio  $P_{in}/P_{out} = 2.70$  where the difference in the pressure distribution between the two predictions is  $\sim -6\%$  at the first bend and  $\sim +10\%$  at the downstream bend.

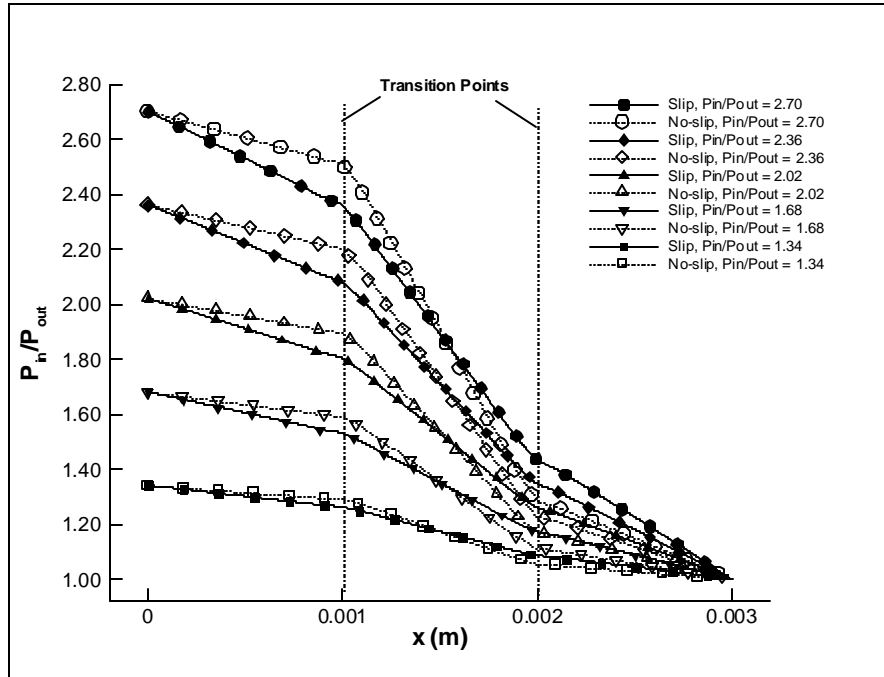


**Figure 39.** Pressure distribution comparison of slip and no-slip boundary condition along the centerline of the micro-column with  $90^\circ$  bends.

Pong *et al.* [38] have carried out experimental measurements for pressure distribution along a straight microchannel using four pressure sensors along the length of the channel. This first generation microchannel was used to validate the numerical results obtained for same geometry earlier in Chapter III. A comparison of the numerical slip results of the straight and  $90^\circ$  bend shows a marked difference in the pressure distribution, Figure 40. The change in direction of flow at the bends causes a change in

slope at these transition points. The pressure drop in the three sections however tends to be more linear than for a straight channel. For five selected pressure ratios, the distribution for the bend show a maximum difference of  $\sim+4\%$  at the upstream bend and  $\sim-20\%$  along the downstream bend. The difference becomes larger as the pressure ratio increases.

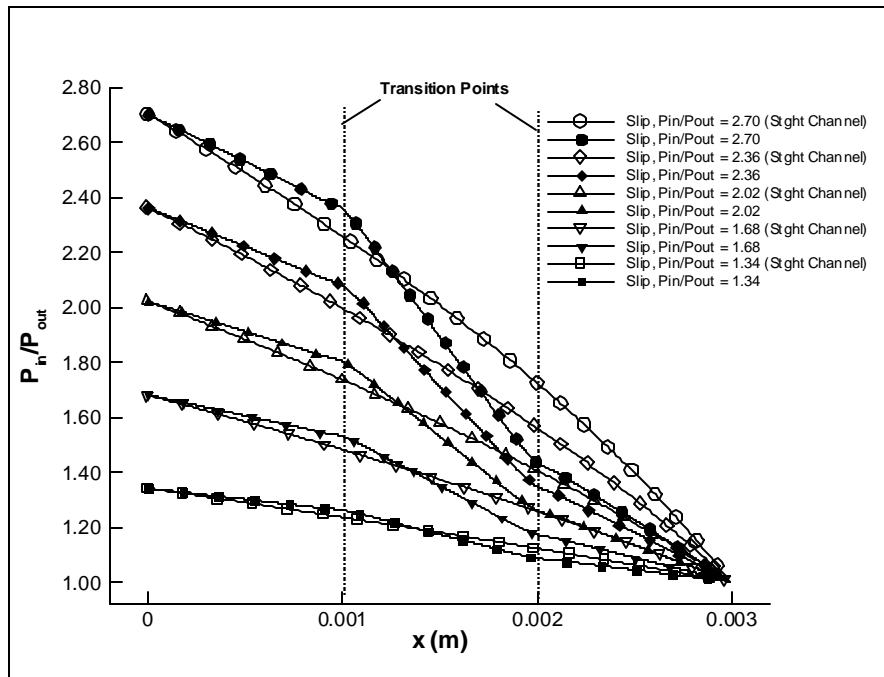


Figure 40. Pressure distribution comparison of slip flow results for the micro-column with  $90^\circ$  bend and a straight microchannel [38] along the centerline.

For a Poiseuille flow, the drop in pressure leads to corresponding increase in the axial velocity. For the micro-column the  $u$ -velocity increases until the first transition point and then encounters a sudden drop (to nearly zero) due to the change in direction of the flow plotted in Figure 41. The  $u$ -velocity again picks up at the second transition point (bend). The increase in velocity is proportionate to the pressure ratio for a fixed outlet



pressure. The slip condition indicates that less frictional force has to be overcome on the walls, which in turn generates a relatively higher velocity when compared to the no-slip condition. Thus the slip flow shows nearly 55% more  $u$ -velocity at the peak point than the no-slip condition for  $P_{in}/P_{out}=2.70$ . The small negative values of  $u$ -velocity at the two bends may indicate re-circulation as flow turns sharply.

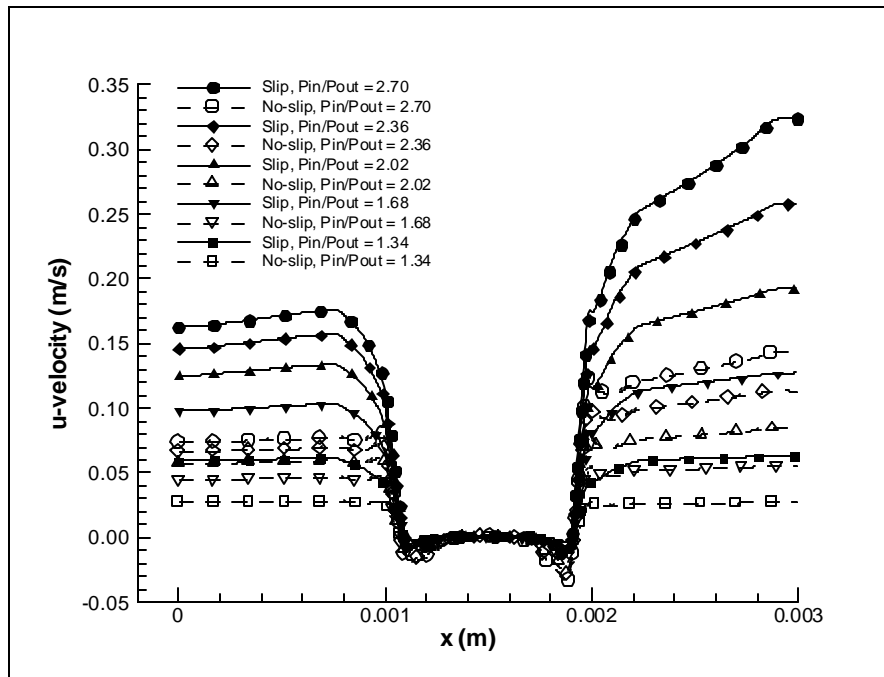


Figure 41.  $u$ - velocity distribution comparison of slip and no-slip boundary condition along the centerline of the micro-column with  $90^\circ$  bends.

Since the primary flow occurs in both  $x$  and  $y$  directions along the three sections of the channel, the stream-wise velocity changes from  $u$  to  $v$  at the first bend and vice versa at the second. In Figure 42, as the gas flow turns in the negative  $y$ -direction, a negative value of  $v$ -velocity is seen. The difference in the slip and no-slip values of the  $v$ -velocity is also plotted in the same figure. The centerline distribution shows a sharp rise

in the magnitude of velocity in the vertical section, a trend proportionate to rise in  $u$  in the horizontal sections, and is essentially zero for the rest of the domain. Similar to the  $u$  dependence the difference between slip and no-slip flows is larger for higher pressure ratios. The small positive values at transition points ( $x = 0.001$  and  $0.002$  m) may be indicative of the local re-circulation.

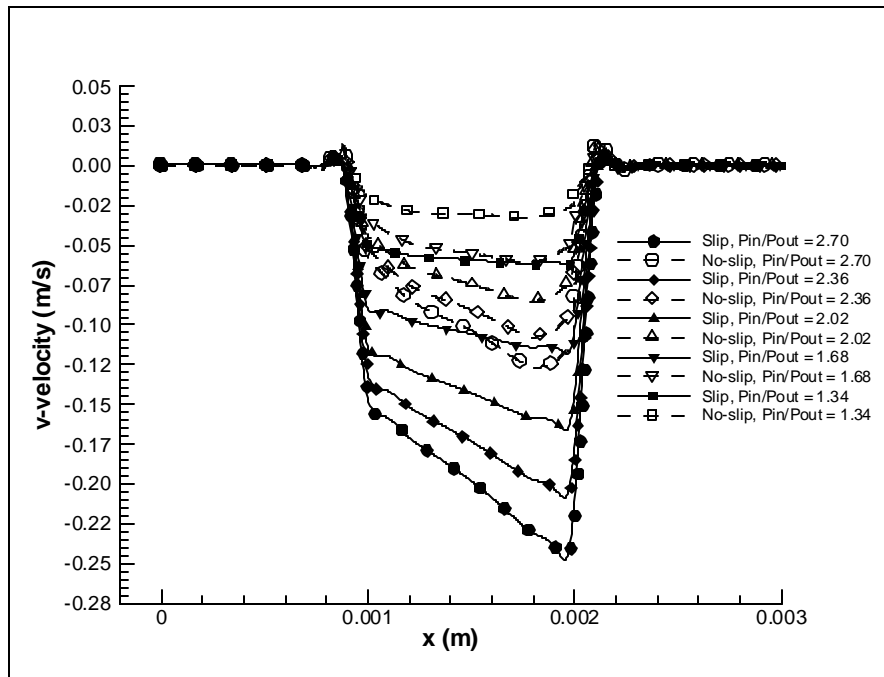


Figure 42.  $v$ - velocity distribution comparison of slip and no-slip boundary condition along the centerline of the micro-column with  $90^\circ$  bends.

Figure 43 compares the mass flow rate versus the pressure ratios for slip and no-slip conditions. Up to 2.4 times more mass flow rates are observed for slip flows than for the no-slip condition. This is due to lower shear stress on the slip walls resulting in less momentum exchange. As compared to the straight microchannel the gas flow inside the

micro-column with two 90° bends has to overcome relatively higher shear stress reducing the overall mass flow rate by approximately 0.4 times.

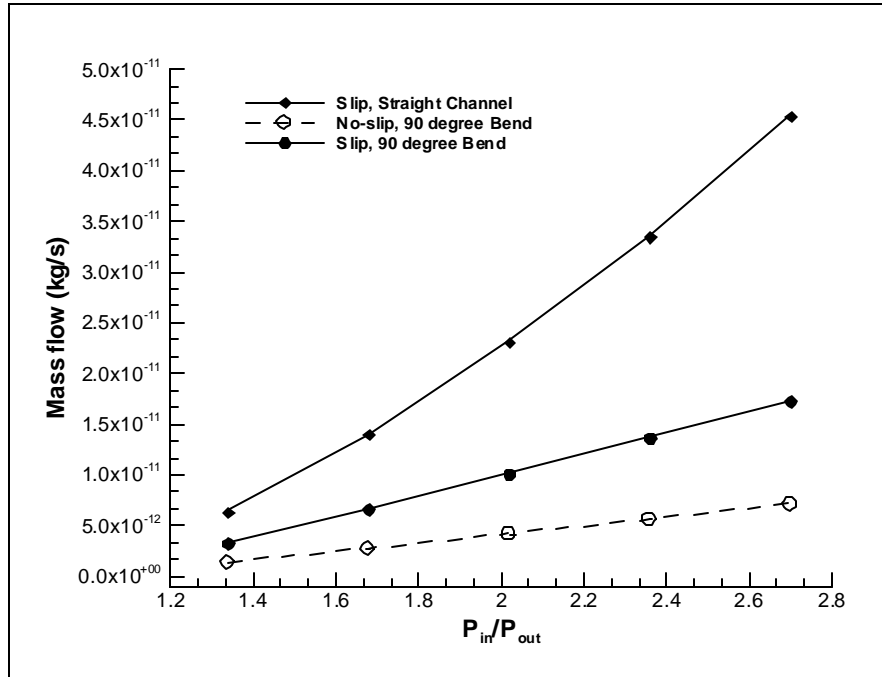


Figure 43. Numerical comparison of mass flow rate for five pressure ratios with slip and no-slip wall conditions for the micro-column with 90° bends. The mass flow rate of gas flow inside a straight microchannel of same overall length is also plotted.

## **VI. MODELING OF GAS FLOW THROUGH NANOPORE AND NANOTUBULE**

The transport behavior in nanopores is generally modeled using molecular dynamics, kinetic Monte Carlo, lattice gas models and other atomistic simulation methods, as mentioned in Chapter I. These studies reflect that the nanoscale bounded flows exhibit diffusive characteristics of normal, single-file and transition modes. [16, 62-63,67] The bulk flow and transport characteristics cannot be distinguished for systems displaying single-file or normal diffusion [64]. This model aims at an exploratory prediction of overall (bulk) characteristics of nanosystems beyond the slip flow regime. Sufficiently wide pores with a nominal diameter of 200 nm have been used for which the boundary layers of the fluid having modified structure do not overlap. Since recent studies show that even nanopores are governed by a finite slip length [27, 70], the hydrodynamic description is reasonable for this case.

Two different analyses are presented for gaseous flow through the nanopores and nanotubules. The first case documents gas flow prediction through an anodisc membrane having a nominal pore diameter of 200 nm. The exit Knudsen number for this case is high (7.36) indicating a transition regime flow. The Knudsen diffusivity calculated from the numerical results is compared with the measured and analytical values.

The second case determines the slip coefficient values for tubular carbon structures that have been produced by chemical vapor deposition (CVD) on a porous alumina substrate with nominal pore diameters of 200 nm. A uniform 20-30 nm thick carbonaceous coating was formed over the pores. The massflux obtained from numerical solutions for three gas flows (Oxygen, Nitrogen and Argon) are compared with the experimental data for varying slip accommodation coefficients. The slip coefficient for the 800 °C case was benchmarked with the analytical value obtained using the formulation by Arkilic *et al.* [45]. All experiments presented in this Chapter were done at the NASA Ames Center for Nanotechnology, California. The author is solely utilizing the data for validation purposes. Some description of the experiment is retained for completeness.

## **Nanopore**

### **Anodisc membrane** [28]

The experimental data were collected from commercial Whatman alumina filters (Anodisc 13) with pore sizes of 200 nm and thickness of 60  $\mu\text{m}$  [28]. The density and sizes of pores were measured in a scanning electron microscope (SEM) and found to be  $5\text{-}8 \times 10^{12} \text{ m}^{-2}$  and 212 nm, respectively, giving an estimated porosity of 0.2-0.3. The SEM image of the surface of these filters is shown in Figure 44. The nominal dimension of a single nanopore and the physical properties of the working fluid are listed in Table 4 for pressure ranging between 0-1200 torr (0-160 kPa). The working fluid selected is Argon, although data was also collected for Nitrogen and Oxygen, which gives a Knudsen number of 7.36 at the outlet. The relationship between flow rate and pressure

drop for a diffusive transport regime with a constant diffusion coefficient and negligible viscous effects can be expressed analytically as,

$$\frac{F}{eA} = D_k \frac{\Delta P}{RTL} \quad (33)$$

where  $F$  is the molar flow rate,  $e$  is the membrane porosity,  $A$  is the exposed area,  $\Delta P$  is the pressure drop across the membrane,  $L$  is the thickness,  $R$  is the ideal gas constant,  $T$  is the ambient temperature. The diffusion coefficient is consistent with the Knudsen diffusivity,  $D_k$ , given by:

$$D_k = \frac{d_{pore}}{3} \sqrt{\frac{8RT}{pMe}} \quad (34)$$

where  $d_{pore}$  is the pore diameter and  $Me$  is the molecular weight of the diffusing species.

Table 4

Nanopore Dimensions and Fluid Properties

<i>Flow Parameters</i>	<i>Value</i>
<b><math>L</math> (mm)</b>	60
<b><math>d_{pore}</math> (nm)</b>	200
<b><math>DP = P_{in} - P_{out}</math> (torr)</b>	100, 300, 600, 900
<b><math>P_{out}</math> (kPa)</b>	4.8
<b><math>T_{in}</math> (K)</b>	300
<b><math>T_w</math> (K)</b>	300
<b>Kn</b>	7.36
<b><math>\mu</math> (Ns/m<sup>2</sup>)</b>	$2.22 \times 10^{-5}$
<b><math>R</math> (J/kg K)</b>	208.1
<b>?</b>	1.4
<b><math>Me</math> (kg/kmol)</b>	39.948

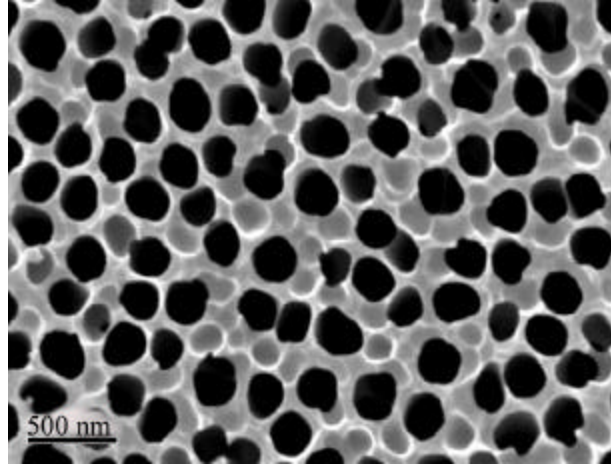


Figure 44. SEM image of Anodisc membrane of 200 nm pores. [28]

### Carbon nanotubule [32]

At the nanometer sizes one major factor in determining the flow characteristics can be the fluid-surface interaction. Controlling the nature of pore surfaces can significantly alter the flow properties through the transport media. The experimental setup for this case consists of monitoring the pressure drop across porous anodic alumina filter with carbonaceous coating versus a controlled flow rate. A uniform 20-30 nm thick carbonaceous coating was formed over the pores using the chemical vapor deposition (CVD) approach. This involved treating the pores at temperatures of 700, 750 and 800 °C [32]. Three separate pore diameters of 235, 220 and 169 nm were obtained after this treatment. For the 169 nm pores treated at 800 °C the carbon coating was observed to be the thickest. The permeability of the porous alumina was then measured using a pressure/flow apparatus. The bulk measurements can be related to the flux through an individual pore by introducing a correction for the membrane porosity. This introduces the largest error into the calculation as the pore areas can vary by as much as 25% across

a single sample. Table 5 contains the pore dimensions and properties for three working fluids Oxygen, Nitrogen and Argon.

### **Boundary Conditions**

Tables 4 and 5 describe the inlet, outlet and wall condition details for the nanopore and nanotubule. At the inlet the gas temperature  $T_{in}$  is specified and based on the assumption of isothermal wall, the wall temperature  $T_w$  is also specified. The velocity flux  $\partial u/\partial x=0$  and the y-component of the velocity  $v = 0$  at the inlet. The pressure at the outlet,  $P_{out}$  is 4.8 kPa for all the cases and the inlet pressure,  $P_{in}$  is specified based on the corresponding the pressure drop,  $DP$ . For the anodisc membrane, we assume the accommodation coefficients  $s_V = s_T \approx 1.0$  while for the nanotubule the tangential momentum accommodation coefficient (TMAC),  $s_V$  is varied to match the experimental data.

Table 5

### **Nanotubule Dimensions and Fluid Properties**

<b><i>Flow Parameters</i></b>	<b><i>Argon</i></b>	<b><i>Nitrogen</i></b>	<b><i>Oxygen</i></b>
<b><i>L (mm)</i></b>	60	60	60
<b><i>d<sub>pore</sub> (nm)</i></b>	169, 220, 235	169	169
<b><i>DP = P<sub>in</sub> - P<sub>out</sub> (torr)</i></b>	100-1000	50,115,180,250	50,120,190,260
<b><i>P<sub>out</sub> (kPa)</i></b>	4.8	4.8	4.8
<b><i>T<sub>in</sub> (K)</i></b>	300	300	300
<b><i>T<sub>w</sub> (K)</i></b>	300	300	300
<b><i>μ (Ns/m<sup>2</sup>)</i></b>	$2.22 \times 10^{-5}$	$1.85 \times 10^{-5}$	$2.06 \times 10^{-5}$
<b><i>R (J/kg K)</i></b>	208.1	298.6	259.8
<b><i>?</i></b>	1.4	1.4	1.395
<b><i>Me (kg/kmol)</i></b>	39.948	35.69	31.25



## **Results and Discussion**

### **Anodisc membrane**

The nanopore geometry is discretized using  $24 \times 18$  two-dimensional non-overlapping bi-quadratic finite elements resulting in a total of 1813 nodes. Here again, fully implicit time integration is utilized and the dimensional equations (2)-(6) are solved using Newton-Raphson iterative procedure. The working fluid is selected to be Argon. For the wall and inlet temperatures maintained at 300K, it is assumed that the solution temperature nearly stays isothermal along the channel, implying that the density is directly proportional to the pressure. For nanoporous Alumina, Itaya, et al. [89] also demonstrated the linear pressure dependence of fluxes for various gases. Note that the Knudsen number for this problem reaches up to 7.36 at the outlet. Karniadakis and Beskok [4] (pp. 92) have noted that for this highly rarified gas flow the pressure distribution becomes more linear. In Figure 45, the density, streaming velocity distribution and the molar flux at the centerline of the pore show the presence of Knudsen diffusion regime. Solution density, see Figure 45(a), is normalized by the outlet density while the streaming velocity in Figure 45(b) is normalized by the inlet value.

Figure 46 compares the porosity corrected experimental data with the numerical prediction for Argon. The numerical result deviates as the pressure drop increases. However, the linear dependence between the gas flux and the pressure drop is clearly captured. Corresponding Knudsen diffusivity is calculated for Argon based on the computed molar flow rate for pressure drop across the pore as 2.72 and tabulated in Table 6. The measured diffusivities have an accuracy of approximately 20%, owing to

uncertainty in the membrane porosity measurement. The diffusivity based on the numerical solution are calculated on the basis of the following formulae.

$$D_k = \frac{FRL}{eA\Delta P} \quad (35)$$

However since for the same nanopore only the molar flux rate,  $F$  and pressure drop  $\Delta P$  are varying. Hence the measure diffusivity,  $(D_k)_{Measured}$  can be used to calculate the numerical diffusivity,  $(D_k)_{Calculated}$ ,

$$\frac{(D_k)_{Calculated}}{(D_k)_{Measured}} = \left( \frac{F}{\Delta P} \right)_{Measured} \left( \frac{\Delta P}{F} \right)_{Calculated} \quad (36)$$

The calculated diffusivity is within +2% of that of the measured data and within –3% of the analytical value.

Table 6

Calculated and Measured Diffusivities of Anodisc Membrane ( $\times 10^{-5} \text{ m}^2/\text{s}$ ).

	Knudsen Diffusivity	Measured Diffusivity	Calculated Diffusivity
Argon	2.80	2.66	2.72

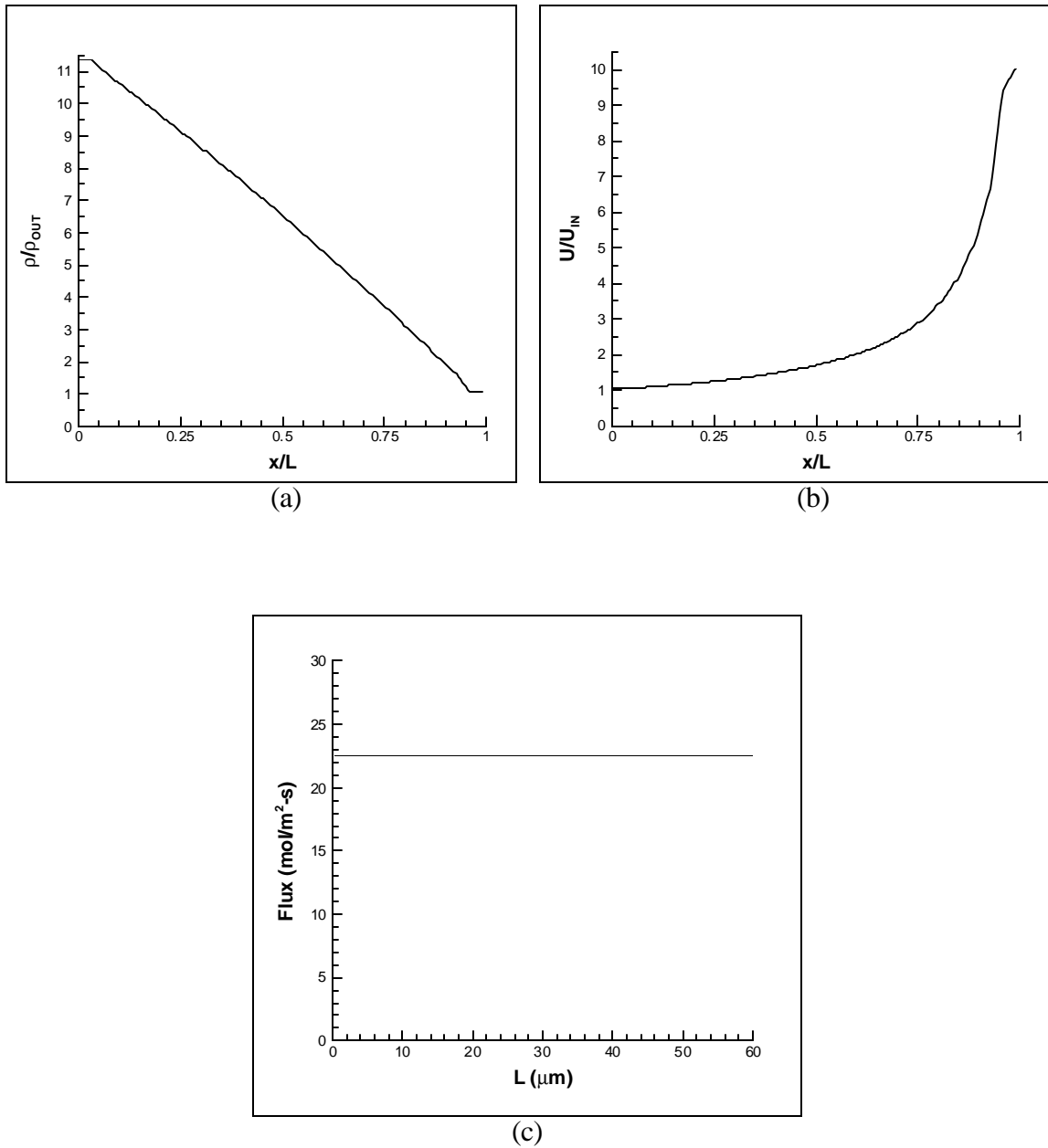


Figure 45. (a) Density profile at the centerline, (b) velocity profile at the centerline, and (c) Argon molar flux along the centerline for  $DP = 600$  torr.

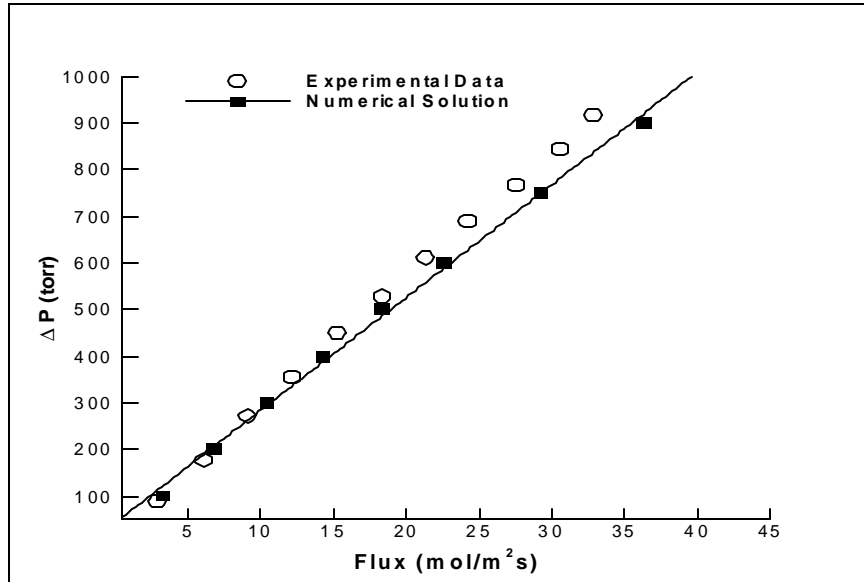


Figure 46. Solution validation of numerical results with experimental data for Argon.

### Carbon nanotubule

The nanopore geometry is discretized using  $28 \times 20$  two-dimensional non-overlapping bi-quadratic finite elements with a total of 2337 nodes. The measured mass flux for Argon through the nanopore sample prepared at 700 °C is compared with the fluid model in Figure 47. The measured data for this 235 nm diameter pore matches well with the numerical solution with for TMAC,  $s_V = 1.0$ . Figure 48 compares the similar massfluxes for 220 nm diameter pores prepared at 750 °C for Argon for varying pressure drops across the pore. For this case also it found that the measured fluxes with 25% error compare well with the numerical result for TMAC,  $s_V = 1.0$ . For the 700 and 750 °C treated samples carbon coating inside the pore is negligible. This indicates in the absence of a carbonaceous material, transport can be well described by diffuse reflection at the wall consistent with that for the anodisc membrane simulated earlier.

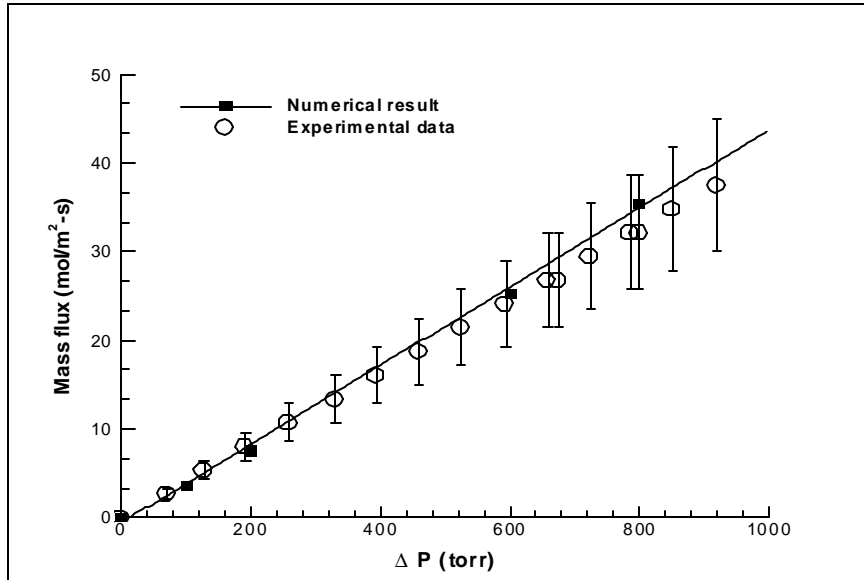


Figure 47. Flux versus pressure drop for Anodisc membranes processed with CVD at temperatures of 700° C compared to numerical results for  $s_v = 1.0$ .

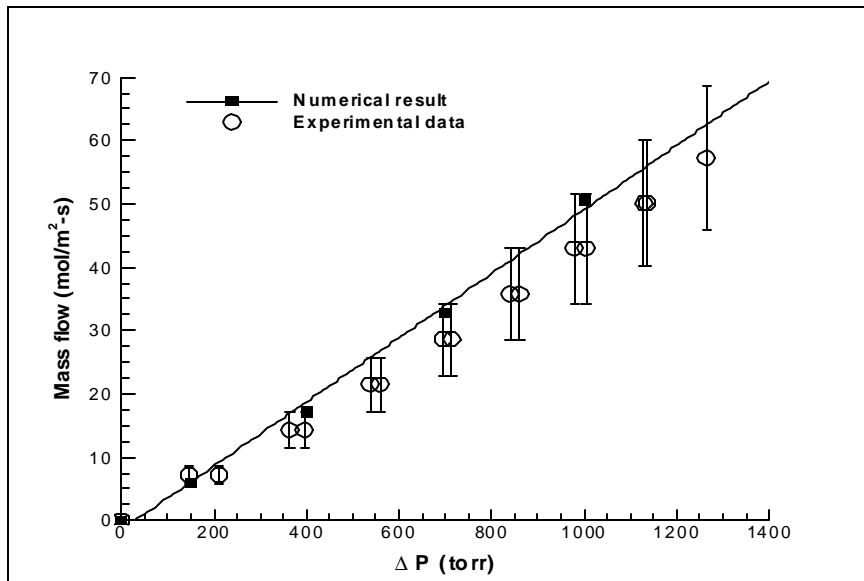
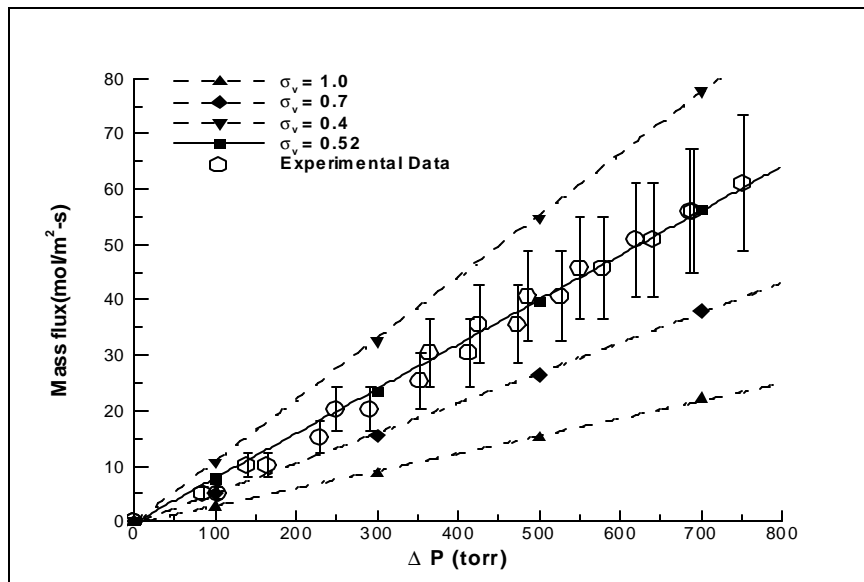


Figure 48. Flux versus pressure drop for Anodisc membranes processed with CVD at temperatures of 750° C compared to numerical results for  $s_v = 1.0$ .

For the nanopore prepared at 800 °C the carbonaceous coating is relatively thicker. Figure 49 compares the massflux for argon through this nanopore sample having a nominal diameter of 169 nm with the experimental data for varying pressure drop across the nanopore. The single adjustable parameter, the TMAC ( $s_v$ ), is adjusted to match the behavior observed experimentally. It is found that the numerical solution for  $s_v = 1.0$  under-predicts the massflux by approx. 62%. Comparing the data to the model with a variety of slip coefficients ranging from 1.0 to 0.4, it is found that a slip coefficient of 0.52 gives the best representation of the measured data obtained for argon. This slip coefficient of  $s_v = 0.52$  is then applied to the systems of oxygen and nitrogen, and is found to represent both sets of data well, Figures 50 & 51. The experiment reports about 25% error for the measured data.



**Figure 49.** Argon massflux versus pressure drop for Anodisc membranes processed with CVD at 800° C compared to numerical results for different values of TMAC values.

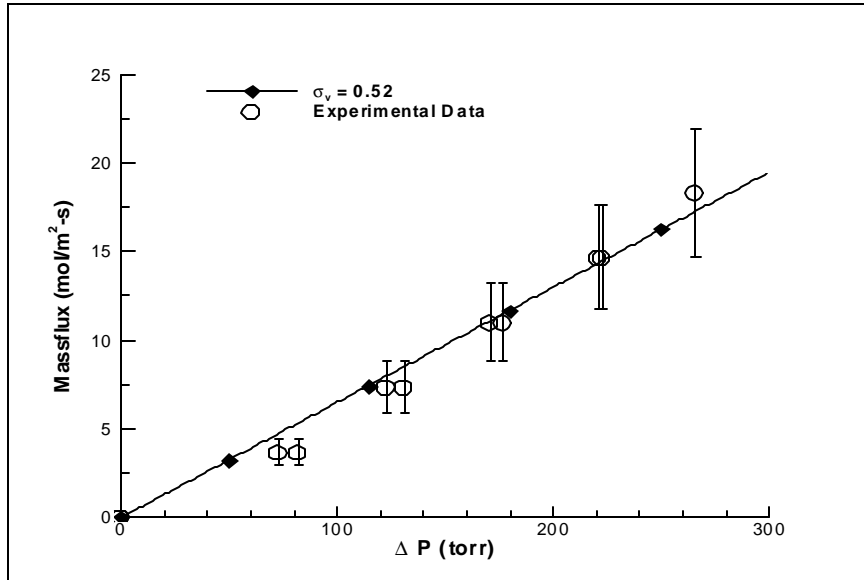


Figure 50. Nitrogen massflux versus pressure drop for Anodisc membranes processed with CVD of 800° C compared to numerical results for  $\sigma_v = 0.52$ .

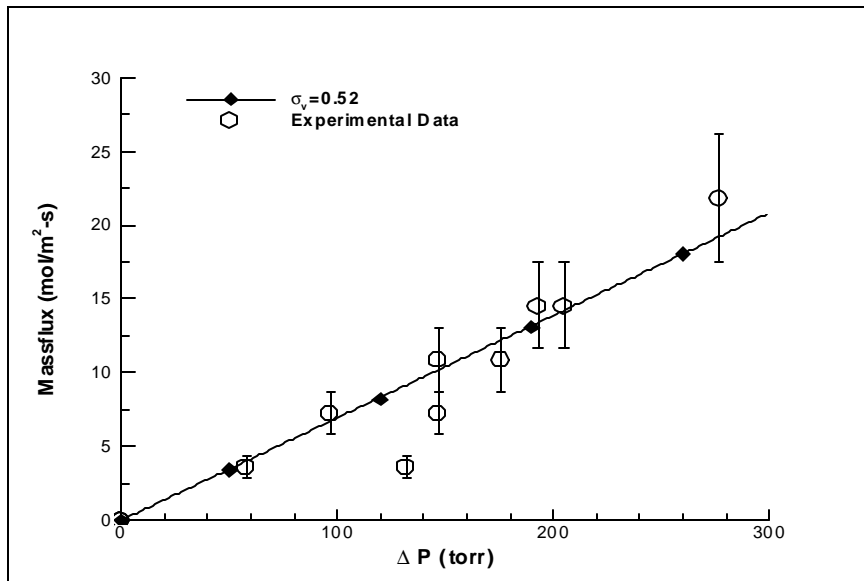


Figure 51. Oxygen massflux versus pressure drop for Anodisc membranes processed with CVD at 800° C compared to numerical results for  $\sigma_v = 0.52$ .

The analytical momentum slip coefficient may be estimated by plotting the following relation [45],

$$\frac{\dot{m}}{P_{in}^2 - P_{out}^2} = B \frac{1}{\bar{P}} + C, \text{ and} \quad (37)$$

$$B = \frac{A_x \bar{d}^2}{4nlRT} \frac{2 - s_v}{s_v} Kn_{out} P_{out}, \quad C = \frac{A_x \bar{d}^2}{24nlRT}$$

where  $\dot{m}$  is the mass flow rate in kg/s,  $P_{in}$  and  $P_{out}$  are the inlet and outlet pressures,  $\bar{P} = (P_{in} + P_{out})/2$  is the mean pressure,  $\bar{d}$  is the average pore diameter, and  $A_x$  is the cross-sectional area of a single pore. In Figure 52, the normalized mass flow rate experimental Argon data from the 800 °C sample is plotted as a function of inverse mean pressure. The slope of this line is then used to estimate the analytical momentum slip coefficient as  $s_v = 0.6$  which is close to the value obtained numerically,  $s_v = 0.52$ .

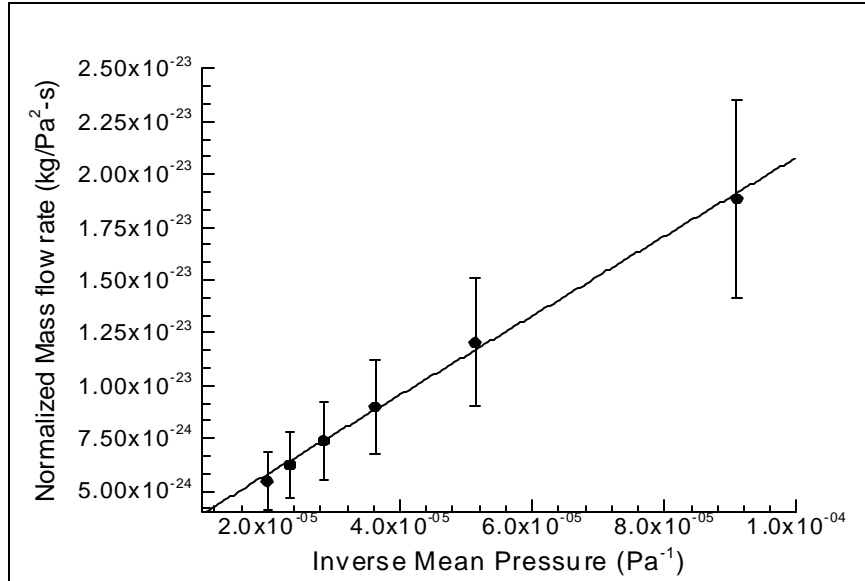


Figure 52. Normalized mass flow rate  $\dot{m}/P_i^2 - P_o^2$  for experimental Argon data at 800 °C plotted as a function of the inverse mean pressure  $1/\bar{P}$ . The slope of the line is utilized to estimate analytical  $\sigma_v = 0.6$ .



## VII. CONCLUSIONS AND RECOMMENDATIONS

This thesis documents the development and benchmarking of a finite element based hydrodynamic formulation for two-dimensional flow prediction of gases through micro-geometries and nanopores. Gas flows through these systems were found to be in the slip and transition regime. Since all the slip models presented in literature have no significant advantages or disadvantages Maxwell's first order slip boundary has been put to use here. The validation of results with both experimental and numerical data, wherever available, showed that the hydrodynamic model was efficiently able to capture the bulk flow characteristics of gas flows inside these systems.

Subsonic gas flow through microchannels has been modeled for three microchannels with aspect ratios 2500, 3333 and 5639. The exit Knudsen number for these cases were 0.0585, 0.17 and 0.155 respectively. The results show a non-linear distribution for pressure and velocity inside the microchannel for all the three cases. As the pressure ratio increases the non-linearity grows. The slip flow results report higher streaming velocity and higher mass flow rates than the corresponding no-slip solution for the same pressure ratio. The hydrodynamic model results compare well with published finer grid finite difference results.

Flow and heat transfer characteristics of high speed gas flows through shorter microchannels with aspect ratio 5 has been modeled for two cases with Knudsen numbers 0.14 and 0.062. The two cases considered incorporate different fluids, namely, Helium and

Nitrogen. The higher Knudsen number case with helium reflects a higher heat transfer characteristics. Although the heat transfer and flow characteristics for hydrodynamic solutions for high speed flows differ slightly in values the profiles obtained are similar to that of the reported DSMC results. The deviation in values could possibly be due to difference in location where the exit backpressure was specified. However, the hydrodynamic model with first order slip boundary conditions was able to capture sharp shock and wall interaction features for the supersonic flows through the microchannel.

The applicability of the hydrodynamic model has been extended to analyze low speed nitrogen flow through a micro-column with two 90° bends for an outlet Knudsen number of 0.0585. The results capture the effect of slip on the walls showing a ~55% higher streaming velocity than the corresponding no-slip solution. Slip flows also show significantly higher mass flow rates. The twisted geometry of the present study reduces the mass flow rate by ~160% than that for a straight microchannel with the same overall dimensions. The analysis indicates suitability of the algorithm for efficiently predicting flows through practical microfluidic devices.

For the 200 nm anodisc membrane nanopores a linear pressure dependence of gas flux is observed. The outlet Knudsen number is found to be 7.36. Based on the calculated flow rate for a given pressure drop, the numerically predicted diffusivity for Argon is within +4.6% of the measured data and -0.4% of the analytical value. Slip coefficient for alumina membranes with carbonaceous coating of varying thickness is determined for working fluid Argon. It is found that for negligible carbon coating a completely diffuse reflection on the walls sufficiently predicts mass flux on matching numerical mass flux with the experimental data. However, for a thicker coating (800 °C) a value of 0.52 is

obtained for TMAC while the analytical value is found to be 0.6. The TMAC value of 0.52 holds good for all the three gases, Argon, Nitrogen and Oxygen.

### **Recommendations for Future Work**

Micro/nano-fluidics is a developing area where a number of issues are yet to be resolved.

Following are some of my recommendations for future work in this area,

1. A grid independent study of the presented cases should be carried out to conclude the numerical aspect of the study.
2. First order slip/jump model may not be sufficient to model gas flows in some cases. Several higher models have been suggested in order overcome the drawbacks of the Maxwell's slip model; however, each has its own shortcomings. A study of the existing models should be done and an empirical model spanning slip-transitional regime should be developed to overcome their shortcomings.
3. This study has been limited to simple microgeometries like microchannels, microcolumns and nanopores. The utility of the algorithm should be extended to practical microfluidic devices like micropumps, actuators and microthrusters.
4. The behavior of liquids in microsystems is different from that of gases since it also involves accommodating surface forces, wetting and electrokinetic effects. Studies to understand these effects should also be undertaken.
5. Phonon transport, adsorption and quantum effects are some factors that could play a major role in determining the heat transfer and flow characteristics in nanosystems. A detailed study of these effects and implementation into the hydrodynamic model needs to be carried out.

## REFERENCES

- 1) Feynman, R.P. (1961) There's Plenty of room at the bottom Miniaturization, ed. H.D.Gilbert, Reinhold Publishing, New York, pp. 282-296.
- 2) Merriam- Webster Online, [www.m-w.com/home.htm](http://www.m-w.com/home.htm).
- 3) Gad-el-hak, M. (1999) The Fluid Mechanics of Microdevices- The Freeman Scholar Lecture Journal of Fluids Engineering, vol.121, pp. 5-33.
- 4) Karniadakis, G. and Beskok, A. (2002) Micro Flows-Fundamentals and Simulation Springer-Verlag, New York.
- 5) Ho, C.M. and Tai, Y.C. (1998) Micro-electro-mechanical systems (MEMS) and fluid flows Annual Review Fluid Mechanics 30, pp. 579-612.
- 6) Bird, G. A. (1976) Molecular Gas Dynamics Clarendon Press, Oxford, United Kingdom.
- 7) Xue, H., Fan, Q. and Shu, C. (2000) Prediction of Microchannel Flow Using Direct Simulation Monte Carlo, Probabilistic Engineering Mechanics, Vol. 15(2), pp. 213-219.
- 8) Jie, D., Diao X., Cheong, K.B. and Yong, L.K. (2000) Navier-Stokes simulations of gas flow in micro devices Journal of Micromechanics and Microengineering, vol. 10, pp. 372-379.
- 9) Schaaf, S.A. and Chambre, P.L. (1961) Flow of rarefied gases Princeton University Press, Princeton, New Jersey.
- 10) Maxwell, J.C. (1879) On stresses in rarefied gases arising from inequalities of temperature Philosophical Transactions of the Royal Society Part 1, vol.170, pp. 231-256.

- 11) Smoluchowski, von M. (1898) Ueber wärmeleitung in verdünnten gasen Annalen der Physik und Chemi, vol. 64, pp. 101-30.
- 12) Alder, B. J. and Wainwright, T. E. (1957) Phase Transition for a Hard Sphere System Journal of Chemical Physics, vol.27, pp. 1208-1209.
- 13) Alder, B. J. and Wainwright, T. E. (1958) Molecular Dynamics by Electronic Computers Transport Processes in Statistical Mechanics, ed. I. Prigogine., Interscience, New York, pp. 97-131.
- 14) G. A. Bird, (1994) Molecular Gas Dynamics and the Direct Simulation of Gas Flows Clarendon Press, Oxford, United Kingdom.
- 15) J. Koplik, and J. R. Banavar, Annual Review of Fluid Mechanics, **27**, 257 (1995).
- 16) Mao, Z. and Sinnott , S.B. (2000) A Computational Study of Molecular Diffusion and Dynamic Flow Through Carbon Nanotubes Journal of Physical Chemistry B, vol. 104, pp. 4618-4624.
- 17) M. N. Kogan, (1969) Rarefied Gas Dynamics, Nauka, Moskow, Translated from Russian, L. Trilling, Ed. Plenum, New York.
- 18) Muntz, E. P. (1989) Rarefied gas dynamics Annual Review of Fluid Mechanics, vol. 21, pp. 387-417.
- 19) Oran, E. S., Oh, C. K. and Cybyk, B. Z. (1998) Direct simulation Monte Carlo: recent advances and applications Annual Review of Fluid Mechanics, vol. 30, pp. 403-442.
- 20) Koppenwallner, G. (1987) Low Reynolds number influences on the aerodynamic performance lifting vehicles Aerodynamics of Hypersonic Lifting Vehicles, AGARD, CP-428, 11, 1.
- 21) Oh, C.K., Oran E.S. and Sinkovits R.S., (1997) Computations of High speed, High Knudsen number Microchannel flows Journal of Thermophysics and Heat Transfer, vol. 11, pp. 497-505.
- 22) Fisco, K. A. and Chapman, D. R. (1988) Comparison of Burnett, Super-Burnett and Monte-Carlo solutions for hypersonic shock structure Proc. 16th International Symposium on Rarefied Gas Dynamics, Pasadena, CA.

- 23) X. Zhong, (1991) Development and computation of continuum higher order constitutive relations for high-altitude hypersonic flow Ph.D. Thesis, Stanford University, Stanford.
- 24) Agarwal, R.K., Yun, K. and Balakrishnan, R. (2001) Beyond Navier-Stokes: Burnett equations for flows in the continuum-transition regime Physics of Fluids, vol. 13(10), pp. 3061-3085.
- 25) Burnett, D. (1935) The distribution of molecular velocities and the mean motion in a non-uniform gas Proceedings of London Mathematical Society, vol. 40, pp. 382-435.
- 26) Comeaux, K. A., Chapman, D. R. and MacCormack, R. W. (1995) An Analysis of the Burnett Equations Based on the Second Law of Thermodynamics AIAA Paper No. 95-0415.
- 27) Sokhan, V.P, Nicholson, D. and Quirke, N. (2001), Fluid flow in nanopores: An examination of hydrodynamic boundary conditions Journal of Chemical Physics, vol. 115, pp. 3878-3887.
- 28) Roy, S., Raju, R., Chuang, H., Kruden, B. and Meyyappan, M. (2003) Modeling gas flow through microchannels and nanopores Journal of Applied Physics, vol.93 (8), pp. 4870-4879.
- 29) Raju R. and Roy S. (2003) Hydrodynamic model for microscale flows in a channel with two 90° bends ASME Fluids Engineering Division Summer Meeting, Honolulu, Paper FEDSM 2003-45535.
- 30) Raju, R. and Roy S. (2003) Hydrodynamic Prediction of High Speed Microflows AIAA Paper No. 2003-4010.
- 31) Raju, R. and Roy S. (2003) Numerical Study of Heat Transfer in High Speed Microflows AIAA Paper No. 2003-4051.
- 32) Cooper, S.M., Cruden, B.A., Meyyappan, M., Raju, R. and Roy, S. (2003) Determination of slip coefficient of a carbon nanotubule Paper no. 228d, AIChE Annual Meeting, San Francisco, Nov. 16-21.
- 33) Wu, P.Y. and Little, W.A. (1984) Measurement of the heat transfer characteristics of gas flow in fine channel heat exchanger used for microminiature refrigerators Cryogenics, vol. 24, pp. 415-423.

- 34) Choi, S.B., Barron, R.F. and Warrington, R.O. (1991) Fluid flow and heat transfer in microtubes Proceedings of ASME, DSC-32, pp. 123-134.
- 35) Pfahler, J., Bau, H. and Zemel, J.N., (1990) Liquid transport in micron and submicron channels Sensors and Actuators, vol. A21-23, pp. 431-434.
- 36) Liu, J., Tai, Y.C, Pong, K. and Ho, C.M. (1993) Micromachined channel/pressure sensor systems for micro flow studies Transducers '93 Technical Paper, 7<sup>th</sup> International Conference on Solid State Sensors and Actuators, Yokohoma, pp.995-999.
- 37) Liu, J., Tai, Y.C, Pong, K. and Ho, C.M. (1995) MEMS for pressure distribution studies of gaseous flow in microchannels In an investigation of Micro Structure, Sensors, Actuators, Machines and Sytems, Proceedings of 8th Annual International Workshop MEMS, Amsterdam, pp.209-215.
- 38) Pong, K.C., Ho, C., Liu, J. and Tai, Y., (1994) Non-Linear Pressure Distribution in Uniform Microchannels Application of Microfabrication to Fluid Mechanics, FED-197, pp.51-56.
- 39) Shih, J.C., Ho, C.M., Liu, J. and Tai, Y.C. (1995) Non-linear pressure distribution in uniform microchannels ASME AMD-MD 238.
- 40) Shih, J.C., Ho, C.M., Liu, J. and Tai, Y.C. (1996) Monatomic and polyatomic gas flow through uniform microchannels ASME DSC-59, pp. 197-203.
- 41) Harley, J.C., Huang, Y. and Bau, H., (1995) Gas flow in microchannels Journal of Fluid Mechanics, vol. 284, pp. 257-274.
- 42) Arkilic, E.B., Breuer, K.S. and Schmidt, M.A. (1994) Gaseous Flow in Microchannel Application of Microfabrication to Fluid Mechanics, ASME, FED- 197, pp. 57-66.
- 43) Arkilic, E.B., Schmidt, M.A. and Breuer, K.S. (1997) Gaseous slip flow in long microchannels Journal of Microelectromechanical systems, vol. 6(2), pp. 167-178.
- 44) Arkilic, E. B. (1997) Measurement of the Mass Flow and Tangential Momentum accommodation coefficient in silicon micromachined channels Ph.D. Thesis, MIT.

- 45) Arkilic, E.B., Breuer, K.S. and Schmidt, M.A. (2001) Mass flow and tangential momentum accommodation in silicon micromachined channels Journal of Fluid Mechanics, vol. 437, pp. 29-43.
- 46) Peng, X.F., Wang, B.X., Peterson G.P and Ma, H.B. (1995) Experimental Investigation of heat transfer in flat plates with rectangular microchannels International Journal of Heat & Mass Transfer, vol.38(1), pp.127-137.
- 47) Mala, G.M, Li, D. and Dale, J.D., (1997) Heat Transfer and fluid flow in microchannels International Journal Heat & Mass Transfer, vol.40, pp.3079-3088.
- 48) Adams, T.M., Ghiaasiaan, S.M. and Abdel-Khalik, S.I. (1999) Enhancement of liquid forced convection heat transfer in microchannels due to the release of dissolved noncondensables International Journal of Heat & Mass Transfer, vol.42, pp.3563-3573.
- 49) Chen, C.S., Lee, S.M. and Sheu, J.D. (1998) Numerical Analysis of Gas flow in Microchannels Numerical Heat Transfer, Part A, vol. 33, pp.749-762.
- 50) Zohar , Y., Lee, S.Y.K., Lee, W.Y. , Jiang, L. and Tong, Pin, (2002) Subsonic gas flow in a straight and uniform microchannel Journal of Fluid Mechanics, vol. 472, pp. 125-151.
- 51) Xue, H. and Fan, Q., (2000) A New Analytic Solution of the Navier-Stokes Equations for Microchannel Flows Microscale Thermophysical Engineering, vol. 4(2), pp. 125-143.
- 52) Xue, H., Ji, H.M. and Shu, C. (2001) Analysis of micro-Couette flow using the Burnett equations International Journal of Heat and Mass Transfer, vol. 44, pp. 4139-4146.
- 53) Liou, W.W and Fang, Y., (2001) Heat Transfer in Microchannel devices using DSMC Journal of Microelectromechanical Systems, vol.10, no.2, pp.274-279.
- 54) Mavriplis, C., Ahn, J.C. and Goulard, R. (1997) Heat Transfer and flowfields in Short Microchannels using Direct Simulation Monte Carlo Journal of Thermophysics and Heat Transfer, vol. 11, no. 4, pp. 489-496.
- 55) McNenly, M., Gallis, M and Boyd, I. (2003) Slip model performance of MEMS gas flows AIAA Paper No. 2003-4050.



- 56) Iijima, S. (1991) Helical Microtubules of Graphitic Carbon Nature, vol. 354, pp. 56-58.
- 57) Iijima, S. and Ichihashi, T. (1993) Single-shell Carbon Nanotubes of 1-nm Diameter Nature, vol. 363, pp. 603-605.
- 58) Bethune, D.S., Kiang, C.H., de Vries, M.D. , Gorman, G. , Savoy, R., Vazquez, J. and Beyers, R. (1993) Cobalt-catalyzed Growth of Carbon Nanotubes with Single-atomic-layer walls Nature, vol. 363, pp. 605-607.
- 59) Kärger, J. and Ruthven, D.M. (1992) Diffusion in Zeolites and other Microporous solids Wiley, New York.
- 60) Chen, N.Y. and Degnan Jr., T.F., and Smith, C.M (1994) Molecular transport and Reactions in Zeolites VCH , New York.
- 61) Tuzun, R. E., Noid, D. W., Sumpter, B. G. and Merkle, R. C. (1996) Dynamics of fluid flow inside carbon nanotubes Nanotechnology, vol. 7, pp. 241-246.
- 62) Sholl, D. S. and Fichthorn, K. A. (1997) Normal, Single-File, and Dual-Mode Diffusion of Binary Adsorbate Mixtures in AlPO<sub>4</sub>-5 Journal of Chemical Physics vol.107, pp. 4384-.
- 63) Sholl, D. S., (2000) Characterization of Molecular Cluster Diffusion in AlPO<sub>4</sub>-5 Using Molecular Dynamics Chemical Physics Letters, vol. 305, pp. 269.
- 64) Sholl, D. S., (2000) Predicting Single-Component Permeance through Macroscopic Zeolite Membranes from Atomistic Simulations Industrial and Engineering Chemistry Research, vol. 39, pp. 3737-3746.
- 65) Saravanan, C. and Auerbach, S. M (1999) Theory and Simulation of Cohesive Diffusion in Nanopores: Transport in Subcritical and Supercritical Regimes Journal of Chemical Physics, vol 10, pp. 11000-11010.
- 66) Keffer, D. (1999) The Temperature Dependence of Single-File Separation Mechanisms in One-dimensional Nanoporous Materials Chemical Engineering Journal, vol. 74, pp.33-42.
- 67) Mao, Z., and Sinnott , S.B. (2001) Separation of organic molecular mixtures in carbon nanotubes and bundles: Molecular dynamics simulations Journal of Physical Chemistry B, vol. 105, pp. 6916-6924.

- 68) MacElroy, J.M.D., Pozhar, L.A. and Suh, S.-H. (2001) Self-Diffusion in a Fluid Confined within a Model Nanopore Structure *Colloids and Surfaces A*, vol. 187, pp. 493-507.
- 69) ten Bosch, A. (2001) Persistent diffusion in nanopores *Journal of Chemical Physics*, vol. 114(11), pp. 4982.
- 70) Sokhan, V.P, Nicholson, D. and Quirke, N. (2002) Fluid flow in nanopores: Accurate boundary conditions for carbon nanotubes *Journal of Chemical Physics*, vol. 117, pp. 8531–8539.
- 71) Seo, Y.-G., Kum, G.-H. and Seaton, N.A. (2002) Monte Carlo simulation of transport diffusion in nanoporous carbon membranes *Journal of Membrane Science*, vol. 195, pp. 65.
- 72) Nicholson, D. (2002) A simulation study of the pore size dependence of transport selectivity in cylindrical pores *Molecular Physics*, vol. 100(13), pp. 2151-2163.
- 73) Düren, T., Kiel, F.J. and Seaton, N.A. (2002) Composition dependent transport diffusion coefficients of CH<sub>4</sub>/CF<sub>4</sub> mixtures in carbon nanotube by non-equilibrium molecular dynamics simulations *Chemical Engineering Science*, vol. 57, pp. 1343-1354.
- 74) Ackerman, D. M., Skoulidas, A. I., Sholl, D. S. and Johnson, J. K. (2003) Diffusivities of Ar and Ne in Carbon Nanotubes *Molecular Simulation* (in press).
- 75) Vargo, S.E., Muntz, E.P., Shiflett, G.R. and Tang, W.C. (1999) Knudsen compressor as a micro- and macroscale vacuum pump without moving parts or fluids *Journal of Vacuum Science and Technology*, vol. 17(4), pp. 2308-2313.
- 76) Lord, R. (1976) Tangential momentum coefficients of rare gases on polycrystalline surfaces In *Proceedings of the Tenth International Symposium on Rarefied Gas Dynamics*, pp. 531-538.
- 77) Srekanth, A. (1969) Slip flow through long circular tubes *Proceedings the sixth international symposium on rarefied gas dynamics*, ed. L. Trilling and H.Y. Wachman, Academic Press, New York, 1, pp. 667-680.

- 78) Piekos, E. and Breuer, K. (1995) DSMC modeling of microchannel devices AIAA Paper No. 95-2089.
- 79) Lockerby, D.A. and Reese, J.M. (2003) High resolution Burnett simulations of micro-Couette flow and Heat Transfer Journal of Computational Physics, (article in press).
- 80) Oden, J. T. and Oliveira, E. R. A. (1976) Lectures on Finite Element Methods in Continuum Mechanics The University of Alabama in Huntsville Press, Huntsville.
- 81) Baker, A.J. (1983) Finite Element Computational Fluid Mechanics Hemisphere Publishing Corporation, New York.
- 82) Tezduyar, T.E., Behr, M. & Hughes, T.J.R. (1995) High Performance Finite Element Computation of Fluid Dynamics Problems Computational Fluid Dynamics Review (eds. M. Hafez and K. Oshima), John Wiley & Sons, pp. 300-321.
- 83) Roy, S. and Baker, A. J. (1998) Sub Grid eMbedding (SGM) Algorithm - Part II, Navier-Stokes solutions Journal of Numerical Heat Transfer - Part B (Fundamentals), vol. 33(1), pp. 5-36.
- 84) Balagangadhar, D. and Roy, S. (2001) Design Sensitivity Analysis and Optimization of Steady Fluid-Thermal Systems Computer Methods in Applied. Mechanics and Engineering, vol. 190(42), pp. 5465-5479.
- 85) Roy, S. and Pandey, B.P. (2002) Numerical Investigation of a Hall Thruster Plasma, Physics of Plasmas, vol.9 (9), pp. 4052-4060.
- 86) Baker, A.J. and Pepper, D.W. (1991) Finite Elements 1-2-3 McGraw Hill, Inc.
- 87) Richtmyer, R.D. and Morton, K.W. (1967) Difference Methods for Initial-Value Problems 2<sup>nd</sup> Ed, Interscience Publishers, Wiley, New York.
- 88) Molho, J.I., Herr, A.E. , Mosier, B.P. , Santiago, J.G. , Kenny, T.W. , Brennen, R.A., Gordon, G.B. and Mohammadi, B. (2003) Optimization of turn geometries for microchip electrophoresis Analytical Chemistry, vol. 73, pp. 1350-1360.

- 89) Itaya, K., Sugawara, S., Arai, K. and Saito, S. (1984) Properties of Porous Anodic Aluminum-Oxide Films As Membranes Journal of Chemical Engineering of Japan, vol. 17(5), pp.514-520.

## **APPENDICES**

**APPENDIX A**

**NOMENCLATURE**

## NOMENCLATURE

### Greek

$b$	Diffusion parameter
$d_{ij}$	Kronecker delta
$e$	Membrane porosity
$h$	Local coordinate
$g$	Specific heat ratio
$k$	Thermal conductivity
$\lambda$	Mean free path of the fluid
$m$	Coefficient of viscosity
$m\dot{c}$	Second coefficient of viscosity
$f$	Trial function
$\Omega$	Solution domain
$r$	Gas density
$s_v$	Tangential-momentum accommodation coefficient
$s_T$	Thermal accommodation coefficient
$t$	Tangential momentum flux

### Alpha

$a$	Unknown coefficient
$A$	Exposed area
$A_x$	Cross-sectional area
$C_p$	Specific heat at constant pressure
<i>Cont.</i>	Continuity Equation
$\bar{d}$	Average pore diameter
$d_{pore}$	Diameter of nanopore
$dE$	Energy flux
$D_k$	Knudsen diffusivity
<i>Ener.</i>	Energy equation
<i>EOS</i>	Equation of State
$H$	Height
Kn	Knudsen Number
$L$	Centerline length
$L_s$	Slip length

$\dot{m}$	Mass flow rate
$M$	Mass matrix
Ma	Mach number
$M_e$	Molecular mass
<i>Mom.-X</i>	X-Momentum equation
<i>Mom.-Y</i>	Y-Momentum equation
$N$	Basis function
Pr	Prandtl number
$P$	Gas pressure
$\bar{P}$	Mean pressure
$DP$	Pressure difference
$Q$	Discretized state variable
$R$	Reduced gas constant
$S$	Assembly operator
$t$	Time
$T$	Gas temperature
$u$	Gas velocity in $x$ -direction
$Du$	Tangential slip velocity
$v$	Gas velocity in $y$ -direction
$w$	Weight function set
$W$	Width

### Superscript

*	Non-dimensional
$h$	Discretization

### Subscript

$el$	Element
$gas$	Gas property
$ic$	Incident
$in$	Inlet condition
$k$	Degree
$out$	Outlet condition
$o$	Reference condition
$r$	Reflected
$w$	Near wall condition
<i>Calculated</i>	Calculated Values
<i>Measured</i>	Measured Values



## **APPENDIX B**

### **JACOBIAN MATRIX (ACTUAL FORM)**

## JACOBIAN MATRIX (ACTUAL FORM)

$r$	$u$	$v$	$T$	$P$	
↓	↓	↓	↓	↓	
$\left[ \frac{\partial u}{\partial x} + \frac{\partial}{\partial y} + u \frac{\partial}{\partial x} + v \frac{\partial}{\partial y} \right]$	$\left[ \frac{\partial r}{\partial x} + r \frac{\partial}{\partial x} \right]$	$\left[ \frac{\partial r}{\partial y} + r \frac{\partial}{\partial y} \right]$	0	0	← <b>Cont.</b>
$\left[ \begin{array}{c} u \frac{\partial u}{\partial x} + v \frac{\partial u}{\partial y} + \\ u \frac{\partial}{\partial x} + v \frac{\partial}{\partial y} \end{array} \right]$	$\left[ \begin{array}{c} n \frac{\partial}{\partial x} + r \frac{\partial}{\partial y} + r \frac{\partial}{\partial x} + \\ u \frac{\partial r}{\partial x} + v \frac{\partial r}{\partial y} - \\ m \left( \frac{\partial u}{\partial x} \frac{\partial}{\partial x} + \frac{\partial u}{\partial y} \frac{\partial}{\partial y} + \frac{1}{3} \left( \frac{\partial u}{\partial x} \right)^2 \right) \end{array} \right]$	$\left[ \begin{array}{c} \frac{\partial u}{\partial y} + u \frac{\partial r}{\partial y} \\ -m \left( \frac{1}{3} \left( \frac{\partial v}{\partial y} \right)^2 \right) \end{array} \right]$	0	$\left[ \frac{\partial}{\partial x} \right]$	← <b>Mom.-X</b>
$\left[ \begin{array}{c} u \frac{\partial v}{\partial x} + v \frac{\partial v}{\partial y} + \\ u \frac{\partial}{\partial x} + v \frac{\partial}{\partial y} \end{array} \right]$	$\left[ \begin{array}{c} r \frac{\partial v}{\partial y} + v \frac{\partial r}{\partial y} \\ -m \left( \frac{1}{3} \left( \frac{\partial u}{\partial x} \right)^2 \right) \end{array} \right]$	$\left[ \begin{array}{c} n \frac{\partial}{\partial x} + r \frac{\partial}{\partial y} + r \frac{\partial}{\partial y} + \\ u \frac{\partial r}{\partial x} + v \frac{\partial r}{\partial y} - \\ m \left( \frac{\partial v}{\partial x} \frac{\partial}{\partial x} + \frac{\partial v}{\partial y} \frac{\partial}{\partial y} + \frac{1}{3} \left( \frac{\partial v}{\partial y} \right)^2 \right) \end{array} \right]$	0	$\left[ \frac{\partial}{\partial y} \right]$	← <b>Mom.-Y</b>
$C_v \frac{DT}{D}$	$\left[ \begin{array}{c} \frac{\partial T}{\partial x} \frac{\partial P}{\partial x} \\ \left( \frac{\partial u}{\partial x} \frac{\partial}{\partial x} + \right. \\ \left. m \left( \frac{\partial v}{\partial x} + \frac{\partial u}{\partial y} \right) \frac{\partial}{\partial y} \right) \\ \left. + \frac{2}{3} \left( \frac{\partial u}{\partial x} + \frac{\partial v}{\partial y} \right) \frac{\partial}{\partial x} \right]$	$\left[ \begin{array}{c} \frac{\partial T}{\partial y} \frac{\partial P}{\partial y} \\ \left( \frac{\partial v}{\partial y} \frac{\partial}{\partial y} + \left( \frac{\partial v}{\partial x} + \frac{\partial u}{\partial y} \right) \frac{\partial}{\partial x} \right) \\ \left. + \frac{2}{3} \left( \frac{\partial u}{\partial x} + \frac{\partial v}{\partial y} \right) \frac{\partial}{\partial y} \right]$	$\left[ \begin{array}{c} u \frac{\partial}{\partial x} + v \frac{\partial}{\partial y} \\ \frac{\partial T}{\partial x} \frac{\partial}{\partial x} + \frac{\partial T}{\partial y} \frac{\partial}{\partial y} \end{array} \right]$	$\left[ -u \frac{\partial}{\partial x} - v \frac{\partial}{\partial y} \right]$	← <b>Ener.</b>
$[-R]$	0	0	$[-R]$	$[1]$	← <b>EOS</b>

## **APPENDIX C**

### **JACOBIAN MATRIX (USED IN ALGORITHM)**

## JACOBIAN MATRIX (USED IN ALGORITHM)

$r$	$u$	$v$	$T$	$P$	
↓	↓	↓	↓	↓	
$\left[ \frac{\partial u}{\partial x} + \frac{\partial}{\partial y} + u \frac{\partial}{\partial x} + v \frac{\partial}{\partial y} \right]$	$\left[ \frac{\partial r}{\partial x} + r \frac{\partial}{\partial x} \right]$	$\left[ \frac{\partial r}{\partial y} + r \frac{\partial}{\partial y} \right]$	0	0	← <i>Cont.</i>
$\left[ \begin{array}{c} u \frac{\partial u}{\partial x} + v \frac{\partial u}{\partial y} + \\ u \frac{\partial}{\partial x} + v \frac{\partial}{\partial y} \end{array} \right]$	$\left[ \begin{array}{c} n r \frac{\partial}{\partial x} + r v \frac{\partial}{\partial y} + r \frac{\partial u}{\partial x} + \\ u \frac{\partial r}{\partial x} + v \frac{\partial r}{\partial y} - \\ m \left( \frac{\partial u}{\partial x} \frac{\partial}{\partial x} + \frac{\partial u}{\partial y} \frac{\partial}{\partial y} + \frac{1}{3} \left( \frac{\partial u}{\partial x} \frac{\partial}{\partial x} \right) \right) \end{array} \right]$	$\left[ \begin{array}{c} \frac{\partial u}{\partial y} + \frac{\partial r}{\partial y} + u \frac{\partial}{\partial y} \\ -m \left( \frac{1}{3} \left( \frac{\partial v}{\partial y} \frac{\partial}{\partial y} \right) \right) \end{array} \right]$	0	$\left[ \frac{\partial}{\partial x} \right]$	← <i>Mom.-X</i>
$\left[ \begin{array}{c} u \frac{\partial v}{\partial x} + v \frac{\partial v}{\partial y} + \\ u \frac{\partial}{\partial x} + v \frac{\partial}{\partial y} \end{array} \right]$	$\left[ \begin{array}{c} r \frac{\partial v}{\partial y} + v \frac{\partial r}{\partial y} \\ -m \left( \frac{1}{3} \left( \frac{\partial u}{\partial x} \frac{\partial}{\partial y} \right) \right) \end{array} \right]$	$\left[ \begin{array}{c} n r \frac{\partial}{\partial x} + r v \frac{\partial}{\partial y} + r \frac{\partial v}{\partial y} + \\ u \frac{\partial r}{\partial x} + v \frac{\partial r}{\partial y} - \\ m \left( \frac{\partial v}{\partial x} \frac{\partial}{\partial x} + \frac{\partial v}{\partial y} \frac{\partial}{\partial y} + \frac{1}{3} \left( \frac{\partial v}{\partial y} \frac{\partial}{\partial y} \right) \right) \end{array} \right]$	0	$\left[ \frac{\partial}{\partial y} \right]$	← <i>Mom.-Y</i>
$C_v \frac{DT}{D}$	$\left[ \begin{array}{c} \frac{\partial T}{\partial x} \frac{\partial P}{\partial x} \\ \left( \frac{\partial u}{\partial x} \frac{\partial}{\partial x} + \right. \\ \left. m \left( \frac{\partial v}{\partial x} + \frac{\partial u}{\partial y} \right) \frac{\partial}{\partial y} \right) \\ \left. + \frac{2}{3} \left( \frac{\partial u}{\partial x} + \frac{\partial v}{\partial y} \right) \frac{\partial}{\partial x} \right]$	$\left[ \begin{array}{c} \frac{\partial T}{\partial y} \frac{\partial P}{\partial y} \\ \left( \frac{\partial v}{\partial y} \frac{\partial}{\partial y} + \left( \frac{\partial v}{\partial x} + \frac{\partial u}{\partial y} \right) \frac{\partial}{\partial x} \right) \\ \left. + \frac{2}{3} \left( \frac{\partial u}{\partial x} + \frac{\partial v}{\partial y} \right) \frac{\partial}{\partial y} \right]$	$\left[ \begin{array}{c} u \frac{\partial}{\partial x} + v \frac{\partial}{\partial y} \\ \frac{\partial T}{\partial x} \frac{\partial}{\partial x} + \frac{\partial T}{\partial y} \frac{\partial}{\partial y} \end{array} \right]$	$\left[ -u \frac{\partial}{\partial x} - v \frac{\partial}{\partial y} \right]$	← <i>Ener.</i>
[-R]	0	0	[-rR]	[1]	← <i>EOS</i>